Jordan Journal of Mechanical and Industrial Engineering (JJMIE)

JJMIE is a high-quality scientific journal devoted to fields of Mechanical and Industrial Engineering. It is published by The Hashemite University in corporation with the Jordanian Scientific Research Support Fund.

SUBMISSION ADDRESS:

Prof. **Nabil Anagreh** , Editor-in-Chief
Jordan Journal of Mechanical & Industrial Engineering,
Hashemite University,
PO Box 330127, Zarqa, 13133 , Jordan
E-mail: jjmie@hu.edu.jo

Hashemite Kingdom of Jordan

Hashemite University

Jordan Journal of Mechanical and Industrial Engineering

JJMIE

An International Peer-Reviewed Scientific Journal

Financed by Scientific Research Support Fund

http://jjmie.hu.edu.jo/

ISSN 1995-6665

Jordan Journal of Mechanical and Industrial Engineering (JJMIE)

JJMIE is a high-quality scientific journal devoted to fields of Mechanical and Industrial Engineering. It is published by The Jordanian Ministry of Higher Education and Scientific Research in corporation with the Hashemite University.

Introduction: The Editorial Board is very committed to build the Journal as one of the leading international journals in mechanical and industrial engineering sciences in the next few years. With the support of the Ministry of Higher Education and Scientific Research and Jordanian Universities, it is expected that a heavy resource to be channeled into the Journal to establish its international reputation. The Journal's reputation will be enhanced from arrangements with several organizers of international conferences in publishing selected best papers of the conference proceedings.

Aims and Scope: Jordan Journal of Mechanical and Industrial Engineering (JJMIE) is a refereed international journal to be of interest and use to all those concerned with research in various fields of, or closely related to, mechanical and industrial engineering disciplines. Jordan Journal of Mechanical and Industrial Engineering aims to provide a highly readable and valuable addition to the literature which will serve as an indispensable reference tool for years to come. The coverage of the journal includes all new theoretical and experimental findings in the fields of mechanical and industrial engineering or any closely related fields. The journal also encourages the submission of critical review articles covering advances in recent research of such fields as well as technical notes.

Guide for Authors

Manuscript Submission

High-quality submissions to this new journal are welcome now and manuscripts may be either submitted online or mail.

Online: For online submission upload one copy of the full paper including graphics and all figures at the online submission site, accessed via E-mail: jjmie@hu.edu.jo. The manuscript must be written in MS Word Format. All correspondence, including notification of the Editor's decision and requests for revision, takes place by e-mail and via the Author's homepage, removing the need for a hard-copy paper trail.

By Mail: Manuscripts (1 original and 3 copies) accompanied by a covering letter may be sent to the Editor-in-Chief. However, a copy of the original manuscript, including original figures, and the electronic files should be sent to the Editor-in-Chief. Authors should also submit electronic files on disk (one disk for text material and a separate disk for graphics), retaining a backup copy for reference and safety.

Note that contributions may be either submitted online or sent by mail. Please do NOT submit via both routes. This will cause confusion and may lead to delay in article publication. Online submission is preferred.

Submission address and contact:

Prof. **Nabil Anagreh**, Editor-in-Chief
Jordan Journal of Mechanical & Industrial Engineering,
Hashemite University,
PO Box 330127, Zarqa, 13115 , Jordan
E-mail: jjmie@hu.edu.jo

Types of contributions: Original research papers

Corresponding author: Clearly indicate who is responsible for correspondence at all stages of refereeing and publication, including post-publication. Ensure that telephone and fax numbers (with country and area code) are provided in addition to the e-mail address and the complete postal address. Full postal addresses must be given for all co-authors.

Original material: Submission of an article implies that the work described has not been published previously (except in the form of an abstract or as part of a published lecture or academic thesis), that it is not under consideration for publication elsewhere, that its publication is approved by all authors and that, if accepted, it will not be published elsewhere in the same form, in English or in any other language, without the written consent of the Publisher. Authors found to be deliberately contravening the submission guidelines on originality and exclusivity shall not be considered for future publication in this journal.

Supplying Final Accepted Text on Disk: If online submission is not possible: Once the paper has been accepted by the editor, an electronic version of the text should be submitted together with the final hardcopy of the manuscript. The electronic version must match the hardcopy exactly. We accept MS Word format only. Always keep a backup copy of the electronic file for reference and safety. Label the disk with your name. Electronic files can be stored on CD.

Notification: Authors will be notified of the acceptance of their paper by the editor. The Publisher will also send a notification of receipt of the paper in production.

Copyright: All authors must sign the Transfer of Copyright agreement before the article can be published. This transfer agreement enables Jordan Journal of Mechanical and Industrial Engineering to protect the copyrighted material for the authors, but does not relinquish the authors' proprietary rights. The copyright transfer covers the exclusive rights to reproduce and distribute the article, including reprints, photographic reproductions, microfilm or any other reproductions of similar nature and translations.

PDF Proofs: One set of page proofs in PDF format will be sent by e-mail to the corresponding author, to be checked for typesetting/editing. The corrections should be returned within 48 hours. No changes in, or additions to, the accepted (and subsequently edited) manuscript will be allowed at this stage. Proofreading is solely the author's responsibility. Any queries should be answered in full. Please correct factual errors only, or errors introduced by typesetting. Please note that once your paper has been proofed we publish the identical paper online as in print.

Author Benefits

Page charge: Publication in this journal is free of charge.
Free off-prints: Three journal issues of which the article appears in along with twenty-five off-prints will be supplied free of charge to the corresponding author. Corresponding authors will be given the choice to buy extra off-prints before printing of the article.

Manuscript Preparation:

General: Editors reserve the right to adjust style to certain standards of uniformity. Original manuscripts are discarded after publication unless the Publisher is asked to return original material after use. If online submission is not possible, an electronic copy of the manuscript on disk should accompany the final accepted hardcopy version. Please use MS Word for the text of your manuscript.

Structure: Follow this order when typing manuscripts: Title, Authors, Affiliations, Abstract, Keywords, Introduction, Main text, Conclusions, Acknowledgements, Appendix, References, Figure Captions, Figures and then Tables. For submission in hardcopy, do not import figures into the text - see Illustrations. For online submission, please supply figures imported into the text AND also separately as original graphics files. Collate acknowledgements in a separate section at the end of the article and do not include them on the title page, as a footnote to the title or otherwise.

Text Layout: Use double spacing and wide (3 cm) margins. Ensure that each new paragraph is clearly indicated. Present tables and figure legends on separate pages at the end of the manuscript. If possible, consult a recent issue of the journal to become familiar with layout and conventions. All footnotes (except for table and corresponding author footnotes) should be identified with superscript Arabic numbers. To conserve space, authors are requested to mark the less important parts of the paper (such as records of experimental results) for printing in smaller type. For long papers (more that 4000 words) sections which could be deleted without destroying either the sense or the continuity of the paper should be indicated as a guide for the editor. Nomenclature should conform to that most frequently used in the scientific field concerned. Number all pages consecutively; use 12 or 10 pt font size and standard fonts. If submitting in hardcopy, print the entire manuscript on one side of the paper only.

Corresponding author: Clearly indicate who is responsible for correspondence at all stages of refereeing and publication, including post-publication. The corresponding author should be identified with an asterisk and footnote. Ensure that telephone and fax numbers (with country and area code) are provided in addition to the e-mail address and the complete postal address. Full postal addresses must be given for all co-authors. Please consult a recent journal paper for style if possible.

Abstract: A self-contained abstract outlining in a single paragraph the aims, scope and conclusions of the paper must be supplied.

Keywords: Immediately after the abstract, provide a maximum of six keywords (avoid, for example, 'and', 'of'). Be sparing with abbreviations: only abbreviations firmly established in the field may be eligible.

Symbols: All Greek letters and unusual symbols should be identified by name in the margin, the first time they are used.

Units: Follow internationally accepted rules and conventions: use the international system of units (SI). If other quantities are mentioned, give their equivalent in SI.

Maths: Number consecutively any equations that have to be displayed separately from the text (if referred to explicitly in the text).

References: All publications cited in the text should be presented in a list of references following the text of the manuscript.

Text: Indicate references by number(s) in square brackets in line with the text. The actual authors can be referred to, but the reference number(s) must always be given.

List: Number the references (numbers in square brackets) in the list in the order in which they appear in the text.

Examples:

Reference to a journal publication:

[1] M.S. Mohsen, B.A. Akash, “Evaluation of domestic solar water heating system in Jordan using analytic hierarchy process”. Energy Conversion & Management, Vol. 38, No. 9, 1997, 1815-1822.

Reference to a book:

[2] Strunk Jr W, White EB. The elements of style. 3rd ed. New York: Macmillan; 1979.

Reference to a conference proceeding:

[3] B. Akash, S. Odeh, S. Nijmeh, “Modeling of solar-assisted double-tube evaporator heat pump system under local climate conditions”. 5th Jordanian International Mechanical Engineering Conference, Amman, Jordan, 2004.

Reference to a chapter in an edited book:

[4] Mettam GR, Adams LB. How to prepare an electronic version of your article. In: Jones BS, Smith RZ, editors. Introduction to the electronic age, New York: E-Publishing Inc; 1999, p. 281-304

Free Online Color: If, together with your accepted article, you submit usable color and black/white figures then the journal will ensure that these figures will appear in color on the journal website electronic version.

Tables: Tables should be numbered consecutively and given suitable captions and each table should begin on a new page. No vertical rules should be used. Tables should not unnecessarily duplicate results presented elsewhere in the manuscript (for example, in graphs). Footnotes to tables should be typed below the table and should be referred to by superscript lowercase letters.

Preface

Welcome to the first issue of the 2014 volume of the Jordan Journal of Mechanical and Industrial Engineering (JJMIE), launch in 2007. Our Journal is a refereed international journal founded by the Higher Committee for Scientific Research at the Ministry of Higher Education and Scientific Research, and published by the Deanship of Scientific Research and Graduate Studies at the Hashemite University of Jordan. JJMIE has provided a forum for scientists to share their research in all areas of mechanical, industrial, material, mechatronics, biomedical engineering. Articles in the journal considered industrial application as basic and applied studies in the above areas.

This issue contains seven interesting research papers covering various aspects of energy (solar energy, biodiesel and biomass), stress-strain analysis (Neuber method, equivalent strain energy density method, FEM, Stress intensity factor; Stress analysis, crack parameters), and laser cutting and Fuzzy Bayesian Network; (i) Design and Performance Assessment of a Parabolic Trough Collector; (ii) Performance and Combustion Characteristics of a DI Diesel Engine Fueled with Jatropha Methyl Esters and its Blends; (iii) Gasification of Solid Waste Biomass; (iv) A New Method for Calculating Notch tip Stresses and Strains Based on Neuber Method and ESED Method under Multiaxial Loading; (v) Stress Intensity Factors for Crack Located at an Arbitrary Position in Rotating FGM Disks; (vi) Comparison between Taguchi Method and Response Surface Methodology (RSM) in Modelling CO_2 Laser Machining; (vii) The Reliability Analysis of Horizontal Vibration of Elevator Based on Multi-State Fuzzy Bayesian Network. The methodology employed in these research articles ranges from analytical and empirical models to experimental studies.

Prof. Nabil Anagreh
Editor-in-Chief
Hashemite University
Zarqa, Jordan,2014

JJMIE

Volume 8, Number 1, February 2014
ISSN 1995-6665

Jordan Journal of Mechanical and Industrial Engineering

JJMIE

Volume 8 Number 1, February. 2014
ISSN 1995-6665
Pages 1- 5

Jordan Journal of Mechanical and Industrial Engineering

Design and Performance Assessment of a Parabolic Trough Collector

Jamil Al Asfar*, Osama Ayadi and Ahmed Al Salaymeh

Mechanical Engineering Department, The University of Jordan, Amman 11942, Jordan

Abstract

Parabolic trough collectors (PTCs) represent a proven source of thermal energy for industrial process heat and power generation; unfortunately it is still not highly implemented due to technical and economical barriers.

In recent years, environmental issues have focused attention on green energy resources, improving the chance for PTCs to be commercially competitive in the market. The Middle East region is considered an interesting area for implementing solar energy projects since the sun is shining most of the year with high direct irradiance values.

In this study, a six meter long parabolic trough collector was designed, constructed and tested to assess its performance. The result of this work proves the efficiency and potential of such green energy sources for both local society and decision-makers. The mechanical analysis of the structure of the trough was simulated both manually and using the finite element software ABAQUS. The experimental test focused on direct steam generation, temperature variation with mass flow rate and thermal efficiency. The maximum steam temperature measured was 123˚C at a pressure of 2 bars, and the maximum efficiency obtained was 22.4%.

Keywords: *Solar Energy; Concentrated Solar Power; Parabolic Trough Collector; Direct Steam Generation.*

1. Introduction

A legend has it that Archimedes used a "burning glass" to concentrate sunlight on the invading Roman fleet and repel it from Syracuse (Sicily). In 1880 John Ericsson constructed the first known parabolic trough collector. He used it to power a hot air engine. In 1907, the Germans Wilhelm Meier and Adolf Remshardt obtained the first patent of parabolic trough technology. The purpose was the generation of steam [1, 2].

In 1913, the English F. Shuman and the American C.V. Boys constructed a 45 kW pumping plant for irrigation in Maadi, Egypt, which used the energy supplied by trough collectors. The pumps were driven by steam motors, which received the steam from the parabolic troughs. The system was able to pump 27,000 liters of water per minute. Despite the success of the plant, it was shut down in 1915 due to the onset of World War I and also due to lower fuel prices, which made more rentable the application of combustion technologies [3].

In this study, a six-meter long parabolic trough collector was designed, constructed with the least possible cost, and tested to assess its performance. Thermal, optical and mechanical analyses of the parabolic trough were done.

Simple available materials in the Jordanian market were used due to a limited budget. The work was completed through several stages; the first stage was to deal with the theory and mathematical equations for the design of a parabolic trough collector, while the second stage was to manufacture the components and parts needed. The third and fourth stages were designing and building the PTC according to design criteria. The last stage was testing and measuring the temperature and pressure of the obtained steam at several running tests to calculate the efficiency of the manufactured six meter long PTC.

2. CSP Projects in Jordan

There are still no serious CSP projects in Jordan, but there are some experimental small-scale projects in operation:

2.1. Dead Sea Spa Hotel

Parabolic troughs are used to generate hot water to drive a two-stage ammonia absorption chiller in summer and to pre-heat domestic hot water in winter. The system consists of three rows of parabolic solar collectors connected in series with a total number of fourteen collectors.

The reflectors are made of 0.8mm Aluminum sheets covered with Aluminum coating, the HTF is distributed among the collectors through 38mm steel pipe which is insulated with 80mm Rockwool. The absorber tube is connected to the distribution pipe via stainless steel flexible connectors [4].

* Corresponding author. e-mail: jasfar@ju.edu.jo, jamilasfar@yahoo.com.

2.2. Mutah University Tri-Generation CSP Project

The project is located at the Roof top of the engineering department of Mutah University. It utilizes CSP technology for a Tri-Generation of electricity, Water Distillation, and Cooling/Heating.

The project comprises 40 C SP parabolic trough reflector panels that cover 240 m^2 of solar matrix area to generate 120 kW thermal power (kW_{th}) peaks with 15 kW electrical (kW_e), 100 kW_{th} heating and 20 kW_{th} cooling; it also can produce 150 L/Hr of distilled water [5].

3. Theoretical Background

3.1. Thermal Analysis of PTC

A parabolic trough solar collector takes the radiant energy from the sun and converts it to useful thermal energy in the heat transfer fluid (HTF) that circulates through the solar field. Once the geometry and thermal properties are defined, the thermal performance and energy gained by the HTF can be calculated under different configurations and meteorological conditions.

In measuring the thermal efficiency, we apply different flow rates at noontime and record the temperature difference. The input energy is the beam irradiance incident on the aperture multiplied by the projected reflector area. The irradiance can be measured using a pyranometer. The thermal efficiency is given by [1, 2]

$$\eta_{th} = \frac{\dot{Q}_{out}}{\dot{Q}_{in}} = \frac{\dot{m}\, C_p\, \Delta T}{G_b A} \quad (1)$$

where:

$\dot{m}$ is the mass flow rate in the pipe and can be measured by recording the time for filling a specific mass,

ΔT is the difference between the outlet and inlet temperatures measured by thermocouples (K).

C_p is the specific heat of water = 4.2 kJ/kg.K.

G_b is the beam irradiance at the time of test (kW/m^2).

A is the projected reflector area (m^2).

3.2. Stress Analysis:

A mechanical analysis of the trough was done, this was important to predict if mechanical failure may occur in any of the components.

As mentioned, the effect of wind on the trough is an important factor that has to be analyzed. The force produced by wind on the trough can be calculated by the generic formula for actual wind speed:

$$F = APC_d \quad (2)$$

where:

P is the wind dynamic pressure,

A is the projected area

C_d is the drag coefficient

$$F_{wind} = (0.5 \times 1.19 \times 7^2)(1.6 \times 6)(1.6) = 450N$$

And per unit length

$$F_{wind} = 450/6 = 75N/m$$

The weight of the trough will also have a distributed load effect (270 N/m) on the trough as shown in figures 1 and 2, those two figures show the action and reaction forces acting on the trough, in addition to shear force and bending moment diagram.

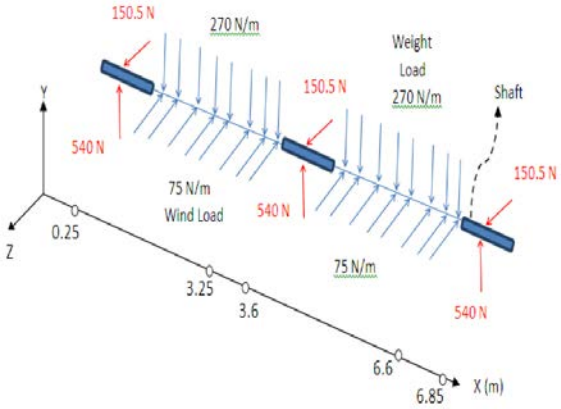

Figure 1.The action and reaction forces acting on the trough.

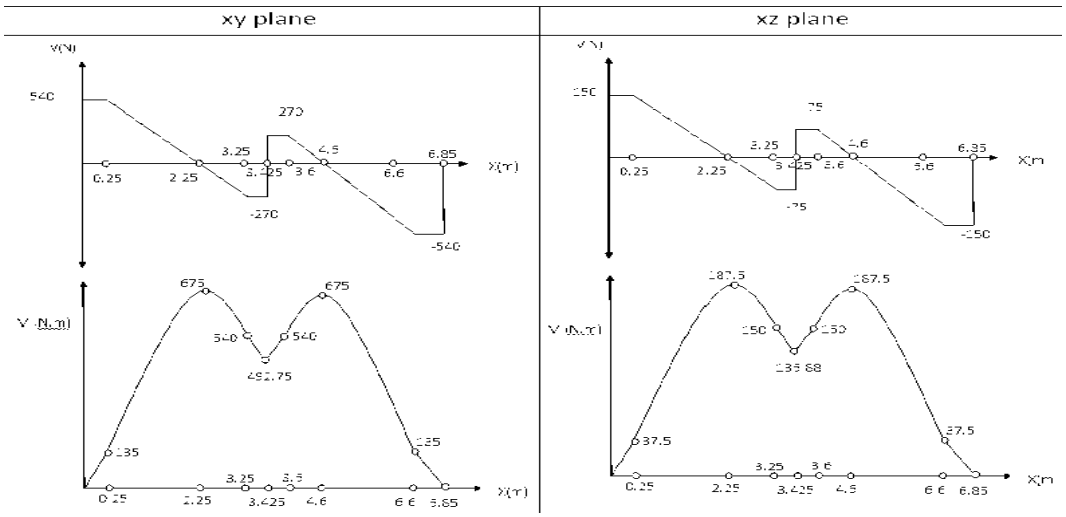

Figure 2. Shear force and bending moment diagrams.

Using an appropriate software, the above boundary and loading conditions were introduced to obtain the deformation and maximum allowable stress as shown in Figures 3-5. The obtained results showed that the loading conditions are within the elastic limits of the complete structure.

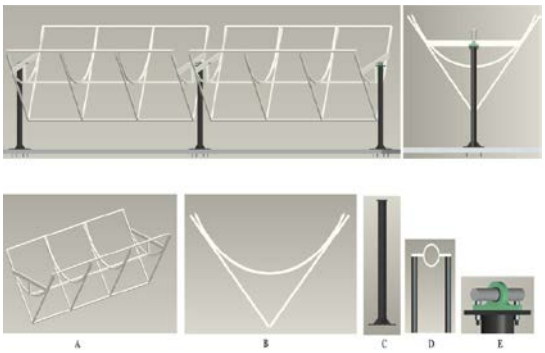

Figure 3. Modelling of the PTC collector.

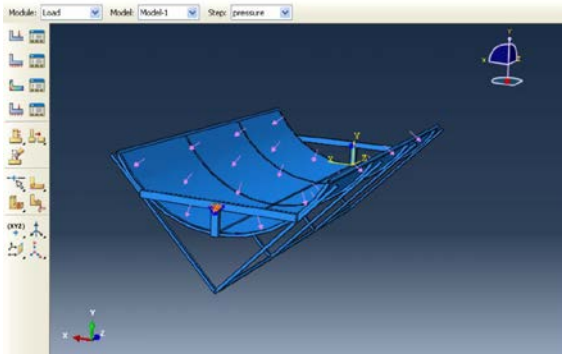

Figure 4. Loading conditions of the PTC.

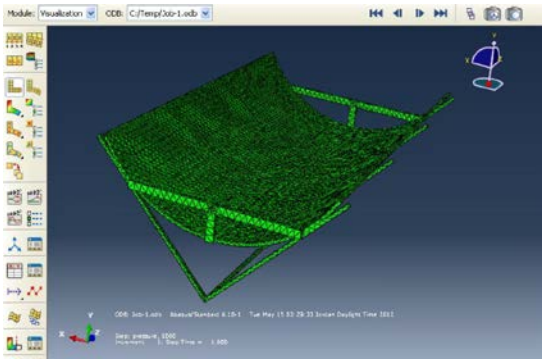

Figure 5. The equivalent Von-Mises stresses.

4. Manufacturing and Testing

The manufacturing process of the locally manufactured CSP is illustrated in the following set of figures:

Figure 6. Tube rolling and welded frame.

Figure 7. Stainless steel mirror used in the project.

Figure 8. Receiver tube and glass tube.

4.1. Experimental Setup

The PTC will be tested in an open circuit flow. The inlet valve is connected to a water supply line and the inlet temperature of the flow is close to ambient temperature. Before the outlet, a pressure gauge which can read up to 14 bar is connected, next to it is a K -type thermocouple connected using a T-connection and a pierced plug. The thermocouple wire is inserted in the plug's small hole and held in it using epoxy droplet glue to avoid water leakage especially at high pressure. After the end valve a one meter length of PEX pipe is connected to send the steam to the air in a s afe way. Sun tracking is done manually and is held in position using a rope connected between the PTC frame and ground. The bearing structure is installed on wheels to adjust the solar south and test the system at different positions.

The components of the final product including the measuring and flow control devices used are illustrated in Figure 9 a nd table 1, while the manufactured system characteristics and the cost of the system components from local market are presented in tables 2 and 3.

Figure 9. PTC components and test rig description (see table 1 for items 1-21).

Table 1. PTC components (see Fig. 9).

1	Outlet water tank	12	Pulley
2	Four bar pressure pipe	13	Stand
3	Pressure gauge	14	Connection shaft
4	Thermocouple	15	Receiver holders
5	Outlet pipe	16	Rope
6	Outlet valve	17	Space frame structure
7	Thermocouple wire inlet to pipe	18	End shaft
8	Pressure relief valve	19	Inlet valve
9	Absorber pipe	20	Inlet pipe
10	Reflecting material	21	Pillow block bearing
11	Glass tube		

Table 2. System characteristics.

No. of PTC modules	2
Concentration Ratio	21
Rim angle	100º
Focal length	0.35 m
Aperture width	1.67 m
Length (per module)	3 m
Total row length	6 m
Total surface area of reflecting mirrors	12 m^2
Total aperture area	10.02 m^2
Tracking axis orientation	North–south
Absorber pipe inner/outer diameter	25/32 mm
Receiver Absorptivity	85%
Mirror Material (Reflectivity)	Stainless steel 68%
Frame material	iron
HTF	Direct steam generation (open feed)

Table 3. Cost analysis of system components.

	Part Name	No. Of Parts Used	Material	Cost (JD Per Part)	Total Cost JD
1	Frame	2	Cast Iron	50	100
2	Mirror Sheet	6	Stainless Steel	30	180
3	Bearing	3	Cast Iron, steel	4	12
4	Pylons Holders	3	Cast Iron	10	30
5	Short Shafts	2	Steel, 1005-1009, Cd	2	4
6	Long Shafts	1	Steel, 1005-1009, Cd	1	1
7	Long bolts	12	Cast Iron	0.02	0.24
8	Short Bolts	6	Cast Iron	0.02	0.12
9	Nuts	6	Cast Iron	0.01	0.06
			Total cost		**327.42**

4.2. Time Constant Testing

An aspect of collector testing is the determination of the heat capacity of a collector in terms of a time constant. It is also necessary to determine the time response of the solar collector in order to be able to evaluate the transient behaviour of the collector and select the correct time intervals for the quasi-steady-state or steady-state efficiency tests. The time constant of a collector is the time required for the fluid leaving the collector to reach 63.2% of its ultimate steady value after a step change in incident radiation. The procedure for performing this test is as follows. The heat transfer fluid is passed through the collector at the same flow rate. The aperture of the collector is shielded from the solar radiation by defocusing the collector and the temperature of the heat transfer fluid at the collector inlet is set approximately equal to the ambient air temperature. When a s teady state has been reached the collector is focused again and measurements continue until steady-state conditions are achieved again. For the purpose of this test, a steady-state condition is assumed to exist when the outlet temperature of the fluid varies by less than 0.05°C per minute. The temperature at 63.2% steady state is given as follows:

$$T_{t=\tau} = 0.632\left(T_{o,steady\ state} - T_i\right) + T_i \qquad (3)$$

where T_i is the inlet temperature

T_o is the outlet temperature, and τ is the time constant.

5. Results

5.1. Time Constant

Figure 10 s hows the temperature response of the collector with three different values of mass flow rates. The average value of the time constant is τ = 4.25 min.

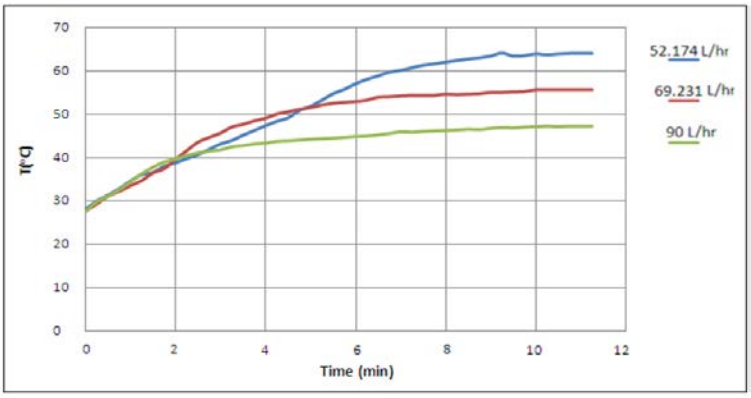

Figure 10. Temperature response of the collector with three different values of mass flow rate.

5.2. Thermal Efficiency

The normal irradiance on t he collector surface was measured to be G_n= 1032 W /m^2, so the thermal efficiency was calculated using equation 1 as:

$$\dot{m} = \frac{69.231L}{hr}, P = 1bar$$

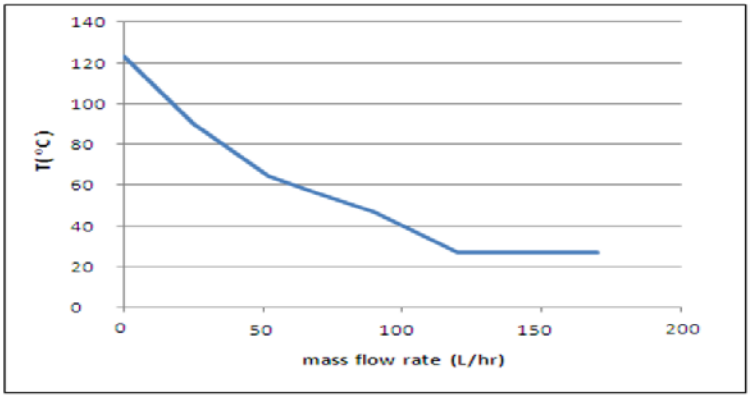

Figure 11. The relation between exit temperature and mass flow rate.

$$\eta_{th} = \frac{(69.23\,l/3600)kg/s(4.186)kJ/kg.K(55.7-27)}{\frac{(1.032)kW}{m^2(1.67\times 6)m^2}} \times 100\%$$

$$= 22.4\%$$

For a fixed inlet temperature of 27 ˚C, the maximum outlet temperature in the test reached 123 ˚C at low flow rate, as shown in Figure 11.

5.3. Steam generation process

The required flow rate to generate steam was 2.642 L/hr, it gave superheated steam at 123˚C and 2 bars. The enthalpies at the inlet and outlet are 113.23 and 2731.15 kJ/kg, respectively. The thermal efficiency for the steam generation can be calculated as the following:

$$\eta_{th} = \frac{\dot{m}\Delta h}{G_b A} = \frac{(2.642/3600)kg/s(2731.15-113.23)kJ/kg}{(0.87)kW/m^2(1.66\times 6)m^2} \times 100\% = 18.6\%$$

The peak thermal efficiency obtained during the test was 22.4%. Steam was generated with temperatures up to 123°C and a pressure of 2 bars at low flow rate of 2.64 L/hr.

6. Conclusion

A parabolic trough solar collector was designed, constructed and tested with acceptable performance and results. The length of the PTC was 6m with an aperture width of 1.67m, a rim angle of 100º and concentration ratio of 21. The surface consisted of 304 AB stainless steel sheets (2×1× 0.00045 m3) and the frame was made of iron tubes. The collector's sun tracking was adjusted manually while ABAQUS software was used for the mechanical design of the bearing structure. The peak thermal efficiency obtained during the tests was 22.4%. Steam was generated with temperatures up to 123˚C and a pressure of 2 bar at low flow rate of 2.64 L/hr.

References

[1] J. A. Duffie and W. A. Beckman, "Solar Engineering of Thermal Processes", Wiley, 2006, p. 928.

[2] A. Fernández-García, E. Zarza, L. Valenzuela, and M. Pérez, “Parabolic-trough solar collectors and their applications”, Renewable and Sustainable Energy Reviews, vol. 14, no. 7, Sep. 2010, pp. 1695–1721.

[3] S. Kalogirou, “The potential of solar industrial process heat applications”, Applied Energy, vol. 76, no. 4, Dec. 2003, pp. 337–361.

[4] D. Krüger, Y. Pandian, K. Hennecke, and M. Schmitz, “Parabolic trough collector testing in the frame of the REACt project,” Desalination, vol. 220, 2008, pp. 612–618.

[5] A. Al-Salaymeh, A. Maytah, and N. Abu Shaban, “CSP Tri-Generation System at Mutah University,” in 1st International Solar Energy Conference, 2012.

JJMIE

Volume 8 Number 1, February. 2014
ISSN 1995-6665
Pages 7 - 12

Jordan Journal of Mechanical and Industrial Engineering

Performance and Combustion Characteristics of a DI Diesel Engine Fueled with Jatropha Methyl Esters and its Blends

Ajay V. Kolhe*, R.E.Shelke and S.S.Khandare

Assistant Professor, Department of Mechanical Engineering, Kavikulguru Institute of Technology & Science, Ramtek-441106, Dist. Nagpur (MS), Govt. ITI Vocational training institute, Daryapur, Dist. Amravati, B.D.College of Engineering Sewagram (Wardha)

Abstract

This study discusses the performance and combustion characteristics of a direct injection diesel engine fueled with Jatropha methyl ester (JME). In order to determine the performance and combustion characteristics, the experiments were conducted at the constant speed mode (1500rpm) under the full load condition of the engine on a single cylinder 4-stroke CI engine. The results indicate that when the test engine is fuelled with JME, the engine performance slightly weakens, the combustion characteristics slightly change when compared to a petroleum based diesel fuel. The biodiesel causes reduction in carbon monoxide (CO), unburned hydrocarbon (HC) emissions, but they cause increases in nitrogen oxides (NOx) emissions.

The useful brake power obtained is similar to diesel fuel for all loads. The oxygen content in the exhaust is more with JME blend due to the fact that fuel itself contains oxygen .The trend of oxygen emission is similar to diesel fuel for all loads. Since JME contains 11% oxygen by weight and this oxygen helps to oxidize the combustion products in the cylinder, especially in rich zones, the addition of JME decreases CO emission. Although there has not been a significant difference in NO_X emissions at part load. NO_x is slightly increased due to the higher combustion temperature and the presence of fuel oxygen with the blend at full load. JME as a new Biodiesel and its blends can be used in diesel engines without any engine modification.

***Keywords**: Biodiesel, Combustion, CI Engine, Jatropha Curcas Oil, Performance and Emission.*

1. Introduction

Increasing global concern due to air pollution caused by internal combustion engines has generated much interest in the environmental friendly diesel fuels. However, increasing number of diesel vehicles will probably bring the same air pollution problem again in the coming years. These forecasts have triggered various research studies in many countries to replace petroleum based diesel fuel with oxygenated fuels such as biodiesel, ethanol, etc. Although the fuel properties of biodiesel show some variations when different feedstocks are used, it has a higher cetane number, near-zero aromatic, and free sulphur, compared to conventional diesel fuel [1]. The fuel properties of biodiesel are affected by its fatty acids content, which causes differences in the injection, combustion, performance and emission characteristics of the engine. Many researchers have concluded that biodiesel holds a promise as an alternative fuel for diesel engines, since its properties are very close to diesel fuel. The fuel properties of biodiesel such as cetane number, heat of combustion, gravity, and viscosity influence the combustion and so the engine performance and emission characteristics because it has different physical and chemical properties from petroleum-based diesel fuel [2]. The combustion timing in CI engines is mainly affected by the start if injection and the ignition delay, which is the time between the start of injection and start of combustion. The ignition delay time is mostly affected by cetane number. The biodiesel has a higher cetane number than diesel fuel; therefore, it shortens the ignition delay time and advances the combustion timing [7].

The objective of the current study is to investigate the use of Biodiesel and to reduce the emissions of all regulate pollutants from diesel engines. A single cylinder, water-cooled constant speed direct injection diesel engine was used for experiments. HCs, NOx, CO, CO_2 of exhaust gas were measured to estimate emission; various engine performance parameters, such thermal efficiency, brake specific fuel consumption, etc., were calculated.

2. Production of Jatropha Methyl Ester from Jatropha Curcas

Jatropha curcus L. is a draught resistant annual shrub that belongs to the family of Euphorbiaceae. The oil has a golden yellow color and is prepared from the seeds of jatropha curcas. These seeds are black in color and oval. Biodiesel, which is synthesized by transesterification of

* Corresponding author. e-mail: *ajay.kolhe4@gmail.com*.

vegetable oils or animal fats sources, is a realistic alternative of diesel fuel because it is produced from renewable resources and involves lower emissions than petroleum diesel. The processed form of vegetable oil (biodiesel) is considered as the potential fuel to replace petroleum diesel in CI engines. In addition, it is biodegradable and contributes a minimal amount of net greenhouse gases or sulfur to the atmosphere [6]. The transesterification process combines the oil with an alcohol. The most common form of biodiesel is made with methanol and vegetable oils in the presence of a suitable catalyst. Additionally, the process yields glycerol. It is derived from crushing the Jatropha seed and by using large mechanical expellers. It is also important to note that most of the experiments conducted on biodiesel are mainly obtained from refined edible type oils only. The price of refined oils such as sunflower, soybean oil and palm oil are high as compared to that of diesel [10].

This increases the overall production cost of the biodiesel as well. Biodiesel production from refined oils would not be viable as well as economical for the developing countries like India. Hence, it is better to use the non-edible type of oils for biodiesel production. In India, non-edible type oil yielding trees, such as linseed, castor, karanji, neem, rubber, jatropha and cashew, are available in large numbers. The production and utilization of these oils are low at present, because of their limited end usage. Utilization of such oils/biodiesel as fuels in internal combustion engines does not only reduce the petroleum usage, but also improves the rural economy. Efforts are made here to produce biodiesel from a refined Jatropha seed oil, and to use it as the fuel in diesel engines.

3. Transesterification Process

JME was synthesized in a reactor vessel using both NaOH & KOH as a catalyst. The ester preparation involved a two-step transesterification reaction followed by washing and drying. The two-step reaction utilized a 100% excess methanol, or a total molar ratio of methanol-to-oil of 6:1 with methanol equally divided in two steps. 1000gm was placed dry flask equipped with a magnetic stirrer and thermometer. In another flask, approximately 300gm of methanol was mixed with 7gm of NaOH until all of the catalyst dissolved.

This mixture was quickly added to the oil and stirred vigorously for 1 hr maintaining temperature 55-60degree Celsius [11]. After 24 hr, ester layer is set up on the upper part and glycerol is set up on the lower part. Then using a separating funnel glycerol is separated and ester is poured into another flask. Finally, the ester is dried by silica gel.

4. Properties of Pure Biodiesel

Table 1. Properties of pure biodiesel

S. N	Properties	ASTM standards	JME100	DIESEL
1	Density in gm/cc	ASTM D4052	0.88	0.825
2	Viscosity in centistoke	ASTM D 445	3.5	2.25
3	Flash point ^{0} C	ASTM D 93	170	66
4	Pour Point ^{0}C	ASTM D 2500	6	10
6	Calorific Value (MJ/Kg.)	ASTM D 6751	38.8	42.00
7	Cetane number	ASTM D 6751-02	52	48

Table 2. Engine Details:

Engine	KIRLOSKAR
General Details	Single cylinder, Four Stroke, CI, Water cooled, TV1
Bore X Stroke	87.5mm X 110mm
Compression Ratio	17.5:1
Capacity	661cc
Rated Output	5.2kW at 1500 rev/min
Injection pressure	200 kg/cm^2
Dynamometer	Rope brake with Mechanical loading

5. Experimental Setup

The experiment was set up using the following equipment. The engine used for experimentation is a Kirloskar make computerised diesel engine used in agricultural applications. The piezo sensor has a range of 5000 PSI. The crank angle sensor has a resolution 1 Deg, speed 5000 rpm with TDC marker pulse. Engine indicator is used for data scanning and interfacing, with speed indicator. Rotameter is used for the water flow measurement. Digital thermocouple type temperature sensors are used as a temperature indicator.

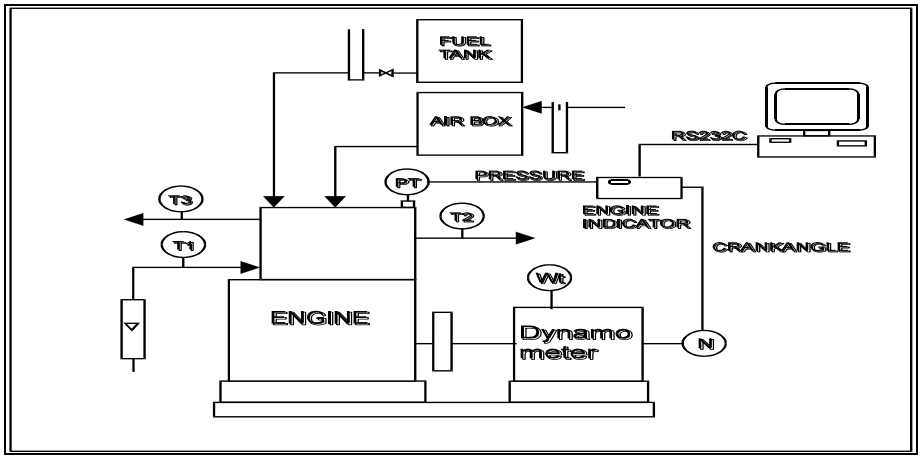

Figure 1. Schematic of Experimental Setup

6. Methodology and Experimental Procedure

Tests have been conducted on a four stroke, direct injection; a naturally aspirated single cylinder diesel engine is employed for the present study. The detail specification of engine is given in table 1. The injection was performed at a static injection timing (optimum) of 23o BTDC set for diesel fuel. To obtain the baseline parameters, the engine was first operated on diesel fuel. Performance and emission tests are carried out on the diesel engine using JME, and its various blends. The tests are conducted at the rated speed of 1500 rpm at various loads and blends are prepared by volume basis, i.e. JME10, JME20, JME30, JME40, JME50. Similar experiments were conducted over the same diesel engine. The experimental data generated are documented and presented here using appropriate graph.

In each experimental phase, the engine parameter is related to the thermal performance of the engine such as brake thermal efficiency; specific fuel consumption and applied load are measured. Mainly, at the given loading conditions, a comparative analysis of the engine performance on the PME, and its blends with diesel and their emission were investigated. Load on the engine is steadily increased.

At each interval, the readings are taken on the manual instrumentation or logged onto the computer analysis software; the variables gathered can then be used with the engine specifications to calculate the characteristics which determine the performance of the fuel on the engine during operation.

Combustion process and Combustion rate in CI engine

Combustion is the process of burning of the fuel in the presence of oxygen to produce heat. The formation of NOx is dependent on the temperatures during the combustion, the amount of O_2 and N_2 in the charge, and the time available for them to react with each other in the combustion chamber. The combustion process in CI engines is mainly divided into three phases. The first phase of combustion is called ignition delay, in which the tiny fuel droplets evaporate and mix with high temperature (or high pressure) air. This period depends mainly on cetane number, and temperatures of fuel and air. The second phase of combustion is called period of rapid combustion or premixed combustion. In this phase, the air-fuel mixture undergoes rapid combustion; therefore, the pressure rise is rapid and releases maximum heat flux. The third phase of combustion is called period of controlled combustion. In this period, the fuel droplets, injected during the second stage, burns faster with reduced ignition delay due to high temperature and pressure. In the third phase, the pressure rise is controlled by the injection rate and the combustion is diffusive mode.

The combustion rate has an effect on NOx production. More premixed combustion means a high initial rate of combustion, which increases NOx. Premixed combustion corresponds to the fuel that is mixed with air and prepared to burn during the ignition delay period. When this fuel auto ignites, it usually burns very quickly. Cetane number and fuel volatility are the two most important properties that determine the combustion rate. A biodiesel with a high cetane number is expected to shorten the ignition delay period and, thus, lower the amount of fuel that is involved with the premixed portion of the biodiesel combustion, thus lowering NOx emission.

7. Results and Discussions

7.1. Engine Performance and Emission Test Analysis

The performance of DI-CI engine was evaluated in terms of fuel consumption, brake specific fuel consumption and brake thermal efficiency, which are discussed as follows:

7.1.1. Brake Thermal Efficiency

The variation of brake thermal efficiency with respect to load for both fuels and their blends is shown in the following graph. Brake thermal efficiency of JME and its blends is slightly lower as compared to that of diesel. The BTE increases as the output power increases for both the fuels.

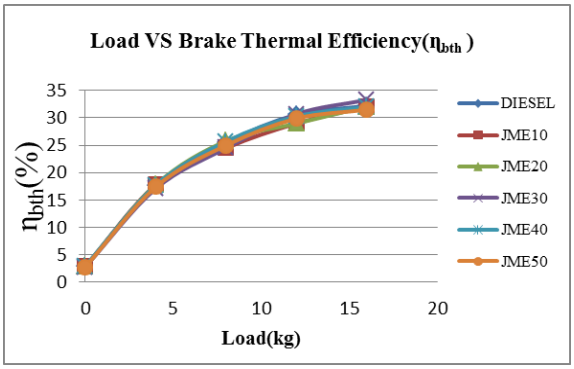

Figure 2. Variation of brake thermal efficiency for JME Blends and diesel

7.1.2. Brake Specific Fuel Consumption

The variation of brake specific fuel consumption with respect to load for both fuels and their blends is shown in the following graph. JME has a lower calorific value than that of the diesel. Hence the specific fuel consumption is higher than that of diesel for JME and its blends. For all loads, the fuel consumption of JME is more than that of diesel. It is also observed that the fuel consumption slightly decreases for lower percentage blends of JME and the reason is attributed to the improved combustion caused by increased evaporation and spray characteristics.

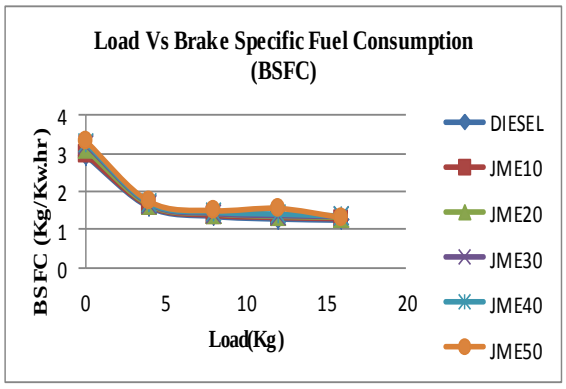

Figure 3. Variation of brake specific fuel consumption for JME blends and diesel.

7.1.3. Indicated Power

The variation of indicated power with respect to load for both fuels and their blends is as shown in the following graph: The indicated power is slightly lower for JME blends than diesel.

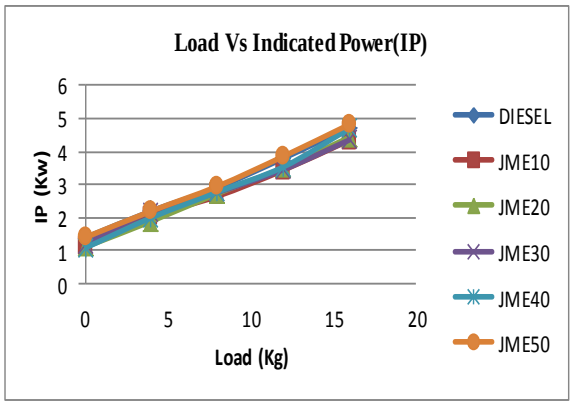

Figure 4. Variation of indicated power for JME Blends and diesel

The biodiesel also contains some amount of oxygen molecule in the ester form. It also takes part in the combustion. For JME20, this reveals that the effective combustion takes place and there is saving with respect to exhaust gas energy loss. This fact is reflected in brake thermal efficiency and brake specific fuel consumption as well.

7.1.4. Mechanical Efficiency

The variation of mechanical efficiency with respect to load for both fuels and their blends is as shown in the following graph. The mechanical efficiency for JME blends and diesel are close to each other.

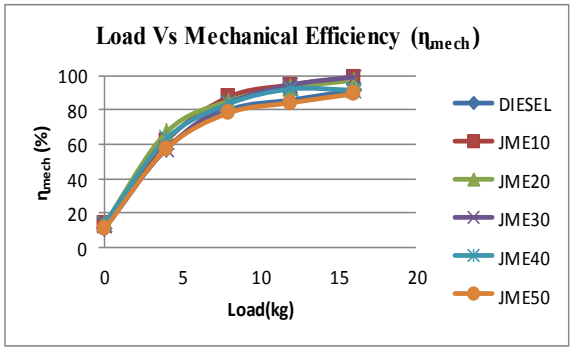

Figure 5. Variation of Mechanical efficiency for JME Blends and diesel

7.1.5. Exhaust Gas Temperature

Figure 6 shows the variation of exhaust gas temperature with load for both fuels and their blends. It is observed that the exhaust gas temperature increases with load because more fuel is burnt at higher loads to meet the power requirement.

It is also observed that the exhaust gas temperature increases with percentage of JME in the test fuel for all the loads. This may be due to the oxygen content of the JME, which improves combustion and thus may increase the exhaust gas temperature.

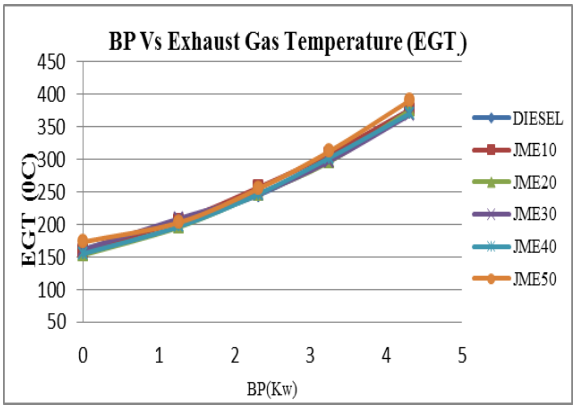

Figure 6: Variation of exhaust gas temperature for JME Blends and diesel

Two fuels and their blends were tested. It is found that specific fuel consumption decreased with the increase in the load. Using lower percentage of JME in JME-diesel blends, the brake specific fuel consumption of the engine is lower than that of diesel for all loads. In case of PME50, the brake specific fuel consumption is found to be higher than that of diesel. At full load condition, the specific fuel consumption of JME is 15% higher than that of the diesel. It may be noted that the calorific values of JME is 7% lower than that of the diesel. With the increase in JME percentage in the blends, the calorific value of fuel decreases.

7.2. Engine Emission Parameters

With problems like global warming, ozone layer depletion and photochemical smog in addition to widespread air pollution, automotive emission are placed under the microscope and every possible method is attempted to reduce emission. Following Engine Emission parameters are evaluated for JME and its blends with diesel.

7.2.1. Carbon Monoxide

The variation of carbon monoxide with respect to load for both fuels and their blends is as shown in the following graph. The formation of CO emission mainly depends upon the physical and chemical properties of the fuel used. It is observed that the CO emission of jatropha biodiesel is less than that of diesel fuel. The decrease in CO emission for JME is attributed to the high cetane number and the presence of oxygen in the molecular structure of the jatropha biodiesel. CO is predominantly formed due to the lack of oxygen. Since JME is an oxygenated fuel, it leads to better combustion of fuel, resulting in the decrease in CO emission.

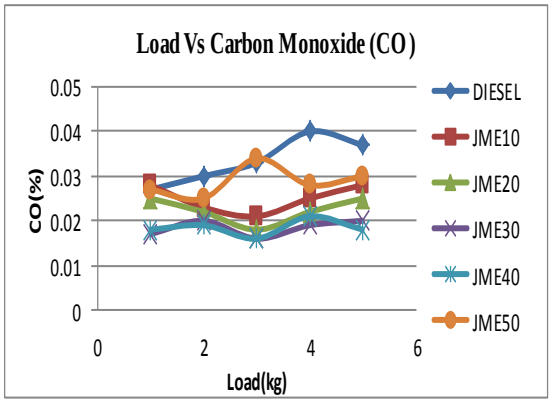

Figure 7. Variation of carbon monoxide for JME Blends and diesel

7.2.2. Hydrocarbons

The variation of hydrocarbons with respect to load for both fuels and their blends is as shown in the following graph. HC emissions reduced drastically, but the higher HC emissions are observed for the blend at low load conditions. At low load conditions, the quantity of fuel injected is lower resulting in a leaner mixture, quenching of flame and lower gas temperature results in incomplete combustion leading to higher HC emissions. The HC emission of the jatropha biodiesel are less than that of diesel fuel due to higher cetane number (52) and inherent presence of oxygen (9%) in the molecular structure of the jatropha biodiesel.

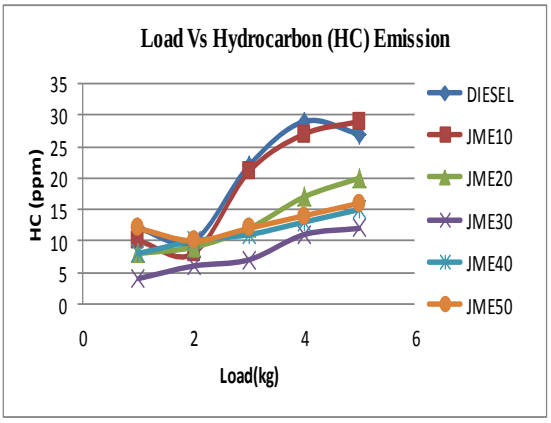

Figure 8. Variation of Hydrocarbons for JME blends and diesel

7.2.3. Carbon Dioxide

Figure 9 shows that, for both fuels, the increasing trend of carbon dioxide (CO_2) emission levels are observed with power output. This increasing trend of CO_2 emission is due to the increase in volumetric fuel consumption. It is observed that the CO_2 emission of jatropha biodiesel is less than that of diesel fuel. This is attributed to the presence of oxygen and high cetane number of jatropha biodiesel.

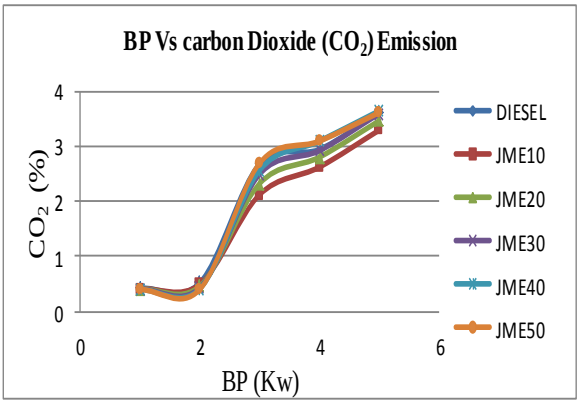

Figure 9. Variation of Carbon dioxide for JME blends and diesel with power output

7.2.4. Nitrogen Oxide

The variation of nitrogen oxide with respect to load for both fuels and their blends is as shown in the following graph and bar chart. Results show, for both the fuels, the increased engine load promoting NOx emission. Since the formation of NOx is very sensitive to temperature, these higher loads promote cylinder charge temperature, which is responsible for thermal (Zeldovich) NOx formation. The jatropha biodiesel produces slightly more NOx than diesel. The increase in NOx emission is attributed to the presence of mono-unsaturated and poly-unsaturated fatty acids present in the jatropha biodiesel. NOx gradually increases with the increase in percentage of PME in the fuel. The NOx increase for JME may be associated with the oxygen content of JME, since the oxygen, present in the fuel, may provide additional oxygen for NOx formation. The formation of NOx emissions are governed mainly by the magnitude of peak cylinder temperature and the crank angle at which it occurs.

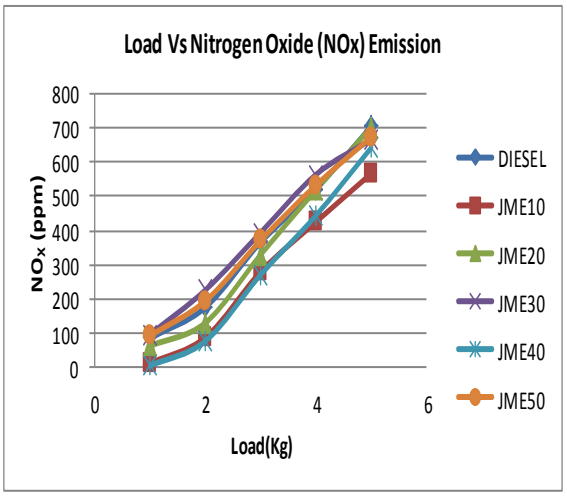

Figure 10: Variation of nitrogen oxide for JME blends and diesel

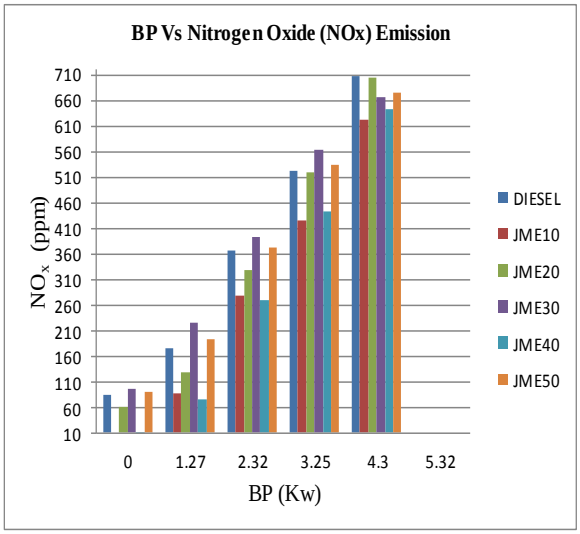

Figure 11: Variation of nitrogen oxide for JME blends and diesel with brake power

8. Conclusion

The performance, emission and combustion characteristics of a single cylinder direct injection CI engine fuelled with JME and its blends have been analyzed and compared to the base line diesel fuel. The results of present work are summarized as follows:

8.1. The specific fuel consumption increases with the increase in the percentage of JME in the blends due to the lower calorific value of JME.

8.2. Methyl ester of Jatropha oil results in a slightly increased thermal efficiency as compared to that of diesel.

8.3. It is also observed that the exhaust gas temperature increases with percentage of JME in the test fuel for all the loads.

8.4. The brake specific fuel consumption values for the engine running with biodiesel are higher than the engine running with normal diesel by a maximum of 10%.

8.5. The tests on engine running with different fuels (biodiesel and diesel) have resulted in almost overlapped P-V diagrams. The engine running with biodiesel has produced slightly higher in-cylinder pressure and peak heat release rate than the engine running with normal diesel.

8.6. CO emission is low at higher loads for methyl ester of Jatropha oil when compared with diesel. The increase in NOx emission of jatropha biodiesel is attributed to the mono and poly unsaturated fatty acids.

8.7. JME satisfies the important fuel properties as per ASTM specification of biodiesel and improves the performance, combustion and emission characteristics of engine significantly.

Acknowledgement

The Authors thank the Management and Principal of Kavikulguru Institute of Technology and Science, Ramtek-441106, Dist. Nagpur, India for providing necessary experimental support to perform this research.

References

[1] Avinash kumar Agarwal., " Biofuels (alcohol and biodiesel) applications as fuels for internal combustion engines," Progress in energy and combustion science 33 (2007) 233-271.

[2] Md. N. Nabi, Md. S. Akhter, M. Shahadat, "Improvement of engine emissions with conventional diesel fuel and diesel-biodiesel blends"., Bioresource Technology 97(2006),372-378.

[3] M.M. Azam, A. Waris, N.M. Nahar, " Prospects and potential of fatty acid methyl esters of some non-traditional seed oils for use as biodiesel in India, Biomass & Biotechnology 29(2005), 293-302.

[4] A.S. Ramadhas, C. Muraleedharan, S. Jayaraj, "Performance and emission evaluation of a diesel engine fueled with methyl esters of rubber seed oil", Renewable Energy 30(2005), 1789-1800.

[5] K. Anand, R.P.Sharma, P.S.Mehta, "Experimental investigations on combustion, performance and emission characteristics of neat karanji biodiesel and its methanol blend in a diesel engine" , Biomass and bioenergy 35 (2011) 533-541.

[6] P.V.Rao, "Experimental investigations on the influence of properties of Jatropha biodiesel on performance, combustion and emission characteristics of a DI-CI engine" , World academy of science, engineering and technology 75 (2011) 855-867.

[7] A.S. Ramadhas, C. Muraleedharan., "Performance and emission evaluation of a diesel engine fueled with methyl esters of rubber seed oil"., RenewableEnergy30(2005),1789-1800.

[8] Mustafa C., Eradil A., Arcaklioglu E., "Performance and Exhaust emissions of a Biodiesel engine", Applied Energy 83(2006),594-605.

[9] Deepak Agrawal, S. Sinha, A. Agrawal, "Experimental investigation of control of NOx emissions in Biodiesel-fueled Compression ignition engine.", 6 December 2005, Renewable Energy.

[10] Mustafa Balat, "Potential alternatives to edible oils for biodiesel production- a review of current work" , Energy conversion and management 52 (2011) 1479-1492.

[11] G.R.Kannan, R.Anand, "Effect of injection pressure and injection timing on Di diesel engine fuelled with biodiesel from waste cooking oil" , Biomass and bioenergy 46 (2012) 343-352.

[12] M.G.Bannikov, "Combustion and emission characteristics of Mustard biodiesel" , 6th International advanced Technologies symposium (IATS'11), 16-18 May 2011, Elazig Turkey, 132-136.

[13] Breda Kegl, "Influence on engine combustion and emission characteristics" , Applied energy 88 (2011) 1803-1812.

[14] K.Muralidharan, D.Vasudevan, "Performance, emission and combustion characteristics of a variable compression ratio engine using methyl esters of waste cooking oil and diesel blend" , Applied energy 88 (2011) 3959-3968.

[15] M.Pugazhvadivu and S. Rajagopan, "Investigations on a diesel engine fuelled with biodiesel blends and diethyl ether as an additive" , Indian journal of science and technology, Volume 2, No 5, May 2009, 31-35.

[16] M.Pugazhvadivu and S. Rajagopan, "Investigations on a diesel engine fuelled with biodiesel blends and diethyl ether as an additive" , Indian journal of science and technology, Volume 2, No 5, May 2009, 31-35.

JJMIE

Volume 8 Number 1, February. 2014
ISSN 1995-6665
Pages 13 -19

Jordan Journal of Mechanical and Industrial Engineering

Gasification of Solid Waste Biomass

Jamil Al Asfar*

Mechanical Engineering Department, The University of Jordan, Amman 11942, Jordan,

Abstract

Gasification of solid waste biomass was performed in this study using an updraft gasifier of a fluidized sand bed with date seeds as fuel and air as fluidizer. The date seeds were washed, dried, crushed and sieved to obtain different particle sizes. The thermo physical properties of date seeds, such as higher heating value, were evaluated experimentally. The fluidization velocity was calculated theoretically to achieve the gasification process of date seed.

It was found that the gasification of date seeds occurred at 550° C temperature with 355-500μm particle size and 2.22 m/s fluidization velocity. The higher heating value of date seed was 17,700 kJ/kg. The carbon content in date seed was little above 50%, which indicates that the solid waste of biomass date seed represents a valuable renewable source of energy in the near future if utilized correctly.

***Keywords**: Gasification, Fluidized Bed, Biomass, Updraft Gasifier*.

Nomenclature

V_{bed}	Volume of bed, [m^3]
V_{sand}	Volume of sand, [m^3]
m	Mass, [kg]
A	Area, [m^2]
h	Height of bed, [m]
ρ_{air}	Density of air, [$\frac{kg}{m^3}$]
ρ_{solid}	Density of solid, [$\frac{kg}{m^3}$]
e_{mf}	Porosity
A	Ash
VM	Volatile material
μ	Dynamic viscosity, [$\frac{N.s}{m^2}$]
$\dot{m}_{air}$	Mass flow rate of air, [$\frac{kg}{s}$]
$(\frac{F}{A})_{stch.}$	Stoichiometric fuel to air ratio, [$\frac{kg\ solid}{kg\ air}$]
$(\frac{F}{A})_{act.}$	Actual fuel to air ratio $\frac{kg\ solid}{kg\ air}$
$\emptyset$	Equivalence ratio
$\dot{m}_{solid}$	Mass flow rate of solid, [$\frac{kg}{s}$]
$\dot{V}_{air}$	Volumetric flow rate of air [$\frac{ft^3}{min}$]
HHV	Higher heating value, [$\frac{kJ}{kg}$]
LHV	Lower heating value, [$\frac{kJ}{kg}$]
DAF	Dry ash free
FC	Fixed carbon

1. Introduction

Biomass is a biological material derived from living, or recently living organisms, that can be harvested as part of a constantly replenished crop. Biomass includes five main categories, which are: virgin wood, energy crops, agricultural residues, food waste and industrial waste. To convert biomass into fuel to produce energy, either direct burning, digestion or gasification is used [1].

Gasification is the process of converting fossil based carbonaceous materials into syngas fuel, which is a mixture of carbon monoxide and hydrogen. This is achieved by incomplete burning of the material at high temperatures without complete combustion, using rich mixture to produce syngas. The power derived from gasification of biomass and combustion of the syngas later is considered a source of renewable energy [2-3].

Janajreh and Al Shrah [4] used downdraft gasification system using wood to investigate its conversion efficiency. Wood chips of 0.5 cm thickness; 1-2 cm width and 2-2.5 cm length constitute the feedstock to the downdraft gasifier. It was found that the conversion rate of wooden pellets increased with increasing air flow, while the heating value of the producer gas reached the maximum value, then decreased as a result of dilution by cold air. Zainal *et. al.* [5] studied the effect of equivalence ratio in downdraft gasifiers on the conversion of wood chips. They found that the hydrogen production increased linearly with the equivalence ratio, whereas carbon monoxide, methane and the calorific value of produced gas reached a maxima, then declined as the equivalence ratio further increased due to the dilution effect of air. It was observed that the phenomenon of bridging which occurs when shredded chips create a bridge that obstructs the continuing flow of

* Corresponding author. e-mail: jasfar@ju.edu.jo.

the wood pellets causing high localized temperatures inside the gasifier. Their work showed that bridging was reduced by using a 60° angled-throat that provides smooth gravitational flow of wood through the combustion zone.

Joardder, Md. Uddin, & M. N. Islam [6] studied the converting of date seed waste into activated carbon and bio-fuel by fixed bed pyrolysis reactor. The date seeds in particle form were pyrolysed in an externally heated fixed bed reactor with nitrogen as the carrier gas. The reactor was heated from 400°C to 600°C. A maximum liquid yield of 50% wt. and char of 30% wt. were obtained at a reactor bed temperature of 500°C with a running time of 120 minutes. The oil is found to possess favorable flash point and reasonable density and viscosity. The higher calorific value was 28,636kJ/kg, which is significantly higher than other biomass derived. Minutillo [7] studied the plasma gasification technology. He developed a thermo chemical model to estimate the syngas composition and the energy required for gasification in plasma arc gasification reactor using air as plasma gas. The model was used to optimize the reactor performance under different operating conditions. M. Erol *et. al.* [8] developed new correlations for calculating the heating values of (20) twenty biomass fuels from their proximate analyses data with measured net heating values varying between 15,410 and 19,520kJ/kg.

The biomass studied included rapeseed, potato peel and soybean cake. The biomass samples were ground and sieved into a powder with a particle size of 0.180–0.250 mm and analyzed to obtain net heating values and contents of moisture, volatile matter, fixed carbon and ash.

Al-Widyan *et. al.* [9] studied direct burning of Jordanian olive cake (OC) in pulverized form in a vertical tube furnace with equivalence ratios from 0.8 to 1.4. The furnace design proved acceptable, and the pulverized OC burned efficiently. The maximum thermal and combustion efficiencies were 69% and 82%, respectively. The maximum flame temperature reached 980℃, and the cooling water temperature gradient was about 20°C. Exhaust gas analyses showed that the concentration of CO was below 1.6%, while the NO_x emission was within 550 ppm and the SO_x maximum concentration was 30 ppm.

In this study, gasification technology of dry updraft type gasification will be implemented to gasify solid waste biomass of date seed.

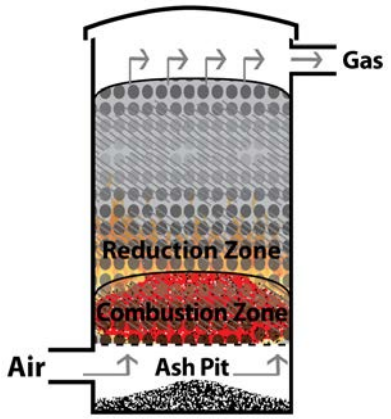

Figure1. Schematic diagram of an updraft gasifier [2].

A schematic diagram of an updraft gasifier is presented in Fig. 1, while Fig. 2 shows the position of biomass compared to coal on the O/C-H/C graph known as Van Krevelen diagram. To convert biomass to useful energy forms, gasification seems to be a promising thermo chemical technology. Physical and Chemical changes that take place during gasification of biomass are similar to typical carbonaceous material decomposition. These changes include drying, devolatilization, heat conduction, fissuring, shrinkage, and fragmentation of solid particles [3].

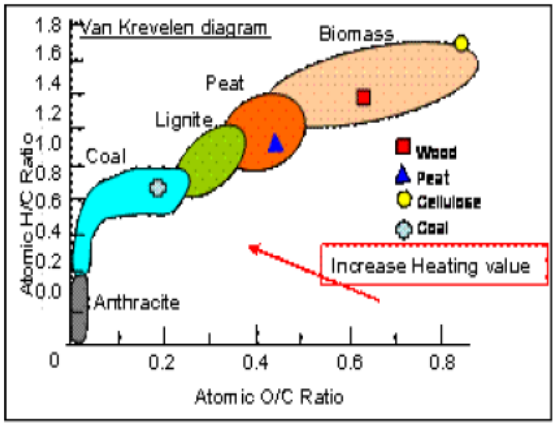

Figure 2. Van Krevelen diagram illustrating the composition and heating value of biomass compared to coal.

2. Theoretical Background

The chemical reaction during which a fuel is oxidized and a large quantity of energy is released is called combustion. The most common oxidizer used is air because it is free and available. Fuel combustion process is complete if all the carbon in the fuel burns to carbon dioxide (CO_2), all the hydrogen burned to water vapour (H_2O), and all the sulfur, if it exists, burns to sulfur dioxide (SO_2). That is, all the combustible components of a fuel are burned to completion during the process. On the other hand, if the fuel combustion process is incomplete, the combustion products contain any unburned fuel or components such as carbon (C), hydrogen ($H_{2(g)}$), carbon monoxide ($CO_{(g)}$), or OH. Gasification is best described as an incomplete combustion process because the products are carbon monoxide and hydrogen gases ($CO_{(g)}$ and $H_{2(g)}$) only. Controlling the air-fuel ratio is the key to have an incomplete combustion process, or gasification [10-11]. The chemical reaction of complete combustion of a fuel composed of carbon and hydrogen only is:

$$C_xH_y + a\,(O_{2(g)} + 3.76\,N_{2(g)}) \rightarrow$$
$$x\,CO_{2(g)} + (y/2)\,H_2O_{(v)} + 3.76a\,N_{2(g)}$$

where; a = x + y/4.

2.1. Fuel-Air Ratio

The mass ratio of the amount of fuel burned to the amount of air used in complete burning of the fuel is called the Fuel-Air ratio (F/A). When burning a solid, the ultimate analysis of the fuel gives the weight percentage of each component of the fuel. The stoichiometric Fuel-Air

$$(F/A)_{stoich.} = \frac{0.232}{2.66C + 7.94H_2 + 0.998S - O_2}$$

ratio is found using the values of fuel components resulting from the ultimate analysis as:

The actual F/A has a different value from the stoichiometric value. The difference between the two values depends on many parameters, such as elevation, pressure and temperature. The ratio between the stoichiometric and the actual Fuel-Air ratios represents the Equivalence Ratio (Ø), found as:

$$Ø = \frac{(F/A)_{actual}}{(F/A)_{stoichiometric}}$$

The equivalence ratio can be less, greater or equal to 1. If (Ø < 1), the actual Fuel-Air ratio is more than the required amount for a complete combustion and the mixture is said to be rich. If (Ø = 1), the actual Fuel-Air ratio is equal to the stoichiometric Fuel-Air and the mixture is said to be stoichiometric. Finally, if (Ø > 1), the Actual Fuel-Air ratio is less than the required amount for complete combustion and the mixture is said to be lean. Gasification seeks a rich mixture to get the unburned elements from the fuel which can be done by increasing the value of the actual Fuel-Air which means (Ø < 1) [10-13].

2.2. Solid Fuels

Solid fuels find little practical applications because of the problems in handling the fuel as well as in disposing off the solid residue or ash after combustion. Compared to gaseous and liquid fuels, solid fuels are difficult to handle. Feeding of a solid fuel in any practical application is quite cumbersome. Due to previous problems and complications in the design of the fuel feed systems, solid fuels have become unsuitable to burn in their solid form, and attempts to generate gaseous and liquid fuels from solid fuels were carried out [10].

2.3. Fluidization of Solids

Burning of solids is much more complicated than burning liquids and gases. Solid fuels may be burned directly, but the most efficient method to burn a solid fuel is the fluidized bed combustion. In fluidized bed combustors, air is blown through the biomass bed. The bed under such conditions behaves like a boiling fluid and has an excellent temperature uniformity. The bed also provides a good contact between gaseous and solid phases. Using fluidized bed combustion to burn solids is preferred for many reasons such as liquid like behaviour is easy to control and automate, rapid mixing, uniform temperature, high rate of heat and mass transfer rates, and applicable for both large and small scale operations [10-12].

Experiments showed that the fluidization velocity is related to the pressure drop of the bed. Fluidization occurs when the upward force exerted by the fluid on the particles is sufficient to balance the net weight of the bed. When this condition is applied, the particles begin to separate from each other and float in the fluid. Fig. 3 shows the relation between the pressure drop and the fluidization velocities [13]:

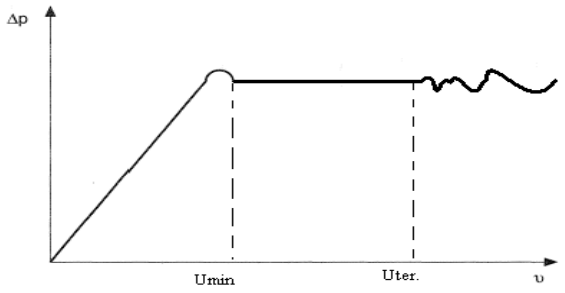

Figure 3: Pressure drop vs. velocity

When burning a solid, the minimum fluidization velocity and the terminal velocity must be known to limit the range of accepted velocity. Any velocity, less than the minimum fluidization velocity, does not give a fluidized bed. Similarly, any velocity, bigger than the terminal velocity, will result in dispersion of bed [12].

In this study, the minimum fluidization velocity and the terminal velocity to limit the range of operation were estimated using the equations below:

2.3.1. Minimum Fluidization Velocity, u_{mf} [12]

The minimum fluidized bed velocity is evaluated as follows:

$$u_{mf} = 0.0055\left(\frac{{e_{mf}}^3}{1 - e_{mf}}\right)\frac{D^2\, g\, (\rho_{solid} - \rho_{air})}{\mu_{air}}$$

Where:

e_{mf} : Porosity of bed, $e_{mf} = \frac{|V_{bed} - V_{solid}|}{V_{bed}}$

Terminal velocity (u_{tf}), $u_{tf} = \frac{D^2\, g\, (\rho_{solid} - \rho_{air})}{18\mu_{air}}$

Desired velocity (u_d), $u_d = \frac{u_{mf} + u_{tf}}{2}$,

which lies in the range of fluidization velocity.

The combustion products from complete combustion of biomass generally contain nitrogen, water vapour, carbon dioxide and oxygen. In gasification, where there is a surplus of solid fuel and due to incomplete combustion, the products are combustible gases like carbon monoxide, hydrogen and traces of methane and other non useful products like tar and dust. The production of these gases takes place by the reaction of water vapour and carbon dioxide through a glowing layer of charcoal. The purpose of the gasifier is to create conditions such that the biomass is reduced to charcoal and charcoal is converted at suitable temperature to produce CO and H_2 [14-16].

2.3.2. Chemical Processes

In this work, an updraft gasifier system was used, with air as the fluidizer and date seed as the fuel. Four processes took place in the updraft gasifier as the fuel makes its way to gasification. These processes are drying, pyrolysis, combustion and reduction. Drying the feed is the main process in this zone. Various experiments on different gasifiers at different conditions have shown that the average condensate formed was about 6-10% of the weight of the gasified feed.

Some organic acids also come out during the drying process. These acids give rise to corrosion of gasifiers. In the pyrolysis process, the products depend upon temperature, pressure and heat losses. Up to 200°C temperature, only water is driven off. Between 200 and 280°C, carbon dioxide, acetic acid and water are driven off. The real pyrolysis, which takes place between 280°C and 500°C, produces large quantities of tar and gases containing carbon dioxide.

The combustion reduction reaction is exothermic and yields a theoretical oxidization temperature. The main reactions are:

$$C_{(s)} + O_{2(g)} = CO_{2(g)}$$
$$2H_{2(g)} + O_{2(g)} = 2H_2O_{(v)}$$

The products of partial combustion are water, carbon dioxide and some pyrolysis products. The pass through a red hot charcoal bed where the following reactions take place:

$$C_{(s)} + CO_{2(g)} = 2CO_{(g)}$$
$$C_{(s)} + H_2O_{(v)} = CO_{(g)} + H_{2(g)}$$
$$CO_{(g)} + H_2O_{(g)} = CO_{2(g)} + H_{2(g)}$$
$$C_{(s)} + 2H_{2(g)} = CH_{4(g)}$$

The first two reactions are the main reductive reactions and they are endothermic, which reduces the gas temperature. Many experiments show that the lower the reduction zone is, the lower the calorific value of the gas [10, 14].

3. Analysis

The experimental feed rate of both date seed particles and air should be estimated carefully to achieve gasification, not combustion. The following procedure shows the theoretical calculation of needed minimum fluidized bed velocity, actual fuel air ratio and mass flow rate of air and date seed particles, taking into consideration the dimension of apparatus and manufactured stainless steel gasifier pipe.

Volume of bed = V_{bed} = h x A_{pipe} = 0.0145 x 5.9x 10^{-4}

= 8.55 x $10^{-6}\ m^3$

Volume of sand = $V_{sand} = \frac{m}{\rho} = \frac{0.02}{1680}$

= 11.964 x $10^{-6}\ m^3$

Porosity = $e_{mf} = \frac{|V_{bed} - V_{sand}|}{V_{bed}}$

$= \frac{|8.55 - 11.964| \times 10^{-6}}{8.55 \times 10^{-6}} = 0.399$

Terminal velocity = $u_{tf} = \frac{D^2\, g\, (\rho_{solid} - \rho_{air})}{18 \mu_{air}} =$

$\frac{(425 \times 10^{-6})(9.81)(1680 - 0.4225)}{18\,(377 \times 10^{-7})} = = 4.3856\ \frac{m}{s}$

Minimum fluidization velocity = u_{mf} =

$0.0055\left(\frac{e_{mf}^3}{1-e_{mf}}\right) \frac{D^2\, g\, (\rho_{solid} - \rho_{air})}{\mu_{air}}$

$= 0.0055\ (\frac{0.399^3}{1-0.399})$ x

$\frac{(425 \times 10^{-6})(9.81)(1680 - 0.4225)}{(377 \times 10^{-7})} = 0.0458\ \frac{m}{s}$

Desired velocity at $550^o C$ = $u_{d@550^o C} = \frac{u_{mf} + u_{tf}}{2}$ =

$2.2157\ \frac{m}{s}$

Air flow rate at $550^o C$ = $\dot{m}_{air@550^o C} = u_d\ \rho_{air@550^o C}\ A_{pipe}$ = 2.2157 x 0.4225 x 5.9 x 10^{-4}

= 5.523 x $10^{-4}\ \frac{kg}{s}$ = $0.5523\ \frac{g}{s}$

Stoichiometric Fuel-Air ratio = $(F/A)_{stch.}$

$= \frac{0.232}{2.66C + 7.94H_2 + 0.998S - O_2} =$

$\frac{0.232}{2.66(0.5084) + 7.94(0.0683) + 0.998(0) - 0.3788} = 0.153\ \frac{kg\ solid}{kg\ air}$

Gasification seeks a rich mixture ($\emptyset > 1$), values of the actual Fuel-Air ratio $(F/A)_{act}$ defers linearly with the equivalence ratio. Many tests were done with different values of equivalence ratio to change the actual Fuel-Air ratio and find the most suitable value for gasification. It was found that at ($\emptyset$ = 1.49), gasification can be noticed and the parameters can be read easily by the gas analyzer. The relation between the actual Fuel-Air ratio and the equivalence ratio is plotted in Fig. 4 using the value of $(F/A)_{stch.}$ = $0.153\ \frac{kg\ solid}{kg\ air}$ as constant.

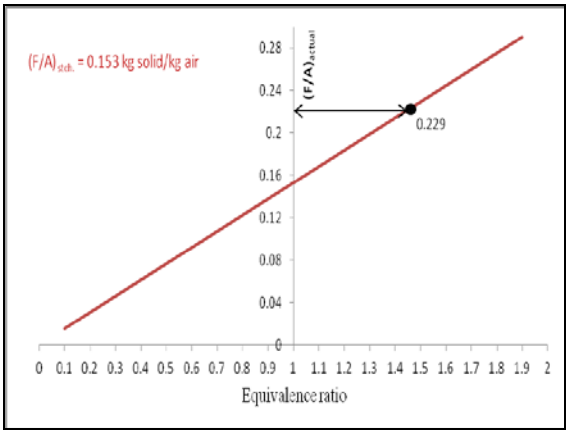

Figure 4. Actual fuel-air ratio vs. equivalence ratio

4. Experimental Work

The updraft gasifier was used in this work to gasify date seed. This gasifier, as shown in Fig. 5 and Fig 7, consists of a stainless steel pipe of 27.5 mm diameter that has a steel mesh welded above the bottom. The steel mesh has 600 holes to allow air to pass through it. Sand grains

were put on the mesh to form the fluidized bed. Fluidization occurs when air passes through the bed of sand at a specified velocity. The pipe was heated to 550^{o}C, and then feed falls on the bed to allow the gasification process to take place. The gas produced is taken from a small outlet at the top of the pipe. A gas analyzer is used to estimate the percentage composition of the gases with time. The temperature of the bed was measured every second of the experiment using a thermocouple that is inserted into the pipe.

4.1. Preparation of Date Seed

4.1.1. Drying:

The first step in preparing the date seed was to dry them in an oven at 105° C for two hours. Drying was done to get rid of the moisture inside the seed and to prevent it from kneading when crushed.

4.1.2. Crushing:

After drying, the seed were crushed in a Jaw Crusher machine to prepare for sieving them in different particle sizes.

4.1.3. Sieving:

Separating each particle size from another is done using the shaker. The smallest sieve size is put in the bottom while the biggest sieve is put on the top as shown in Fig.5.

Figure. 5. Sieving shaker machines.

4.2. Thermophysical Properties of Date Seed

Proximate analysis and ultimate analysis were carried out to find the Fuel-Air ratio of the gasification process of date seed. Other thermophysical properties of date seed were estimated experimentally and are given in table 1. The density of date seed particles was determined using Archimedes method of volumes by the displacement of water; since the fluidization velocities calculation uses the true density which does not include the voids between the particles. So, this method was used because it finds the volume of the particles only and the voids are filled with water.

4.3. Updraft Gasifier

The combustion chamber was manufactured from a stainless steel pipe of a circular cross section area. Air enters from the bottom of the pipe through a small lane and passes through an iron mesh where the bed of sand lies. Feed is introduced manually from the top by another lane to be gasified. The pipe was heated in an oven for 24 hours to get rid of the dust and other dirt in the holes of the iron mesh and to prevent any obstacles to stand in the air path.

Table 1. Ultimate (dry, Ash free basis) and proximate (as received) analyses of date seed

Analysis	**wt %**
Ultimate:	
C	50.84
H	6.83
N	4.45
S	0.00
O	37.88
Proximate:	
Fixed carbon	16.311
Volatile matter	77.699
Moisture	5.01
Ash	0.98
Density, kg/m^3	1680
LHV, kJ/kg	16400
HHV, kJ/kg	17700

Product gases from the gasification process are taken from the pipe outlet directly to a cooling basin. The gas passes through a cylindrical glass pipe filled with small crushed pieces of cut glass. The cut glass is inserted into the glass pipe to increase the passing area of gases. To determine the concentrations of each combustible species, a gas analyzer was connected to the cooling basin. The measurement of the volumetric concentration of $O_{2(g)}$, $CO_{(g)}$ and $CO_{2(g)}$ were recorded during the gasification process.

The temperature of the fluidized bed during gasification was measured and recorded using a thermocouple of type “K” and a data logger to study the variation of the temperature of the fluidized bed with time from the beginning of feed entering until the gas analyzer rests. The gas analyzer used and gasification complete system are shown if Fig. 6 and Fig. 7.

Figure 6. Gas Analyzer

  - Volume 8, Number 1 (ISSN 1995-6665)

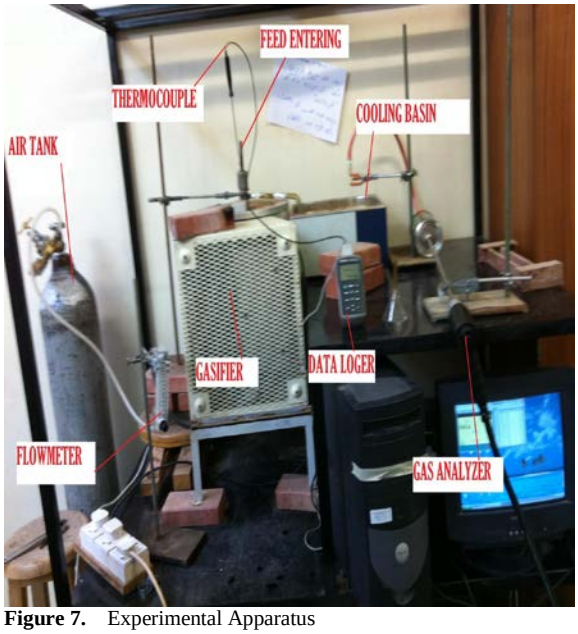

Figure 7. Experimental Apparatus

5. Results

The following figures represent the main findings of this work. These figures show the fluidized bed temperature, the concentration of oxygen and carbon monoxide during the gasification process.

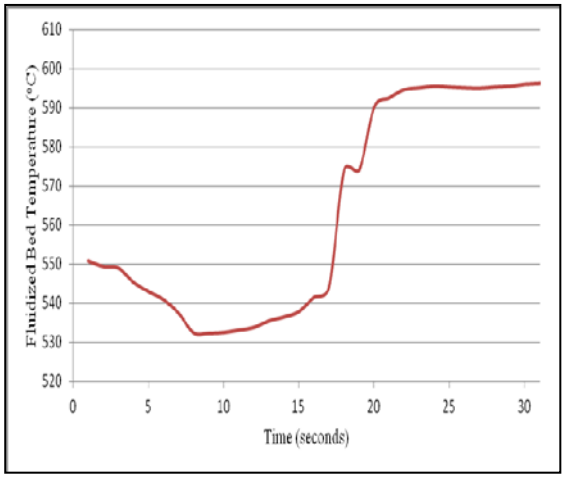

Figure 8. Fluidized bed temperature with time

It is noticed from Fig. 8 that the temperature of the fluidized bed decreased in the first stages of feeding due to heat transferred from the bed to the seed. While it started to increase up to 595° C when gasification occurred since the chemical reaction of gasification is exothermic. This also indicates that complete combustion did not take place; otherwise the temperature will increase to higher values.

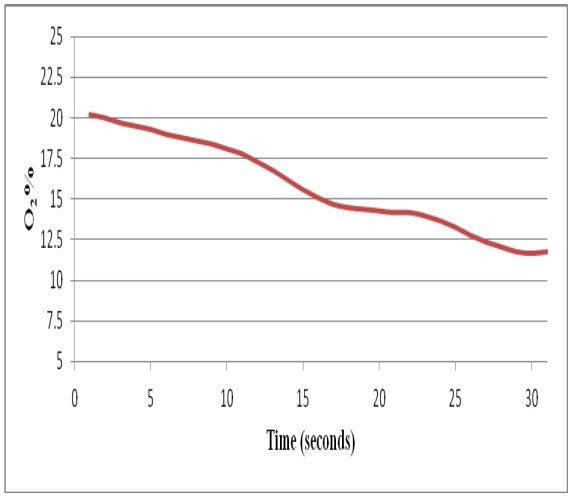

Figure 9. Oxygen concentration with time

From Fig. 9, it is seen that the level of oxygen, $O_{2(g)}$ decreased with time which indicates clearly that gasification is going on.

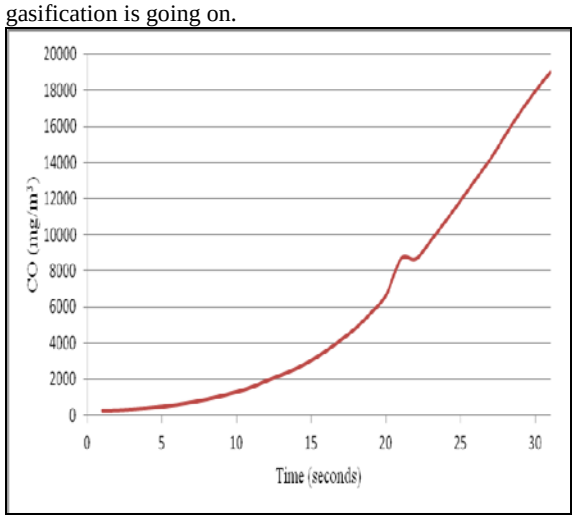

Figure 10. Volumetric concentration of $CO_{(g)}$ with time

Fig. 10 shows that the volumetric concentration of carbon monoxide, $CO_{(g)}$ has increased. This increase is not due to dissociation of carbon monoxide; since the temperature did not reach 850° C. This increase assures that gasification, not combustion, occurred successfully in this work.

6. Conclusion

In this study, the use of an updraft gasifier, with a fluidized sand bed to gasify date seed, proved to be a successful method to utilize agricultural solid waste. It was also found that the higher heating value of date seed reached 17,700kJ/kg, while the gasification process took place at 550° C temperature with 355-500μm particle size and 2.2157 m/s fluidization velocity. This ensures that solid waste of bio mass represent a valuable renewable source of energy in the near future if utilized correctly.

References

[1] O. Senneca. "Kinetics of pyrolysis, combustion and gasification of three biomass fuels". Fuel Processing Technology, 88(1), 2007, 87-97.

[2] Gek Wiki sandbox, http://www.gekgasifier.com /info/ gasification-basics/gasifier-types, retrieved February 13th, 2014.

[3] P. McKendry. "Review paper: Energy production from biomass (part 3): Gasification technologies". Bioresour. Technol., 83, 2002, 55-63.

[4] Janajreh, and M. Al Shrah. "Numerical and experimental investigation of downdraft gasification of wood chips". Energy Conversion and Management, volume 65, 2013, 783-792.

[5] Z. A. Zainal, A. Rifau, G. A. Quadir, and K. N. Seetharamu, "Experimental investigation of a downdraft biomass gasifier". Biomass and Bioenergy, 23(4), 2002, 283-289.

[6] M. U. H. Joardder, Md. S. Uddin and M. N. Islam, "The Utilization of Waste Date Seeds as Bio-Oil and Activated Carbon by Pyrolysis Process", Rajashi University, Rajashi 6204, Bangladesh. 2011.

[7] M. Mintillo, A. Perna, D. Di Bona, "Modelling and Performance analysis of an Integrated Plasma Gasification Combined Cycle Power Plant". Energy Conversion and Management, 2009, 2837-2842.

[8] M. Erol, H. Haykiri-Acma, S. Ku¨ cu¨ kbayrak, "Calorific value estimation of biomass from their proximate analyses data". Renewable Energy 35, 2010, 170–173.

[9] M. I. Al-Widyan, G. Tashtoush and A. M. Hamasha, "Combustion and emissions of pulverized olive cake in tube furnace". Energy Conversion and Management 47, 2006, 1588–1596.

[10] Stephen R. Turns. An Introduction to Combustion. 2nd edition. McGraw-Hill, 2000.

[11] Archie W. Culp. Principles of Energy Conversion. 2nd edition. McGraw-Hill. 1991

[12] Kunii, D. and Levenspiel, O. Fluidization Engineering, 2nd edition. Boston: Butterworth-Heinemann. 1991.

[13] Yunus A. Cengel and Micheal A. Boles. Thermodynamics: An Engineering Approach. 7th edition, McGraw-Hill. 2011.

[14] Richardson, Coulson and Harker. Chemical Engineering: Particle Technology and Separation Process. 3rd edition, Elsevier Ltd. 2007.

[15] Yogi Goswami. Alternative Energy in Agriculture. Elsevier Ltd. 1986.

[16] K.J. Ptasinski, M.J. Prins and Pierik, "Exergitic evaluation of biomass gasification", Energy, 2007, 568-574.

JJMIE

Volume 8 Number 1, February. 2014
ISSN 1995-6665
Pages 21- 26

Jordan Journal of Mechanical and Industrial Engineering

A New Method for Calculating Notch Tip Stresses and Strains Based on Neuber Method and ESED Method under Multiaxial Loading

Liu Jianhui*, Wang Shengnan, Su Yi

School of aeronautics, Northwestern Polytechnical University 127 Youyixi Road, xi'an shaanxi, 710072, P.R.China

Abstract

A modified version of Neuber method and ESED method for calculating elasto-plastic notch tip stresses and strains in bodies subjected to proportional multiaxial loading, in which only the heat energy is considered as a dissipation and the stored energy is regarded as a contribution to local stress and strain ranges, has been developed in this paper. The method considers the material constant of yield stress in response to the difference between before and after the plastic phase. This approach makes the calculated results tend to be more precise and reveals its energy meaning, considers the elastic-plastic properties of material itself and avoids the blindness of selecting coefficient values. Finally, the calculated results using modified model are validated with the Finite Element Method. It is shown that, for the case of cyclic loading, the modified method further improves the accuracy of the original Neuber method and ESED method in predicting the nonlinear stress-strain behavior of notches. It is also shown that the modified model proposed in this paper can easily be used for a calculation of the local stress-strain relationship.

***Keywords**: Neuber Method; Equivalent Strain Energy Density Method; Notch Tip Stresses and Strains; Proportional Loading, Finite Element Method.*

1. Introduction

There are various kinds of notches in engineering applications, which lead to stress concentration. The mechanical structures in practical application mostly work under cyclic loading. The loading mode may be uniaxial cyclic loading, or likely to be multiaxial cyclic loading [1]. Fatigue life prediction of notched components in complex service conditions requires the local stress-strain relationship to be known. Although accurate calculations are not intractable, they are difficult and lengthy especially for a long arbitrary cyclic loading. Therefore, approximate methods [2-3] are widely used in engineering practice. So far, a few approximate methods [4-6] for description of the nonlinear stress-strain behavior of notches have been developed. Ayhan Ince and Grzegorz Glinka [7] has developed a computational modeling method of the multiaxial stress-strain notch analysis to compute elastic-plastic notch-tip stress-strain responses using linear elastic finite element results of notched components. In this paper, a modified method is proposed considering the material constants of yield stress. The benefit of this approach is to consider the elastic-plastic properties of material itself and avoid the blindness of selecting coefficient values. The Neuber method and ESED method were used to calculate the stresses and strains at the notch tip of the LD5 shaft under the tensile-torsional proportional loading. A modified model was proposed to calculate the stresses and strains of the same specimen on the basis of the analysis of the above methods [8-9].

It was proved that the proposed modified model is available and practicable by the comparing the calculated results with the FEM results.

2. Stress-Strain Analysis and Constitutive Relations

When the stress range of notch tip is under the uniaxial state, the state of stress and strain can be expressed as:

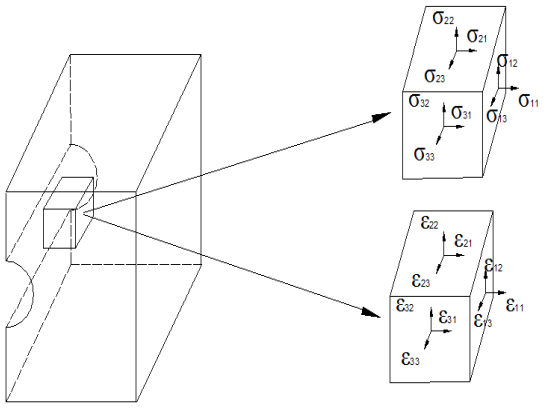

Figuer1. Notch tip stress and strain state

$$\sigma_{ij}=\begin{bmatrix}0&0&0\\0&\sigma_{22}&0\\0&0&0\end{bmatrix}\quad \varepsilon_{ij}=\begin{bmatrix}\varepsilon_{11}&0&0\\0&\varepsilon_{22}&0\\0&0&\varepsilon_{33}\end{bmatrix} \tag{1}$$

* Corresponding author. e-mail: liujianhui2010@163.com.

At the same time, in the case of multiaxial loading, the state of stress and strain can be represented as:

$$\sigma_{ij}=\begin{bmatrix}0 & 0 & 0\\ 0 & \sigma_{22} & \sigma_{23}\\ 0 & \sigma_{32} & \sigma_{33}\end{bmatrix}\quad \varepsilon_{ij}=\begin{bmatrix}\varepsilon_{11} & 0 & 0\\ 0 & \varepsilon_{22} & \varepsilon_{23}\\ 0 & \varepsilon_{32} & \varepsilon_{33}\end{bmatrix} \tag{2}$$

The elastic-plastic stress-strain constitutive relation is usually derived from uniaxial stress strain curve based on elastic-plastic theory and it can be written as:

$$\varepsilon_{ij}=\frac{1+\nu}{E}\sigma_{ij}-\frac{\nu}{E}\sigma_{kk}\delta_{ij}+\frac{3}{2}\frac{\varepsilon^{p}_{eq}}{\sigma_{eq}}S_{ij} \tag{3}$$

where ν is poisson's ratio, E is elastic modulus, ε_{ij} are the strain components, σ_{ij} are the stress components, δ_{ij} is Karen Necker coefficient, σ_{eq} is the equivalent stress, ε^{p}_{eq} is the equivalent plastic strain and S_{ij} are stress deviators.

$$\sigma_{eq}=\sqrt{\frac{3}{2}S_{ij}S_{ij}}\ ,\ \varepsilon^{p}_{eq}=\sqrt{\frac{2}{3}\varepsilon^{p}_{ij}\varepsilon^{p}_{ij}}\ ,$$

$$S_{ij}=\sigma_{ij}-\frac{1}{3}\sigma_{kk}\delta_{ij}\ ,$$

$$\sigma_{kk}=\sigma_{11}+\sigma_{22}+\sigma_{33}\ ,\ \varepsilon^{p}_{eq}=f\left(\sigma_{eq}\right).$$

Here, $f\left(\sigma_{eq}\right)$ is the function of stress and plastic strain in the case of uniaxial tension and compression.

3. Neuber Method

The Neuber rule was initially proposed for a notched body under pure shear stress state, but is most often used for notches under a tensile or bending load (Fig. 2). Neuber rule is written in the form of eq.(4) which relates the theoretical stress concentration K_t, the actual stress concentration K_σ and the actual strain concentration K_ε factors:

$$K_t^2=K_\sigma K_\varepsilon \tag{4}$$

where :

$$K_t=\frac{\sigma^{e}_{22}}{\sigma_n},\ K_\sigma=\frac{\sigma^{N}_{22}}{\sigma_n},\ K_\varepsilon=\frac{\varepsilon^{N}_{22}}{\varepsilon_n},\ \varepsilon_n=\frac{\sigma_n}{E} \tag{5}$$

where, K_t is the theory elastic stress concentration factor, K_ε is the strain concentration factor, K_σ is the stress concentration factor, σ_n is the nominal stress, superscript e represents the corresponding item analyzed by linear elastic and superscript N represents the corresponding item calculated by Neuber rule.

In the case of notched bodies in plane stress resulting in an uniaxial stress state in the notch tip, Neuber's rule eq.(4) can also be written in the form which relates the elasto-plastic strain ε^{N}_{22} and stress σ^{N}_{22} components to the hypothetical linear elastic notch tip strain ε^{e}_{22} and stress σ^{e}_{22}.

$$\sigma^{e}_{22}\varepsilon^{e}_{22}=\sigma^{N}_{22}\varepsilon^{N}_{22} \tag{6}$$

Thus, when the notch tip is subjected to a uniaxial stress state (as in plane stress), eq.(6) represents the equality of the total strain energy density at the notch tip as shown in Fig.3. The total strain energy density is defined as the sum of the strain energy density and the complementary energy density. A relationship similar to eq.(6) can also be written for notched bodies in strain.

There are three stress components and four strain components when the structures are subjected to multiaxial loading. That is to say, there are a total of seven unknown parameters. However the constitutive equations can only provide four equations. Therefore three additional equations are required. Eq.(6) can be expanded in the case of multiaxial loading and its tensor form is given by

$$\sigma^{e}_{ij}\varepsilon^{e}_{ij}=\sigma^{N}_{ij}\varepsilon^{N}_{ij}\qquad \text{i,j=1,2,3} \tag{7}$$

It has been proved that this equation has energy meaning. Fig.2 shows that, in the case of uniaxial stress state (such as plane stress), the total strain energy density in plastic state equals to that in the linear elastic state, namely the rectangular AFOH and the rectangular BEOM have the same area.

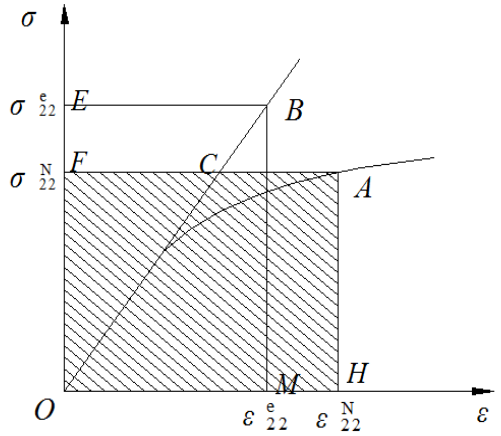

Figuer2. Principle of Neuber Method

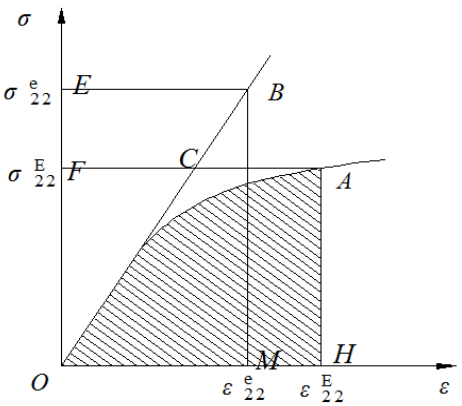

Figuer3. Principle of ESED Method

It has been reported that it is more convenient to describe Eq.(7) using the principal stress and strain in the case of proportional loading, so there are five unknown parameters and five equations are required. Then Eq.(7) can be rewritten as:

$$\sigma_2^e\varepsilon_2^e+\sigma_3^e\varepsilon_3^e=\sigma_2^N\varepsilon_2^N+\sigma_3^N\varepsilon_3^N \tag{8}$$

Meanwhile it has been experimentally proven that in the case of multiaxial loading the stress and strain distribution ratio can be assumed as:

$$\frac{\sigma_2^e\varepsilon_2^e}{\sigma_2^e\varepsilon_2^e+\sigma_3^e\varepsilon_3^e}=\frac{\sigma_2^E\varepsilon_2^E}{\sigma_2^E\varepsilon_2^E+\sigma_3^E\varepsilon_3^E} \tag{9}$$

The constitutive equations can provide the following three equations:

$$\varepsilon_1^N=-\frac{v}{E}\left(\sigma_2^N+\sigma_3^N\right)-\frac{f\left(\sigma_{eq}^N\right)}{2\sigma_{eq}^N}\left(\sigma_2^N+\sigma_3^N\right) \tag{10}$$

$$\varepsilon_2^N=\frac{1}{E}\left(\sigma_2^N-v\sigma_3^N\right)+\frac{f\left(\sigma_{eq}^N\right)}{2\sigma_{eq}^N}\left(2\sigma_2^N-\sigma_3^N\right) \tag{11}$$

$$\varepsilon_3^N=\frac{1}{E}\left(\sigma_3^N-v\sigma_2^N\right)+\frac{f\left(\sigma_{eq}^N\right)}{2\sigma_{eq}^N}\left(2\sigma_3^N-\sigma_2^N\right) \tag{12}$$

where:

$$\sigma_{eq}^N=\sqrt{\left(\sigma_2^N\right)^2-\sigma_2^N\sigma_3^N+\left(\sigma_3^N\right)^2}$$

So Eqs.(8-12) can be employed to calculate the stresses and strains by Neuber method.

4. ESED Method.

The equivalent strain energy density (ESED) relationship was initially proposed [15] for a notched body in plane stress, and is given as an equality of strain energy densities at the notch tip by Molski, Glinka et al.[16-17], which is based on the assumption that the strain energy density distribution in the plastic zone ahead of a notch tip is the same as that determined on the basis of the pure elastic stress-strain solution. In the case of monotonic loading and uniaxial stress condition at the notch tip, ESED method can be expressed in the form

$$\int_0^{\varepsilon_{22}^e}\sigma_{22}^e d\varepsilon_{22}^e=\int_0^{\varepsilon_{22}^E}\sigma_{22}^E d\varepsilon_{22}^E \tag{13}$$

where superscript E represents the corresponding item calculated by ESED method.

Fig.3 shows that the strain energy density equals to that in elastic state although the stress range of notch is in the plastic region, namely the shadow area and the triangle area OBM are equal. The equivalent strain energy density method needs the following expression to solve the problem under multiaxial loading

$$\frac{1}{2}\left(\sigma_2^e\varepsilon_2^e+\sigma_3^e\varepsilon_3^e\right)=\frac{1}{3E}(1+v)\left(\sigma_{eq}^E\right)^2+\frac{1-2v}{6E}\left(\sigma_2^E+\sigma_3^E\right)+\int_0^{\varepsilon_{eq}^{pE}}\sigma_{eq}^E d\varepsilon_{eq}^{pE} \tag{14}$$

where

$$\varepsilon_{eq}^{pE}=f\left(\sigma_{eq}^{pE}\right),\quad \sigma_{eq}^E=\sqrt{\left(\sigma_2^E\right)^2-\sigma_2^E\sigma_3^E+\left(\sigma_3^E\right)^2}$$

Similarly the stress and strain distribution ratio can be given as:

$$\frac{\sigma_2^e\varepsilon_2^e}{\sigma_2^e\varepsilon_2^e+\sigma_3^e\varepsilon_3^e}=\frac{\sigma_2^E\varepsilon_2^E}{\sigma_2^E\varepsilon_2^E+\sigma_3^E\varepsilon_3^E} \tag{15}$$

Therefore Eqs.(14-15) and constitutive equations are used to calculate the stresses and strains by ESED method.

5. Modified Model

On the basis of the analysis of results of notch tip subjected to multiaxial loading, a quantitative relationship between Neuber method and the equivalent strain energy density (ESED) method is found. It is shown that, in the case of elastic range, both Neuber method and ESED method get the same estimation of the local stresses and strains, whereas in the case of elastic-plastic range, Neuber method normally overestimates the notch tip stresses and strains, while ESED method tends to underestimate the notch tip stresses and strains. In other words, the upper limit of the stresses and strains can be obtained by Neuber method and the lower limit is given by ESED method. Through the above analysis, the following points can be given: first, the yield strength limit should be reflected in response to the difference between before and after the plastic phase; secondly, the results calculated by modified model should locate between the upper limit and lower limit in order to avoid large errors of calculated results. So calculation model should be modified based on the above two reasons [18-19].

Providing the further quantitative analysis for Fig.2 and Fig.3 and considering the stress-strain relationship, it can be found that the shaded area calculated by Neuber method is larger than that calculated by the equivalent strain energy density method. Difference area roughly equals to trapezoidal area BCFE (Fig.4), which provides the idea to modify the stress and strain calculation model under multiaxial loading.

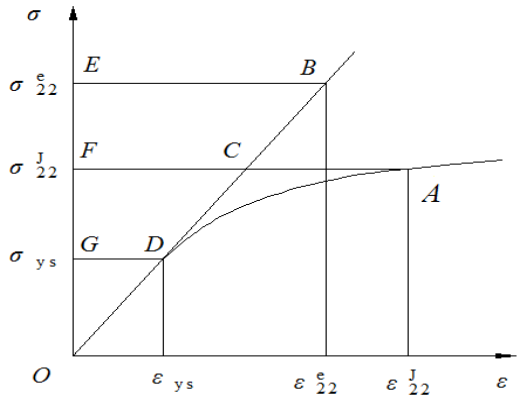

Figuer4. Principle of Modified Model

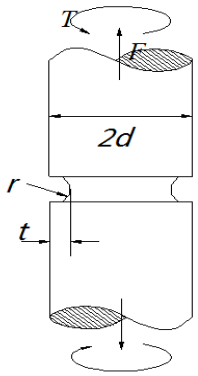

Figuer5. Shape and Dimensions of Specimen

In this paper, the essence of the modified model is based on Neuber method and ESED method. According to the above analysis, the results calculated by modified model should locate between the results calculated by Neuber method and ESED method. Then calculation model is processed by using the principal stress and strain:

$$\left(\frac{\sigma_{ys}}{\sigma_2^e}\right)^2\left(\sigma_2^e\varepsilon_2^e+\sigma_3^e\varepsilon_3^e\right)=\frac{1}{2}\left[\frac{2}{3E}(1+v)\left(\sigma_{eq}^E\right)^2+\frac{1-2v}{3E}\left(\sigma_2^E+\sigma_3^E\right)+2\int_0^{\varepsilon_{eq}^{pE}}\sigma_{eq}^E d\varepsilon_{eq}^{pE}+\sigma_2^N\varepsilon_2^N+\sigma_3^N\varepsilon_3^N\right] \quad (16)$$

In this paper the yield strength of material should be defined as:

$$\sigma_{ys}=\sigma_{ys}\left(\sigma_{ys}\le\sigma_2^e\right)$$
$$\sigma_{ys}=\sigma_2^e\left(\sigma_{ys}>\sigma_2^e\right) \quad (17)$$

The modified model makes the calculated results tend to be more precise and reveals its energy meaning. Similarly, the distribution ratio can be assumed as

$$\frac{\sigma_2^e\varepsilon_2^e}{\sigma_2^e\varepsilon_2^e+\sigma_3^e\varepsilon_3^e}=\frac{\sigma_2^J\varepsilon_2^J}{\sigma_2^J\varepsilon_2^J+\sigma_3^J\varepsilon_3^J} \quad (18)$$

Therefore Eq(16), Eq.(18) and constitutive equations enable the notch tip stress and strain components to be calculated.

6. Application Example

The shape and dimensions of specimen are simplified as shown in Fig.5 and the material constants of LD5 aluminum alloy are listed in table 1

Table 1. Material Constants of LD5 Aluminum Alloy

elastic modulus, E	68GPa
shear elastic modulus, G	26GPa
yield stress, σ_{ys}	120Mpa
yield strain, ε_y	0.004
poisson's ratio, υ	0.3

It is easily obtained that σ_{nF} and τ_n can be calculated by the formula as follows:

$$\sigma_{nF}=\frac{F}{\pi(d-t)^2},\quad \tau_n=\frac{2T}{\pi(d-t)^3} \quad (19)$$

where, $\tau_n=2.5\sigma_{nF}$, σ_{nF} is nominal stress under loading F, τ_n is nominal shear stress, F is axial loading, D is cylinder radius, t is the depth of the notch, R is radius of notch and T is torque.

The finite element method (FEM) has a widespread application in engineering because of its high precision and economy. Finite element model, boundary conditions and loading process, which directly affects the calculation of the degree of correctness and precision, should close to the actual situation of the project as much as possible, so that the results can be more accurate. Comparing with the eight-node hexahedral elements, the twenty- node hexahedral element, which is an advanced unit setting up on the basis of eight-node hexahedral elements using for the analysis of structure, is more suitable for high precision. In this paper, the ANSYS software is used and element unit is SOLID95. The stresses and strains can be read from ANSYS results(Fig.6 and Fig.7).

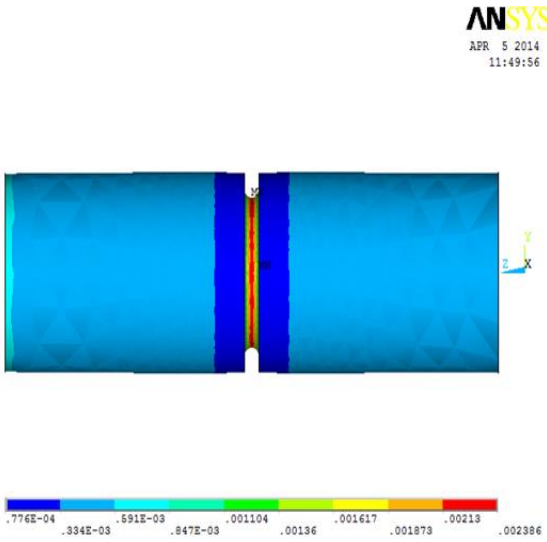

Figuer6. Equivalent stress under multiaxial loading

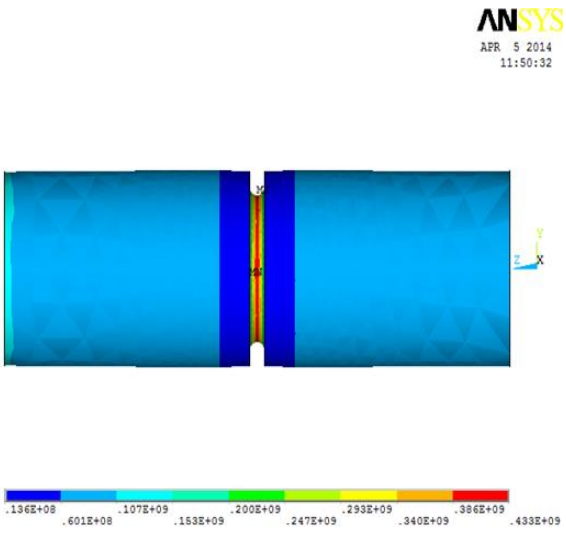

Figuer7. Equivalent strain under multiaxial loading

The stresses and strains can also be calculated by Neuber method, ESED method and modified model. The calculated results using above three methods are compared with the FEM results, and the comparison are shown in Fig.8 and Fig.9:

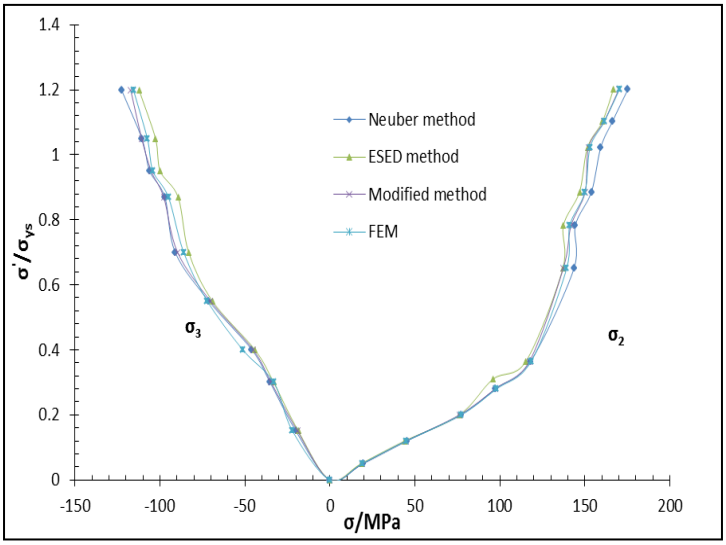

Figuer8. comparison of stress between different methods

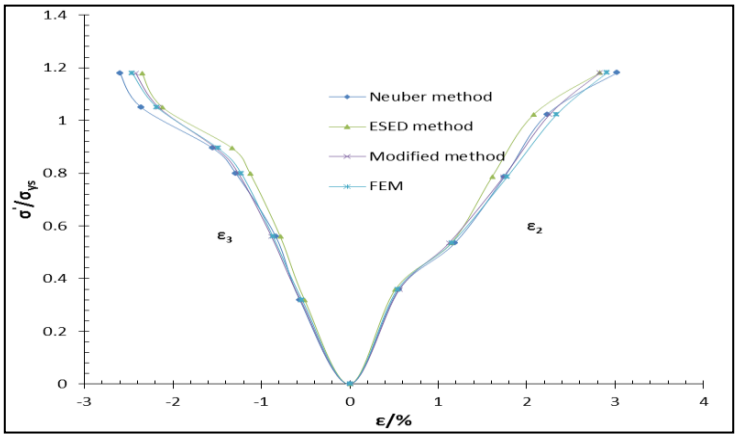

Figuer9. comparison of strain between different methods

Fig. 8 and Fig. 9 show the plots of the calculated and measured local stress and strain amplitude against the ratio of the average nominal stress S' to yield stress σ_{ys} and $S' = \sqrt{\sigma_{nF}^2 + 3\tau_n^2}$. It is obvious from the figures that the results calculated by Neuber method are slightly larger than FEM results, namely Neuber method gives the upper limit of stresses and strains. However the results of ESED method are smaller than FEM results, that is, the lower limit can be got by ESED method. It can be found that the results of the two methods locate both sides of FEM results, and the results calculated by modified model are validated with the FEM results. As a consequent, the correction model can be applied to calculate the stresses and strains in the case of multiaxial loading.

7. Conclusion

It is easily obtained that the results calculated by the above three methods are the same in the case of elastic range; However both Neuber method and ESED method usually have large errors under proportional loading. In this paper, a new modified model is proposed on the basis of the analysis of difference between the two methods. The comparisons of the calculated results with FEM results show that the modified model can relatively accurately calculate the stresses and strains of notch tip and it is convenient for engineering application.

References:

[1] Conle F A, Chu C C. Fatigue analysis and the local stress–strain approach in complex vehicular structures. International journal of fatigue, 1997, 19(93): 317-323.

[2] Savaidis, Savaidis G, Zhang Ch. Elastic-plastic FE Analysis of a Notched Shaft under Multiaxial Nonproportional Synchronous Cyclic Loading. Theoretical and Applied Fracture Mechanics, 2001, 36(2): 87-97.

[3] Hoffmann M, Seeger T. A Generalized Method for Estimating Multiaxial Elastic-Plastic Notch Stresses and Strains. Part 1: Theory. Journal of Engineering Materials and Technology, 1985, 107(3): 250-254.

[4] Moftakhar A, Buczynski A, Glinka G. Calculation of elastic-plastic strains and stresses in notches under multiaxial loading. International journal of fracture, 1994, 70(4): 357-373.

[5] Tipton S M. Cyclic Elastic-Plastic Strain Estimation for Notched Shafts in Bending. ICBMFF3, 2013.

[6] Hoffman M, Amstutz H, Seeger T. Local strain approaches in nonproportional loading. Fatigue under Biaxial and Multiaxial Loading. ESIS10, Mechanical Engineering Publications, London, 1991, 34 (3): 357-376.

[7] Ince A, Glinka G. A numerical method for elastic-plastic notch-tip stress-strain analysis. The Journal of Strain Analysis for Engineering Design, 2013, 48(4): 229-244.

[8] Barkey M E, Socie D F, Hsia K J. A yield surface approach to the estimation of notch strains for proportional and nonproportional cyclic loading. Journal of engineering materials and technology, 1994, 116(2): 173-180.

[9] Nisitani H, Kawano K. Non-propagating crack and crack strength of shafts with a shoulder fillet subjected to rotary bending. Eleventh Japan Congress on Materials Research-Metallic Materials, 1968, 39 (4): 49-51.

[10] Neuber H. Theory of stress concentration for shear-strained prismatic bodies with arbitrary nonlinear stress-strain law. Journal of Applied Mechanics (Transactions of the ASME), 1961, 28: 544-9.

[11] Seeger T, Heuler P. Generalized application of Neuber's rule. Journal of Testing and Evaluation 1980; 8: 199-204.

[12] Lee Y L, Chiang Y J, Wong H H. A Constitutive Model for Estimating Multiaxial Notch Strains. Journal of Engineering Materials and Technology, 1995, 117(1): 33-40.

[13] Topper T, Wetzel, Morrow J. Neuber method Applied to Fatigue of Notched Specimens. Journal of Materials, 1969, 4(1): 200-209.

[14] Mücke R, Bernhardi O E. A constitutive model for anisotropic materials based on Neuber's rule. Computer methods in applied mechanics and engineering, 2003, 192(37): 4237-4255.

[15] Molski K, Glinka G. A method of elastic–plastic stress and strain calculation at a notch-tip. Material Science and Engineering1981, 50: 93-100.

[16] Glinka G. Energy density approach to calculation of inelastic strain–stress near notches and cracks. Engineering Fracture Mechanics 1985, 22: 485-508.

[17] Glinka G. Calculation of inelastic notch-tip strain–stress histories under cyclic loading. Engineering Fracture Mechanics, 1985, 22: 839-54.

[18] Ye D, Matsuoka S, Suzuki N, et al. Further investigation of Neuber method and the equivalent strain energy density (ESED) method. International journal of fatigue, 2004, 26(5): 447-455.

[19] Knop M, Jones R, Molent L, et al. On the Glinka and Neuber methods for calculating notch tip strains under cyclic load spectra. International Journal of Fatigue, 2000, 22(9): 743-755.

JJMIE

Volume 8 Number 1, February. 2014
ISSN 1995-6665
Pages 27 - 34

Jordan Journal of Mechanical and Industrial Engineering

Stress Intensity Factors for Crack Located at an Arbitrary Position in Rotating FGM Disks

Hadi Eskandari*

Abadan Institute of Technology, Petroleum University of Technology, Abadan, Iran

Abstract

This article focuses on the stress analysis of an internal crack located at an arbitrary position in a rotating functionally graded material disk. The disk is assumed to be isotropic with exponentially varying elastic modulus in the radial direction.
A comprehensive study is carried out for various combinations of the crack length, direction, and location with the different gradation of materials. The results show that the material gradation, the crack position and the crack length have a significant influence on the value of stress intensity factors. Numerical results are given to assess the safety of the FGM and homogeneous cracked disks.

Keywords*: Functionally Graded Materials; Rotating Discs; Stress Intensity Factor; Stress Analysis; Crack Parameters.*

1. Introduction

To meet the demands of new technologies, functionally graded materials (FGMs) are designed as systems that combine multiple and often significantly different materials into a single system.

FGMs are multiphase materials in which the volume fractions of the constituents vary continuously as a function of position. Therefore, the mismatch of thermo mechanical properties near the bond line is minimized. Another application area of FGMs includes their use as interfacial zone between two different layers; they are also used to improve the bonding strength [1], and to reduce the residual stresses, interfacial delamination [2] and stress concentration or stress intensity factors (SIFs)[3,4]. Because of their outstanding advantages over conventional composites and monolithic materials, these materials have received a wide attention of engineers and researchers from different fields of interest. Kim and Paulino [5] have addressed a wide variety of FGMs applications. The research in FGM development requires the supports of engineering mechanics, especially in the field of fracture mechanics. Recently a wide variety of researches are focused on a nalysis of cracked FGM structures. For example, Nami and Eskandari [6,7] considered cracked FGM cylinders and solved them in different conditions of loading.

Rotating discs are very common and useful parts of several engineering high speed rotating equipment such as compressors, cutters and grinding tools that are used extensively in the process industry today. Parallel to new industrial developments, it s eems that the use of conventional materials in rotating discs is inadequate.

With the trend toward the analyses of cracked structural parts under centrifugal loading, much attention is being paid to investigate the strength and life of a rotating cracked disc. Unfortunately, the most studies are focused to homogeneous discs. For example, Tweed and Rooke [8] considered the homogeneous rotating disc with an edge crack, and Isida [9] considered it for a crack in an arbitrary position. The problem of three dimensional investigation of stress intensity factor in a cracked rotating impeller is considered by Nami and Eskandari [10]. A rigorous elastodynamic hybrid displacement finite element procedure for a s afety analysis of fast rotating discs with mixed mode cracks is considered by Chen and Lin [11]. Cho and Park [12] have investigated the thermoelastic characteristics of functionally graded lathe cutting tools. Zenkour [13] considered a rotating FGM sandwich solid disk with material gradient in the thickness direction for the analysis of stress and displacement.

The problem of finite element analysis of thermoelastic field in a thin circular FGM disk with an exponential variation of material properties in radial direction is considered by Afsar and Go [14]. Sharma et al. [15] studied the thermoelastic displacements, stresses, and strains in a thin, circular, FGM disk subjected to thermal load by taking into account an inertia force due to rotation of the disk. Zafarmand and Hassani [16] obtained the elasticity solution of two-dimensional FGM rotating annular and solid disks with variable thickness.

In the present paper, an internal crack at an arbitrary location of a thin hollow circular FGM disk is considered (Fig. 1). A comprehensive study is carried out for various combinations of the crack length (2a), direction, and location with the different gradation of materials. Here the eccentricity of the midpoint of the crack line is measured

* Corresponding author. e-mail: eskandari@put.ac.ir.

  - Volume 8, Number 1 (ISSN 1995-6665)

as e and the orientation of the crack line relative to x-direction is shown as β.

2. Finite Element Formulation

Consider a rotating FGM disk with a concentric circular hole containing an internal crack at an arbitrary position as shown in Fig. 1. The FGM disk is considered to be made of two distinct material phases, which are, respectively, represented by the dark and white colors as shown in the figure. The distribution of each material continuously varies along the radial direction. The radii of the hole and outer surface of the disk are designated by R_{in} and R_{out}, respectively. Further, the angular velocity of the disk is denoted by ω.

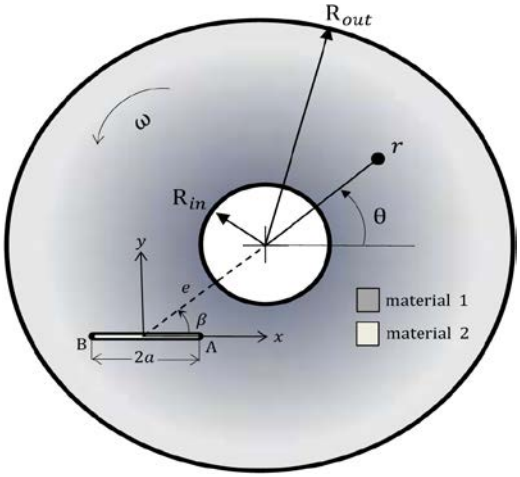

Figure 1. Rotating FGM disk containing an internal crack

A finite element code can be used to account for spatial variation in material property of FGM disk. There are different ways of incorporating changes in material properties into a finite element program. Walter *et al.* [17] describe two commonly-used methods. An element base method where the desired spatial material property of each element based on its location is achieved through a finite element code. Another way is to compute the material property at each integration point for element stiffness matrix via the spatial varying in material property function.

In this study, a finite element code is used to account for the material property changes in each element via its location. This section describes the details of the finite element formulation for stress and fracture analyses of FGM disk. The material is assumed to be isotropic with exponentially varying elastic modulus in radial direction as follows:

$$E(r) = E_{in}\, e^{\psi (r - R_{in})} \tag{1}$$

Where R_{in} is the inner radius of the disk and ψ is the constants of material which defined as

$$\psi = \frac{1}{R_{in} - R_{out}} \ln\left(\frac{E_{in}}{E_{out}}\right) \tag{2}$$

Which R_{in} and R_{out} denote the inner and outer radius of the disk, E_{in} and E_{out} are the values of elastic modulus at the inner and outer radius of the disk, respectively. For a simple traceable solution, the dependency to the Poisson's ratio is neglected and it is assumed constant ($\nu = 0.3$) throughout the disk.

The stress intensity factor for the disk is considered in the non-dimensional form and is defined as:

In which $K_{I,A}$ and $K_{I,B}$ are the calculated values of the first mode stress intensity factors in right and left sides of the crack, respectively. $K_{II,A}$ and $K_{II,B}$ are the calculated values of the second mode stress intensity factors in right and left sides of the crack, respectively.

The nominal stress intensity factor, K_0, for FGM disk is used as:

$$K_0 = \sigma_0 \sqrt{\pi\, a} \tag{4}$$

Where σ_0 is considered as:

$$\sigma_0 = \frac{3 + \upsilon}{8}\, \rho\, V^2 \tag{5}$$

a is the crack length, ρ and V being the material density and the peripheral speed, respectively.

The eccentricity of the crack center is defined as:

$$\varepsilon = \frac{e}{R_{out}} \tag{6}$$

and the dimensionless crack length is defined as:

$$\lambda = \frac{a}{R_{out} - e} \tag{7}$$

The FGM disk, considered in the present study, is assumed to be fixed to a shaft. The outer surface of the disk is free from any mechanical load. Thus, the boundary condition of the problem can be given by:

$$\begin{aligned} &\text{(i)} \quad r = R_{in}, \quad u_r = 0. \\ &\text{(i)} \quad r = R_{out}, \quad \sigma_r = 0. \end{aligned} \tag{8}$$

3. Crack Tip Fields in FGMs

Material non-homogeneity has a significant influence on SIFs, which, in turn, will influence subsequent crack trajectory [18]. Williams [19] proposed the Eigen function expansion technique to investigate the nature of the near-tip fields in a two-dimensional crack body. An extension of this conventional procedure has been used by Eischen [20] to establish the general form of the stress and displacement fields near a crack tip in a nonhomogeneous material with a spatially varying material property. Eischen solved the problem for materials with continuous, bounded, and differentiable property variations. He showed that the asymptotic fields for a crack in an FGM with continuous mechanical properties are similar to those of a crack embedded in a homogeneous material. In addition, the asymptotic displacement expressions for the homogeneous materials can be used for FGMs on condition that the material properties are calculated at the crack-front location. Jin and Noda [21] further showed that this result is also valid for materials with piecewise differentiable property variation.

A crack in a continuously non-homogeneous, isotropic and linear elastic FGM body with applied boundary conditions on the body satisfies the equilibrium equation:

$$\sigma_{ij,j} + F_i = 0 \tag{9}$$

and the Hooke's law is as (10):

$$\sigma_{ij} = C_{ijkl}(X)\varepsilon_{kl} \tag{10}$$

Where σ_{ij} is the stress tensor, F_i is the body force tensor, $C_{ijkl}(X)$ is the constitutive relation of FGMs and ε_{kl} is the strain tensor. The comma after a quantity denotes the partial derivatives with respect to spatial variable.

As mentioned previously, for a s imple traceable solution, the functional dependence to the Poisson's ratio is neglected and it is assumed constant throughout the analysis, thus Eq. (10) can be expressed as [19]:

$$\sigma_{ij} = \frac{E(X)}{2(1+\nu)} C^H_{ijkl}\,\varepsilon_{kl} = \frac{E(x)}{2(1+\nu)} C^H_{ijkl}\,u_{k,l} \tag{11}$$

Where u_i is displacement component and C^H_{ijkl} is the constitutive relation of corresponding homogeneous material and can be written as [22]:

$$C^H_{ijkl} = \frac{2\nu}{1-2\nu}\,\delta_{ij}\,\delta_{kl} + \delta_{ki}\,\delta_{lj} + \delta_{kj}\,\delta_{li} \tag{12}$$

here δ_{ij} denotes the Kronecker delta tensor.

Since the nature of the stress singularity for continuously non-homogenous, isotropic and linear elastic solid is precisely the same as the well-known form applicable to homogeneous materials, irrespective of the particular form of the Young's modulus variation (Eischen,1987), the stress intensity factors can be obtained from crack-opening-displacements (CODs) as [22]:

$$\begin{Bmatrix} K_I \\ K_{II} \\ K_{III} \end{Bmatrix} = \frac{\mu_{tip}\sqrt{2\pi}}{4(1-\nu)} \lim_{\delta\to 0} \frac{1}{\sqrt{\delta}} \begin{Bmatrix} \Delta u_\zeta(\delta) \\ \Delta u_\xi(\delta) \\ (1-\nu)\Delta u_\eta(\delta) \end{Bmatrix} \tag{13}$$

where K_I, K_{II} and K_{III} are opening, sliding and tearing modes of SIFs, μ_{tip} is the shear modulus at the crack front, δ which approaches zero is a small distance between specified node at crack-surface and a n ode at crack-front, and

$$\Delta u_l(X) = [u_l(X \in \text{upper crack surface}) - u_l(X \in \text{lower crack surface})]$$

in which $l = \zeta, \xi$ and η are the CODs in the local coordinate systems.

4. The Validation of the Method

4.1.1. Stresses in a Functionally Graded Strip

To justify the reliability of the FGM model, the semi-infinite functionally graded strip under the uniform tensile load (in the y-direction) has been considered in Fig. (2-a). Young's modulus is an exponential function of *z*, i.e. $E(z) = E_1\, e^{\ln(\frac{E_2}{E_1})\frac{z}{W}}$, while Poisson's ratio is constant.

Figure (2-b) shows the normalized σ_{yy} stresses for different levels of material gradation. These results agree well with those of Erdogan and Wu [23]. Thus, such excellent results validate the present FEM implementation for elastic FGMs.

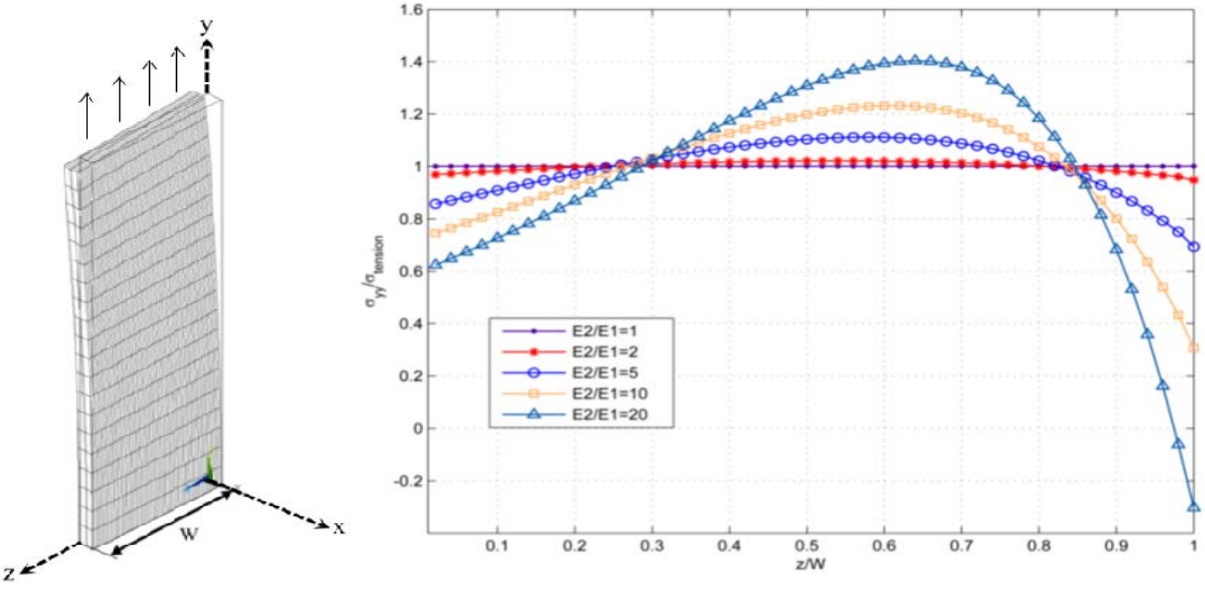

(a) (b)

Figure 2. (a) Finite-element model of uncracked functionally graded strip, (b) normalized σ_{yy} stresses for different levels of material gradation – uniform tensile far-field stress

4.1.2. Edge Crack in a Plate

Figure 3 shows an edge crack of length *a* located in a finite two-dimensional functionally graded strip under tension loading. As in the case of stress analysis of uncracked strip, the same form of material property gradation is considered. Table 1 compares the normalized SIFs of the current study with those reported by Chen *et al.* [21]. As can be seen in this table, the maximum difference is less than 2.25% when a/w=0.3 and $E_2/E=10$. Thus, good agreement is obtained between the different solutions for both homogeneous and FGM cases.

Table 1. Normalized stress intensity factors for an edge cracked FGM plate under tension.

Method	E_2/E_1	a/W				
		0.2	0.3	0.4	0.5	0.6
Chen *et al.*[24]	0.2	1.455	1.897	2.529	3.443	4.926
	1	1.408	1.698	2.178	2.933	4.237
	5	1.158	1.392	1.794	2.446	3.611
	10	1.032	1.249	1.614	2.223	3.337
Current study	0.2	1.455	1.915	2.539	3.442	4.880
	1	1.428	1.733	2.205	2.951	4.216
	5	1.182	1.430	1.826	2.472	3.603
	10	1.046	1.282	1.658	2.273	3.357

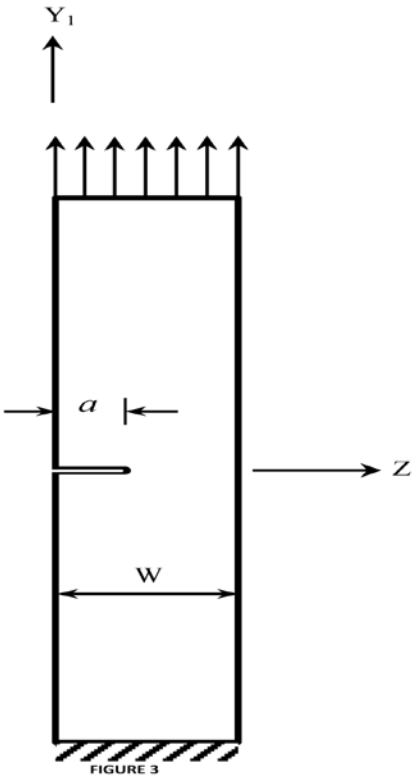

Figure 3. A functionally graded semi-infinite strip containing an edge crack

4.1.3. Arbitrary Crack in a Rotating Solid Disk

Consider the homogeneous elastic rotating disk in figure 1 with no hole. The stress intensity factors for the right hand side of the crack at different positions of the solid disk are determined and compared with those reported by Isida [9]. The problem was solved by two different methods, i.e. the Displacement Correlation Technique (DCT) and the J-integral method. The results are shown in figures 4. As it can be seen from figure 4, the results agree well with those reported in literature by Isida [9].

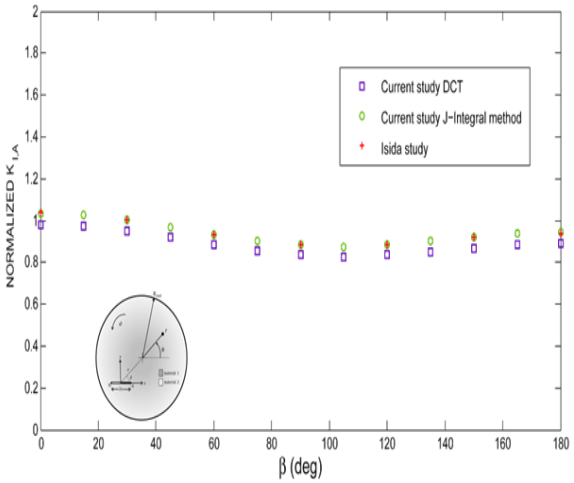

Figure 4. . Variation of the normalized $K_{I,A}$ with β for $\lambda = \varepsilon = 0.5$

5. Results and Discussion

In this study, the stress intensity factors for two sides of an internal crack located at an arbitrary position of a rotating FGM disk with a concentric circular hole is determined. When the gradation of material is assumed radially, i.e. Eq. (1), it is obvious that $K_{I,A}(\beta) = K_{I,B}(180-\beta)$ for $90 \le \beta \le 180$. Therefore, the problem for both $K_{I,A}$ and $K_{I,B}$ in the range of $0 \le \beta \le 90$ is solved and the results are plotted only for SIF in the right hand side of the crack. Figure 5 shows the variation of normalized $K_{I,A}$ with dimensionless crack lengths, λ, for different gradation of materials, i.e. $\frac{E_{in}}{E_{out}} = 0.2, 1, 5 \text{ and } 20,$ when $\beta = 0, 30, 90, 120, 150 \text{ and } 180.$

From Fig. 5, it is evident that for a certain value of λ, in the range of $0 \le \beta \le 120$, higher the gradation of materials, i.e. $\frac{E_{in}}{E_{out}}$, higher the $K_{I,A}$. An exception is seen only for radial cracks with $\lambda = 0.1$ and $\frac{E_{in}}{E_{out}} = 20$.

Variation of the normalized stress intensity factor for right hand side of the crack, i.e. $K_{I,A}$, with β is plotted at figure 6a through 6d. Each curve is plotted for a certain value of material gradation and different values of dimensionless crack length, *i.e.*, λ =0.1 to 0.5. As seen, for homogeneous materials, the larger the crack lengths

(larger $\lambda's$), the higher the values of $K_{I,A}$. This result is valid for FGM disks with $\frac{E_{in}}{E_{out}} > 1$ and $\beta \leq 120$, but the trend is apt to be reversed for higher values of $\beta's$. In other words, for FGM disks with $\frac{E_{in}}{E_{out}} < 1$ and $\beta \leq 40$, the smaller the crack lengths (larger $\lambda's$), the higher the values of $K_{I,A}$ and this rule tends to be reversed for higher values of $\beta's$. This fact can be seen in figure 5, too.

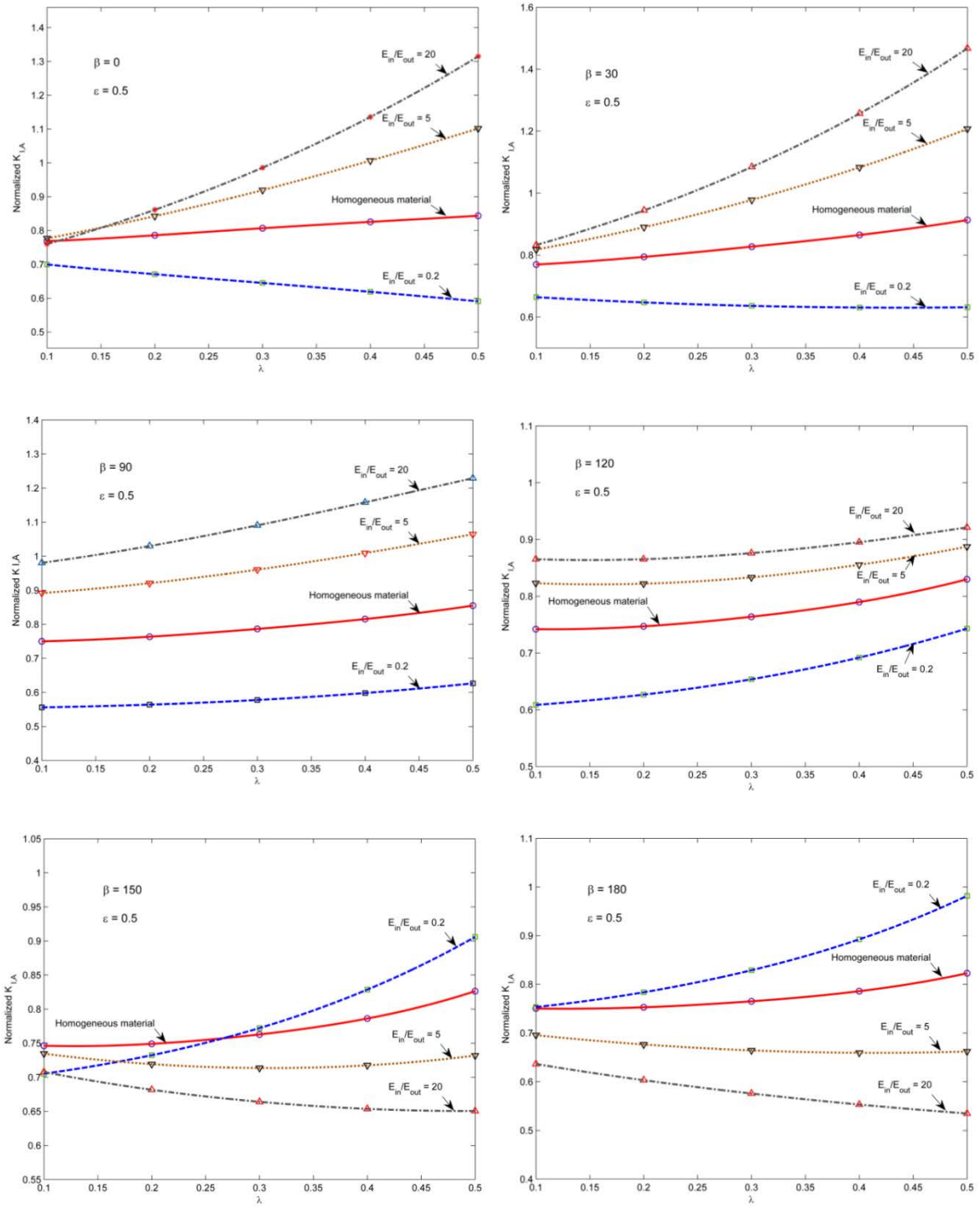

Figure 5

Figure 5. Variation of normalized $K_{I,A}$ with λ for different gradation of materials, i.e. $\frac{E_{in}}{E_{out}} = 0.2, 1, 5$ and 20, when $\beta = 0, 30, 90, 120, 150$ and 180.

Another interesting point for homogenous and FGM disks with $\frac{E_{in}}{E_{out}} > 1$, is that $K_{I,A}$ for the crack tip which closer to the disk center is generally larger than $K_{I,B}$. In other words, for FGM disks with $\frac{E_{in}}{E_{out}} < 1$, $K_{I,A}$ is smaller than $K_{I,B}$. In addition, it can be concluded from Figs. 6c-6d that as $\frac{E_{in}}{E_{out}}$ increased, there exists a value of β in which the $K_{I,A}$ is independent to the crack length. Here $\beta_1 \approx 132^o$. This position for FGM disks with $\frac{E_{in}}{E_{out}} < 1$ occurs at $\beta_2 \approx 180^o - 132^o = 48^o$. It seems that these values are supplement.

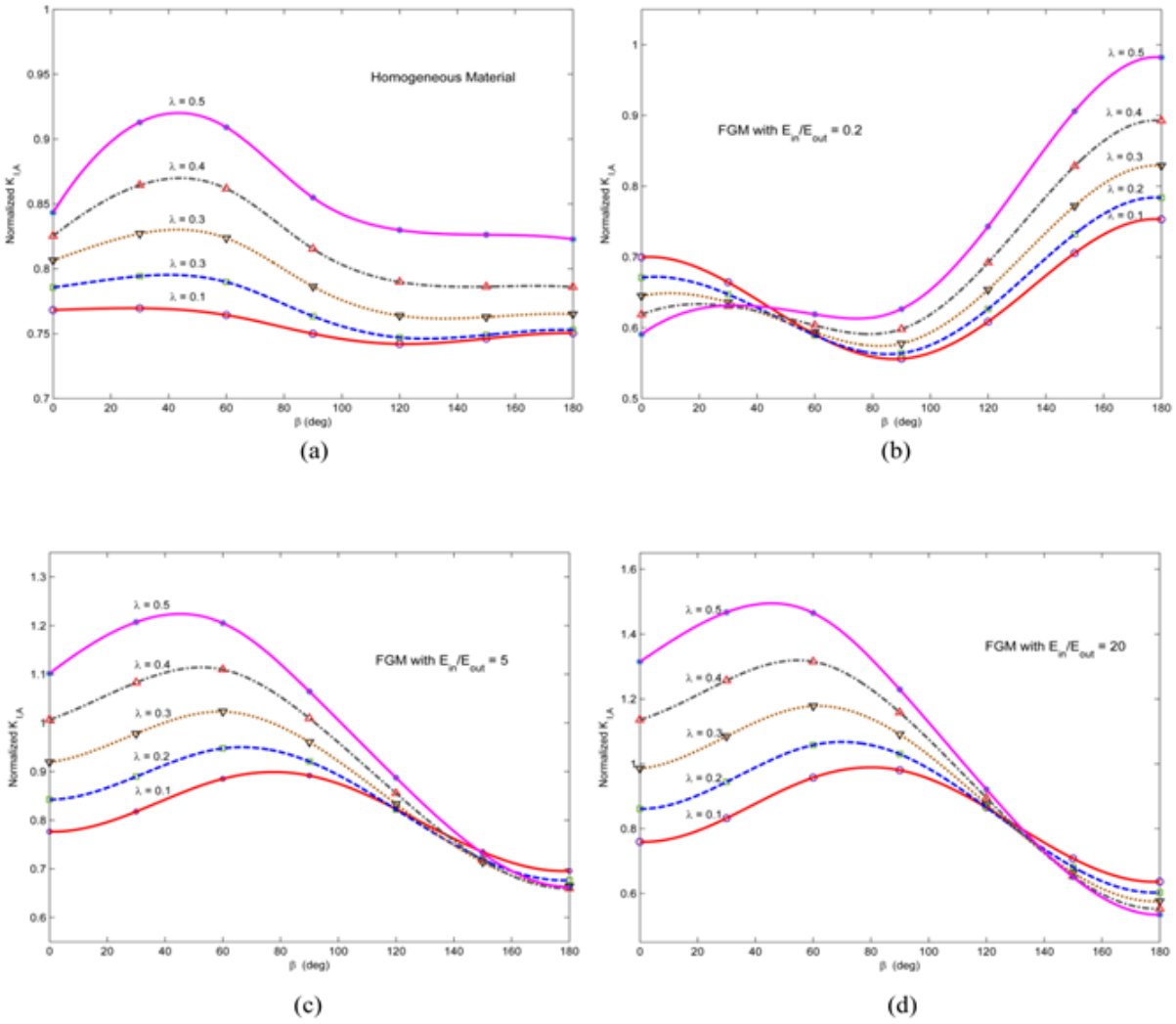

Figure 6. Variation of normalized $K_{I,A}$ with β for different crack lengths, λ, and different gradation of materials, (a) homogenous material, (b) FGM with $\frac{E_{in}}{E_{out}}$ = 2, (c) FGM with $\frac{E_{in}}{E_{out}}$ =5 , (d) FGM with $\frac{E_{in}}{E_{out}}$ =20

The values of $K_{I,A}$ in homogeneous and functionally graded discs for small and large cracks are plotted at Figs. 7a and 7b. It can be seen from Figures 7a – 7b that for cracks in functionally graded discs with $\frac{E_{in}}{E_{out}} > 1$, maximum $K_{I,A}$ occurs at $0 < \beta < 180$, where the cracks are not in radial direction. Also, the minimum value of SIF occurs at left hand side of the crack in the position of $\beta = 0$ (radial crack).

In addition, it can be concluded from Fig. 6a that small cracks in FGM disks with $\frac{E_{in}}{E_{out}} < 1$, have minimum value of SIFs at $0 < \beta < 180$ and maximum values occur in radial cracks. For a wide variety of crack positions in the range of $0 \leq \beta \leq 90$, large cracks in functionally graded discs with $\frac{E_{in}}{E_{out}} < 1$, experience constant value of SIFs.

So far, the stress intensity factors K_I for the opening mode deformation have been discussed. On the other hand, the shear mode stress intensity factor K_{II} are found to be rather small compared with K_I of the corresponding crack tips. This fact may be attributed to the biaxial tension state of the untracked disk. Table 2 gives $K_{II,B}$ values for the typical case when $\beta = 60$, and they are shown to be fairly small compared with the corresponding $K_{I,B}$ values

given in figure 5. Therefore, the shear mode deformation can be neglected in the fracture analysis of a rotating disk.

Table 2. Values of $K_{II,B}$ for $\beta = 60$ and $\varepsilon = 0.5$

	λ				
E_{in}/E_{out}	0.1	0.2	0.3	0.4	0.5
0.2	0.0720	0.0728	0.0786	0.0903	0.1085
1	0.0092	0.0159	0.0255	0.0390	0.0571
5	0.0474	0.0311	0.0140	0.0050	0.0267
20	0.0847	0.0587	0.0337	0.0084	0.0185

Variation of normalized $K_{I,A}$ with ε for different gradation of materials in cracks with constant length at $\beta = 45^o$ is shown in figure 8. As seen, for cracks with $\varepsilon < 0.7$, higher the material gradation, higher the values of $K_{I,A}$. In other words, for cracks near the outer radius of the disk with $\varepsilon > 0.7$, the values of $K_{I,A}$ decrease with increasing the gradation of material. Here the value of $\varepsilon \approx 0.7$ can be considered as an important point in fracture analysis of rotating disks.

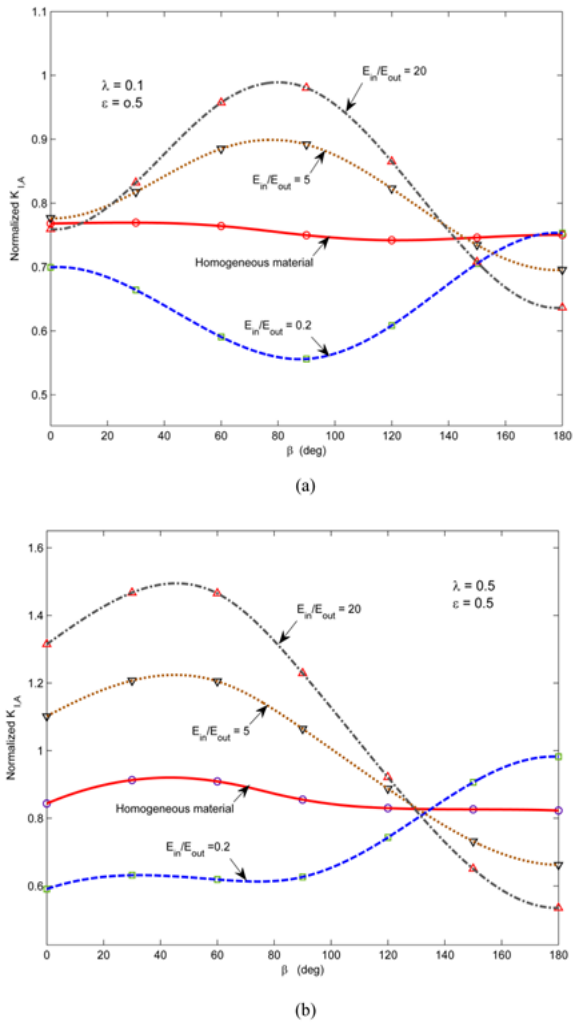

Figure 7. Comparison of $K_{I,A}$ in homogeneous and functionally graded materials for, (a) relatively small cracks ($\lambda = 0.1$), (b) relatively large cracks ($\lambda = 0.5$).

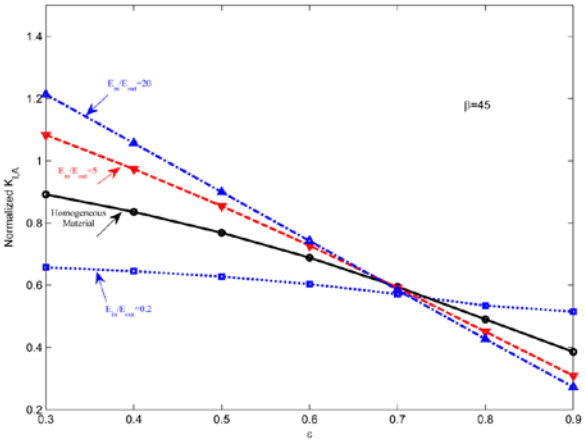

Figure 8. Variation of normalized $K_{I,A}$ with ε for different gradation of materials, i.e. $\frac{E_{in}}{E_{out}} = 0.2, 1, 5$ and 20, in cracks with constant length at $\beta = 45$

6. Summary and Conclusions

In this study, the stress analysis of an internal crack located at an arbitrary position in a thin hallow rotating FGM disk is carried out. The disk is assumed to be isotropic with exponentially varying elastic modulus in the radial direction. A comprehensive study is carried out for various combinations of the crack length, direction, and location with the different gradation of materials. The results which are normalized for the advantage of non-dimensional analysis show that the material gradation, the crack position and the crack length have a s ignificant influence on t he amount of stress intensity factors. The critical values of stress intensity factors and their position in homogeneous and FGM disks are obtained. The larger the cracks, the larger the stress intensity factors in homogeneous disks. In general, this is not valid in FGM disks. Nu merical results are given to assess the safety of the FGM and homogeneous cracked disks.

Acknowledgment

The author gratefully acknowledge the supports of Abadan Institute of Technology, Petroleum University of Technology, Abadan, Iran.

References

[1] K. Kurihara, K. Sasaki, and M. Kawarada, “Adhesion improvement of diamond films”. In: M. Yamanouochi, M. Koizumi, T. Hirai, and I. Shiota (eds.), Proceedings of the First International Symposium on Functionally Gradient Materials, 1995 , 65-69.

[2] Y.-D. Lee, F. Erdogan, “Residual/thermal stresses in FGM and laminated thermal barrier coatings”. Int. J. Fract., Vol. 69, No. 2, 1995, 145–165.

[3] F. Erdogan, “Fracture mechanics of functionally graded materials”. Compos. Eng., Vol. 5, No. 7, 1995, 753–770.

[4] J.-H. Kim, G.H. Paulino, "Isoparametric graded finite elements for nonhomogeneous isotropic and orthotropic materials". J. Appl. Mech., Vol. 69, No.4, 2002a, 502–514.

[5] J.-H. Kim, G.H. Paulino, "Finite element evaluation of mixed mode stress intensity factors in functionally graded materials". Int. J. Numer. Method Eng., Vol. 53, 2002b, 1903-1935.

[6] M. R. Nami, H.Eskandari, "Three-Dimensional Investigations of Stress-Intensity Factors in a Cracked Cylinder Made of Functionally Graded Materials". Mech. Based Des. Struc. Int. J., Vol. 40, No. 2, 2012, 206-217.

[7] M. R. Nami , H . Eskandari, "Three-dimensional investigations of stress intensity factors in a thermo-mechanically loaded cracked FGM hollow cylinder". Int. J. Pres. Ves. Pip.,Vol. 89, 2012, 222-229.

[8] D. P. Rooke, J. Tweed, "The stress intensity factor of an edge crack in a finite rotating elastic disc". Int. J. Eng. Science, Vol. 11, 1973, 279-283.

[9] M. Isida, "Rotating disk containing an internal crack located at an arbitrary position". J. Eng. Fract. Mech., Vol. 14, 1981, 549-555.

[10] M. R. Nami , H . Eskandari, " Stress intensity facors in a rotating impeller containing semi-elliptical surface crack". Mech. Based Des. Struc. Int. J., Vol. 40, 2012, 1-18.

[11] W. H. Chen, T. C. Lin, "A mixed-mode crack analysis of rotating disk using finite element method". J. Eng. Struct, Vol. 18, No. 1, 1983, 133-143.

[12] J. R. Cho, H. J. Park, "High strength FGM cutting tools: finite element analysis on thermoelastic characteristics". J. Mater. Process Technol., Vol. 130-131, 2002, 351-356.

[13] A.M. Zenkour, "Stress distribution in rotating composite structures of functionally graded solid disks". J. Mater. Process Technol., Vol. 209, 2009, 3511–3517.

[14] A. M. Afsar, J. Go, "Finite element analysis of thermoelastic field in a rotating FGM circular disk". Appl. Math. Modeling, Vol. 34, 2010, 3309-3320.

[15] J. N. Sharma, D. Sharma, S. Kumar , "Vibration analysis of a rotating FGM thermoelastic axisymmetric circular disk using FEM". Int. J. Comp. Methods Eng. Science Mech., Vol. 14, No. 3, 2013, 262-270.

[16] H. Zafarmand, B. Hassani, "Analysis of two dimensional functionally graded rotating thick disks with variable thickness". Acta Mech., Vol. 225, 2014, 453-464.

[17] M.C. Walters, G.H. Paulino, R. H. Dodds, "Stress-intensity factors for surface cracks in functionally graded materials under mode-I thermomechanical loading". Int. J. Solids Struct., Vol. 41, 2004, 1081-1118.

[18] J.-H. Kim, "Mixed-mode crack propagation in functionally graded materials". Ph.D. thesis, University of Illinoisat Urbana-Champaign, Illinois, 2003.

[19] M.L. Williams, "on the stress distribution at the base of a stationary crack". J. Appl. Mech., Vol. 24, 1957, 109 -114,

[20] J.W. Eischen, "Fracture of non-homogeneous materials". Int. J. Fract., Vol. 34, 1987, 3-22.

[21] Z.H. Jin, N. Noda, "Crack tip singular fields in non-homogeneous materials". J. Appl. Mech., Vol. 6 1, No. 3, 1994, 738 -740.

[22] C. Zhang, M. Cui, J. Wang, X.W. Gao, J. Sladek, V. Sladek, "3D crack analysis in functionally graded materials". Eng. Fract. Mech., Vol. 78, No. 3, 2011, 585-604.

[23] F. Erdogan, B. H. Wu, "The surface crack problem for a plate with functionally graded properties". J. Appl. Mech., Vol. 64, 1997, 449-456.

[24] J. Chen, L. Wu, S. Du, "A modified J integral for functionally graded materials". Mech. Res. Commun., Vol. 27, No. 3, 2000, 301-306.

JJMIE

Volume 8 Number 1, February. 2014
ISSN 1995-6665
Pages 35 - 42

Jordan Journal of Mechanical and Industrial Engineering

Comparison between Taguchi Method and Response Surface Methodology (RSM) in Modelling CO_2 Laser Machining

Sivaraos[a,*] , K.R.Milkey[a], A.R.Samsudin[a], A.K.Dubey[b], P.Kidd[c]

[a]*Faculty of Manufacturing Engineering, Universiti Teknikal Malaysia Melaka, 75450 Ayer Keroh, Melaka, Malaysia.*

[b]*Department of Mechanical Engineering, Motilal Nehru National Institute of Technology, Allahabad 211004, U.P., India.*

[c]*UES International Pte. Ltd., No 1 Jalan T.U.43, Taman Tasik Utama, 75450 Ayer Keroh, Melaka, Malaysia.*

Abstract

The applications of Taguchi method and RSM to modelling the laser parameters when machining industrial PVC foams is presented. The influence of cutting speed, laser power, frequency, duty cycle, and gas pressure on kerf width has been considered in this investigation according to Taguchi method using a standard orthogonal array L_{27} and RSM using a central composite design. Taguchi technique as well as 3D surface plot of RSM revealed that the cutting speed is the most significant factor in minimizing kerf width followed by laser power and etc. A predictive mathematical model was then developed through a regression analysis in both analytical tools to study the response. Though both the techniques predicted near values of average error, the RSM technique seems to be more promising in predicting the response via mathematical modelling over the Taguchi technique.

Keywords: *Laser Cutting; Kerf Width; DOE Method; PVC Foam; Mathematical Model.*

1. Introduction

Industrial PVC foams are widely used as a core material in composite/sandwich for marine applications as they own low density with high moisture resistance values. PVC foams are closed-cell and have good physical properties as compared to other foams of similar density. On the other hand, laser advancements stand advantage to cut thermoset material with high level of precision and flexibility. Laser machining is one of the non-contact advanced processing techniques with narrow kerf in almost all categories of materials such as metals, non-metals, ceramics and composites [1]. In polymer, it is complicated to identify the best parameters for machining the materials due to their poor thermal and physical properties compared to metals or ceramic [2].

The main challenge in laser cutting of materials is to select the most appropriate parameters. Laser power, cutting speed, frequency, duty cycle and gas pressure are the most important parameters for laser cutting depending on materials being cut. Effective parameters should be controlled to obtain a high quality of laser cutting. Determination of the parameters by classical experimental design methods requires a large amount of experimental data, which has been found costly and time consuming [3,4]. To overcome the difficulties, researchers applied DOE methods such as factorial design, Taguchi method and response surface methodology are now widely used in place of OFAT experimental approach. The response surface methodology approach was successfully used to investigate the laser cutting performance of medium density fibreboard [5]. In another investigation, the effect of assist gas pressure on quality of the cut CFRP material, namely pure oxygen, pure nitrogen and 50% oxygen - 50% nitrogen, central composite design (CCD) of RSM was successfully applied as an analytical tool [6]. RSM was also derived ironically to identify the effect of five factors on cut quality, namely kerf width, dross height and slope of the cut [7].

Combining of RSM and Taguchi technique was used to developed mathematical model on surface roughness and power consumption [8]. The Taguchi method was used to find the optimal cutting parameters for laser machining [9]. An integrated approach whereby the combination of ANN technique and Taguchi's algorithm was also used in optimizing the CO_2 laser welding process to obtain the optimal setting [10]. An integrated investigation using Taguchi and principle component analysis in gaining best of kerf width, kerf deviation and kerf taper, where, pulse width and cutting speed was found very much influential to response [11]. Researchers also investigated a selection of cutting parameters towards cut quality on carbon fibre reinforced plastics (CFRP) composite and later optimized up to the desired response with RSM [12]. In a laser drilling investigation, machining parameters on recast layer and micro-crack formation were performed by means of Taguchi method [13]. Taguchi methodology was also

* Corresponding author. e-mail: sivarao@utem.edu.my.

successfully applied for parameter optimization during micro-engraving of photo-masks. Five factors, each at two levels, were selected and the experiment was designed using L_{16} orthogonal array [14].

2. Experimental Details

The Helius Hybrid 2514 CO_2 laser beam cutting machine was used to conduct this experimental research. The investigated research work was conducted using H80 industrial PVC foam as work materials with the density of 80 kg/m^3 and 20 m m thickness, supplied by marine composites industry, UES International Pte. Ltd. The kerf width 'responses' that were obtained after the experimental runs were observed by optical comparator with embedded digital micrometer with an accuracy of 1 micron, which allows easy access to measure both X-axis and Y-axis directions. The estimated values of kerf width are based on Equation 1:

$$\text{Kerf Width (mm)} = \frac{\text{Upper Kerf Width} + \text{Lower Kerf Width}}{2} \quad (1)$$

Preliminary experiments were critically designed and conducted to identify the design range for each tested process parameters. Thus, from the initial screening results, five parameters were identified significant, namely laser power, cutting speed, frequency, duty cycle, and gas pressure; they were found to be most influencing and correlated to the kerf width. Table 1 summarizes the constant values, whereas Table 2 summarizes the design parameters and their respective levels employed throughout the entire number of experimentations.

Table 1. Parameters setting for constant parameters

S.O.D (mm)	F.D (mm)	Lens (mm)	Nozzle Type	Gas Selection	Material Thickness (mm)
1	0	7.5	Conical	Nitrogen	20

S.O.D: stand-off distance; F.D: Focal Distance

Table 2. Experimental design parameters and levels.

Parameter	Code	Unit	Level 1	Level 2	Level 3
Cutting Speed	A	mm/min	1800	1900	2000
Laser Power	B	W	550	625	700
Frequency	C	Hz	1700	1775	1850
Duty Cycle	D	%	80.0	82.5	85.0
Gas Pressure	E	Bar	1.5	2.0	3.0

3. Analytical Tools

3.1. Taguchi's Experimental Design

The Taguchi method is a unique statistical experimental design approach that greatly improves the engineering productivity [15]. Taguchi suggests the production process to be applied at optimum levels with minimum variation in its functional characteristics. In general, the signal-to-noise (S/N) ratio (η, dB) represents quality characteristics for the observed data in the Taguchi method. S/N ratio is an index to evaluate the quality of manufacturing process. Here, the 'signal' represents the desirable value and the 'noise' represents the undesirable value, where signal to noise ratio expresses the scatter around the desired value. The experimental result should be transformed into the S/N ratios, mainly three types: smaller-the-better, nominal-the-best (Equation 2), and larger-the-better (Equation 3). In this case, lower values of the kerf width is desirable for maintaining high cut quality; hence smaller-the-better S/N ratio was computed based on Equation 4 as shown [16]:

Table 3. Central-composite design (RSM)

Standard	Exp. Run	Factor levels					Response
		A	*B*	*C*	*D*	*E*	Kerf width (mm)
1	26	-1	-1	-1	-1	1	0.264
2	21	1	-1	-1	-1	-1	0.451
3	30	-1	1	-1	-1	-1	0.639
4	15	1	1	-1	-1	1	0.476
5	25	-1	-1	1	-1	-1	0.618
6	12	1	-1	1	-1	1	0.499
7	32	-1	1	1	-1	1	0.644
8	6	1	1	1	-1	-1	0.475
9	29	-1	-1	-1	1	-1	0.457
10	28	1	-1	-1	1	1	0.471
11	24	-1	1	-1	1	1	0.614
12	19	1	1	-1	1	-1	0.822
13	27	-1	-1	1	1	1	0.603
14	10	1	-1	1	1	-1	0.518
15	23	-1	1	1	1	-1	0.778
16	8	1	1	1	1	1	0.528
17	13	-1	0	0	0	0	0.604
18	20	1	0	0	0	0	0.455
19	2	0	-1	0	0	0	0.452
20	5	0	1	0	0	0	0.513
21	11	0	0	-1	0	0	0.546
22	7	0	0	1	0	0	0.557
23	17	0	0	0	-1	0	0.516
24	4	0	0	0	1	0	0.653
25	14	0	0	0	0	-1	0.553
26	31	0	0	0	0	1	0.472
27	3	0	0	0	0	0	0.602
28	22	0	0	0	0	0	0.629
29	9	0	0	0	0	0	0.611
30	1	0	0	0	0	0	0.597
31	18	0	0	0	0	0	0.519
32	16	0	0	0	0	0	0.603

$$S/N = 10\log\left(\frac{\bar{y}}{s_y^2}\right) \quad (2)$$

$$S/N = -10\log\left(\frac{1}{n}\sum_{i=1}^{n}\frac{1}{y^2}\right) \quad (3)$$

$$S/N = -10\log\left(\frac{1}{n}\sum_{i=1}^{n}y_i^2\right) \quad (4)$$

Where, y_i is the observed data at the i^{th} trial, and n is the number of trials of the same level with the aim of always keeping maximize of the S/N ratio. A parameter level corresponding to the maximum average S/N ratio is called optimum level for that parameter [17]. The predicted value of S/N ratio (η_{opt}) at optimum parameter levels is analysed by Equation 5 as follows [18]:

$$\eta_{opt} = \bar{\eta} + \sum_{i=1}^{k}\left(\eta_{mi} - \bar{\eta}\right) \quad (5)$$

Where, $\bar{\eta}$ is the average S/N ratio of all experimental runs, k is the number of control factors, and η_{mi} is the mean S/N ratio for i^{th} control factor corresponding to optimum parameter level. S/N ratio calculated for optimum level as Equation 6:

$$\eta_0 = \eta_m + (\eta A_3 - \eta_m) + (\eta B_1 - \eta_m) + (\eta C_2 - \eta_m) + (\eta D_1 - \eta_m) + (\eta E_1 - \eta_m) \quad (6)$$

η_o is optimum S/N ratio, η_m is the overall mean of S/N values, ηA_3 is the third level of cutting speed, ηB_1 is the first level of laser power, ηC_2 is the second level of frequency, ηD_1 is the first level of duty cycle and ηE_1 is the first level of gas pressure. According to the formula Equation 6, η_o was found as 9.126 dB. Some verification experiments are conducted at suggested optimum parameter levels to validate the predicted responses. The experiments are performed as per standard L_{27} orthogonal array and the analysed S/N ratio (η values) corresponding to each experimental run is given in Table 4.

3.2. RSM Experimental Design

Response surface methodology (RSM) is an analytical method that is commonly used to statistically justify the significance of the relationship between input variables (independent variables) to output variables (response). Statistical branch revolves around deriving information about the properties of random processes from sets of observed samples [19]. It is most helpful to construct a model which provides a mathematical representation of the given situation for most of the statistical based investigation [20]. In some system, the nature of the relationship between y and x values might be known. Then, a model can be written in the form [21]:

$$y = f\left(x_1, x_2, ...x_n\right) + \varepsilon \quad (7)$$

Where ε characterizes noise or error observed in the output y. If we signify the expected output as:

$$E\left(y\right) = \left(x_1, x_2, ...x_n\right) = y \quad (8)$$

So the surface represented by:

$$\hat{y} = f\left(x_1, x_2, ...x_n\right) \quad (9)$$

In RSM, the experiments are performed using CCD matrix (for first-order response model factorial design matrix can be used, but due to lack-of-fit, first-order-response model is avoided generally) to develop a second order response model as:

$$Y = b_o + b_1X_1 + b_2X_2 + ... + b_{11}X_1^2 + b_{22}X_2^2 + b_{12}X_1X_2 + ...b_{n-1,n}X_{n-1}X_n, \quad (10)$$

where, Y is response and X_i are different factors. The regression coefficients b_i can be computed by least-square method. Significance of factors and their interactions can be computed using statistical analysis. Using above response model optimum value of responses and optimal setting of parameters can be computed [22].

Table 4. L_{27} orthogonal array (Taguchi)

Standard	Exp. Run	Factor levels					Responses	
		A	*B*	*C*	*D*	*E*	KW (mm)	η_{KW} (dB)
1	2	1	1	1	1	1	0.430	7.341
2	27	1	1	1	1	2	0.440	7.141
3	12	1	1	1	1	3	0.452	6.897
4	7	1	2	2	2	1	0.487	6.241
5	25	1	2	2	2	2	0.483	6.312
6	22	1	2	2	2	3	0.513	5.791
7	4	1	3	3	3	1	0.587	4.627
8	19	1	3	3	3	2	0.506	5.926
9	20	1	3	3	3	3	0.637	3.924
10	26	2	1	2	3	1	0.395	8.079
11	10	2	1	2	3	2	0.428	7.381
12	14	2	1	2	3	3	0.461	6.726
13	21	2	2	3	1	1	0.381	8.393
14	24	2	2	3	1	2	0.487	6.258
15	1	2	2	3	1	3	0.451	6.926
16	15	2	3	1	2	1	0.456	6.821
17	5	2	3	1	2	2	0.480	6.375
18	9	2	3	1	2	3	0.435	7.240
19	18	3	1	3	2	1	0.352	9.069
20	13	3	1	3	2	2	0.446	7.013
21	17	3	1	3	2	3	0.391	8.168
22	23	3	2	1	3	1	0.430	7.331
23	16	3	2	1	3	2	0.492	6.161
24	6	3	2	1	3	3	0.461	6.726
25	8	3	3	2	1	1	0.423	7.473
26	11	3	3	2	1	2	0.434	7.250
27	3	3	3	2	1	3	0.391	8.168

The observed data from the experimental runs were then fed into a commercially available analytical tool to analyse, optimize and establish a predictive mathematical model to estimate the kerf width. In this case, a half fractional factorial, with 5 factors, 10 axial points at the face, and 6 centre point, were used which gives a total of 32 design point. The design, which is called a face-centred central-composite design, the axial point was then placed at the low and high values. Table 3 shows the complete experimental design matrix, where the runs were randomized to avoid bias in response gain. The extreme right column shows the experimentally observed average reading of kerf width.

3.3. Analysis of Variance

ANOVA is a computational technique to quantitatively estimate the contribution that each parameter makes on the overall observed response. ANOVA is accomplished by separating the total variability of the S/N ratios (SS_{tot}), which is measured by the sum of the squared deviations from the total mean S/N ratio into contributions by each of the parameters and the error:

$$SS_{tot} = SS_T + SS_E \tag{11}$$

The total sum of square deviations from the total mean S/N ratio can be calculated as [23]:

$$SS_T = \sum_{i=1}^{n_t} (\eta_i - \bar{\eta})^2 \tag{12}$$

where, η_t is the total number of experiment trials, η_i is the S/N ratio in i^{th} trial in the OA and $\bar{\eta}$ is the total mean S/N ratio:

$$\bar{\eta} = \frac{1}{n_t} \sum_{i=1}^{n_t} \eta_i \tag{13}$$

The sum of square due to parameter Q can be computed as:

$$SS_Q = \sum_{i=1}^{k} n_{Qk} [\bar{\eta}_{Qk} - \bar{\eta}]_i^2 \tag{14}$$

Subsequently, SS_T can be used to measure the relative influence of the process parameters on the response. The percentage contribution (ρ) of parameter Q can be calculated as:

$$\rho(\%) = \frac{SS_Q}{SS_T} \times 100 \tag{15}$$

The final step in the optimization methodology is the verification of the improvement of the quality characteristic. For that purpose, a confirmation experiment should be carried out implying the (near) optimal levels of the control parameters.

4. Results and Discussion

4.1. Taguchi's Technique

The response analysis, represented by graphs in Figure 1, indicates the change in response when a given factor varies from lower to higher level. Figure 1 represents the main effects plot for the mean value of kerf width against cutting speed, laser power, frequency, duty cycle, and gas pressure. It can be seen that greater laser power and duty cycle give a better kerf width. This phenomenon is witnessed probably due to an increase of the incident laser power absorbed by the work materials. On the other hand, it was experiencing inverse effects for cutting speed over the kerf width. The effect of the cutting speed is correlated by the fact that, as the cutting speed increases, the interaction time between the laser beam and work materials distorts.

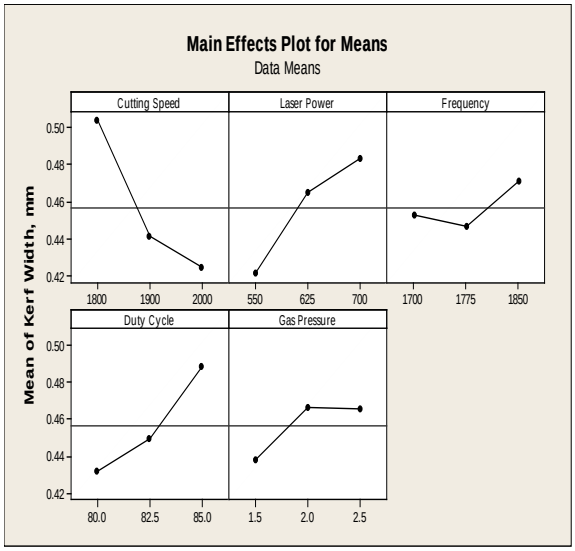

Figure 1. Main effects plot of design parameters over kerf width

The effect of various factors at different levels for responses kerf width is shown in Table 5. The optimum parameter level for minimum value of kerf width is $A_3B_1C_2D_1E_1$. Tabulated in Table 5, the optimal combination of the parameters for the kerf width could be achieved by using a cutting speed of 2000 mm/min, laser power of 550 W, frequency of 1775 Hz, duty cycle of 80 %, and gas pressure of 1.5 Bar. The ANOVA table of the S/N ratio for the kerf width as shown in Table 6 clearly indicates that, the influence of cutting speed has the greatest effect (43.65 % contribution) on the kerf width, followed by the laser power (24.98 % contribution), and duty cycle (20.87 % contribution). However, the other parameters are least significant effect (3.98 % - 6.52 % contribution) compared to earlier.

4.1.1. Regression Analysis

The second-order response surface representing the kerf width can be expressed as a function of cutting parameters such as cutting speed, laser power, frequency, duty cycle and gas pressure. From the observed data for kerf width, the response function has been determined in coded factors units as:

Kerf Width *= 0.46 - 0.026*A + 0.023*B – 0.011*C - 5.556E-005*D + 0.014*E – 0.040*A*B – 0.016*A*C - 5.075E-003*A*E + 0.027*B*C - 0.011*B*E +0.011*C*E + 7.250E-003*D*E* (16)

4.2. RSM Technique

The influence of cutting speed, laser power, frequency, duty cycle and gas pressure was investigated through the modelling stages. The analysis of variance (ANOVA) for kerf width of Industrial PVC foam is shown in Table 7. This analysis was carried out for level of confidence not less than 95 % which is a criteria to be set into RSM.

Table 7 presents the ANOVA for kerf width. The significance of the model is revealed according to the F-value of 5.15 model. There was only a probability of 0.11 % of noise in this "F-Value model". If the values of "Probability > F", and if they are lesser than 5 % (0.05), then the model is said to be sound; thus, A, B, D, AC, AD, BD, and BE are considered as excellent model terms. In

case that the values are greater than 0.1 (10 %), the model terms are said to be insignificant and impractical to be considered. The "Lack of Fit F-value" of 2.28 reveals that lack of fit, related to the pure error, is not significant. In this case, since, the intention here is to fit the model, it is good to have an insignificant lack of fit.

The cutting speed and laser power are two parameters affecting the kerf width. According to Figure 2(a), higher cutting speed at lower duty cycle gives a smaller kerf width due to a less interaction time. On the other hand, Figure 2(b) reveals that frequency is inverse proportional to the kerf width. Hence, the greater the cutting speed, the higher the frequency and the smaller kerf width is attainable. It should be noted that the effect of duty cycle slightly decreases the kerf width, while, laser power is inverse to that effect as its correlation is clearly visible in Figure 2(c). Therefore, it can be summarized that combination of lower side laser power and higher side duty cycle produces better kerf width. The lower laser power and gas pressure, it is then more favourable for kerf width, as shown in Figure 2(d). It is clearly evident that kerf width increases with laser power as the laser beam energy mainly depends on laser power. High laser power generates high thermal energy, which produces higher kerf width in return.

Table 5. S/N ratio response

Source	Factors	S/N ratios (dB)			Delta	Rank
		Level 1	Level 2	Level 3		
A	Cutting speed	6.022	7.133	7.484[a]	1.462	1
B	Laser Power	7.535[a]	6.682	6.423	1.112	2
C	Frequency	6.892	7.047[a]	6.700	0.346	5
D	Duty cycle	7.316[a]	7.003	6.320	0.996	3
E	Gas pressure	7.264[a]	6.646	6.730	0.617	4

[a]Optimum parameter level

Table 6. ANOVA for S/N ratio

Source	df	SDG	MS	F-Value	Contribution (%)
A	2	0.0316	0.0158	11.862	43.65
B	2	0.0181	0.0090	6.788	24.98
C	2	0.0029	0.0014	1.082	3.98
D	2	0.0151	0.0075	5.671	20.87
E	2	0.0047	0.0024	1.771	6.52
Total	26	0.072			

df: degrees of freedom; SDG: sum of square; MS: mean square

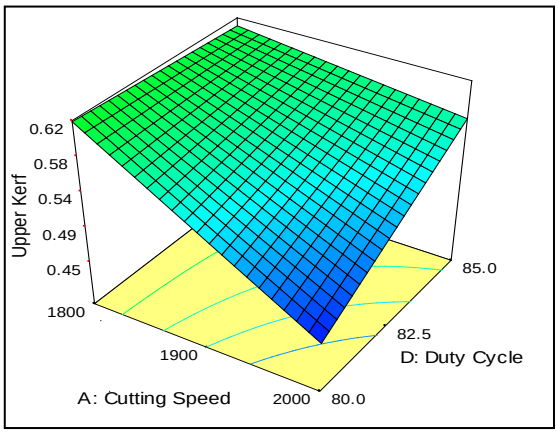

(a)

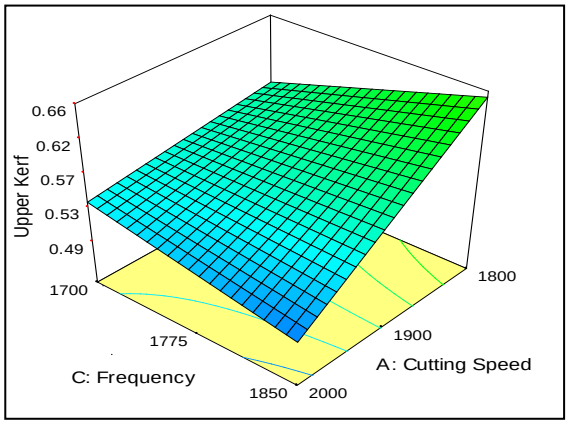

(b)

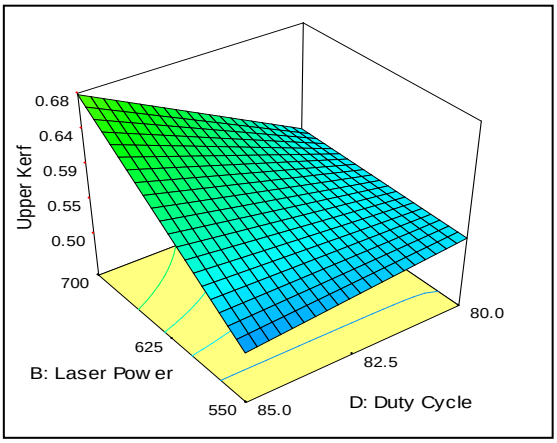

(c)

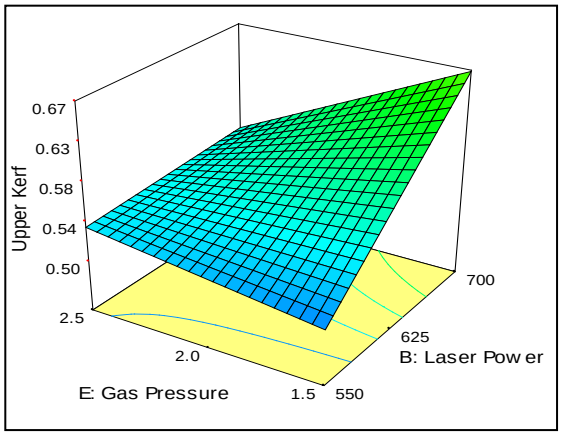

(d)

Figure 2. 3D surface of kerf width model; (a) effects of cutting speed and duty cycle, (b) effects of cutting speed and frequency, (c) effects of laser power and duty cycle, and (d) effects of laser power and gas pressure.

4.2.1. Mathematical Modelling

The models for the quality of cut were developed to evaluate the relationship of laser cutting parameters to the kerf width. Through these models, experimental results of kerf width by any combination of machining parameters can be estimated. From the factor of interaction (2FI) behaviour of model, the polynomial equation implied several process parameters as Equation 10. The developed mathematical models are listed below in terms of actual factors. Equation 17 is for the prediction of kerf width. Optimization is carried out by finding the desirability value in Table 8, which shows a part of the result generated. The optimum condition is when kerf width equals 0.278 that can be achieved when machining at cutting speed of 1800 m /min, laser power of 550 W , frequency of 1700 H z, duty cycle of 80 % , and gas pressure of 2.5 Bar. This optimum condition is not similar with the one obtained using Taguchi method. This may be due to a small number of data that caused the misleading of the result. Therefore, it is recommend that the RSM (CCD) be used to obtain an accurate optimization condition.

4.3. Experimental Validation

Experimental validation is the final step in the modelling process to investigate the accuracy and robustness of the established model. Thus, in order to verify the capability of the developed regression model and RSM model, five randomly picked validation experiments were carried out within the range of explored experimental parameters. Table 10 presents the experiments order, the actual values, the predicted values and their deviations (percentage errors) for Taguchi regression model as well as Table 9 for RSM model. It is a common practice for a n onlinear process, if the average error deviation is less than 15 %, then the optimization can be considered valid for the model to be accepted. The final analysis involves comparing the predicted values of the established model with experimentally validated values; it was found that the average error was below 15 % , confirming and concluding the methodology in establishing the model was systematic in performing this scientific research. The Taguchi method revealed the error was 14.61 %, meanwhile the RSM showed 8.93 %.

Kerf Width *= 7.769 – 0.0028*A – 0.0080*B + 0.0099*C – 0.3360*D + 2.7906*E – 9.17E-08*A*B - 4.22E-06*A*C + 1.28E-04*A*D - 3.54E-04*A*E - 4.02E-06*B*C + 2.18E-04*B*D - 1.01E-03*B*E + 5.67E-06*C*D + 1.17E-04*C*E - 0.0210*D*E* (17)

Table 7. ANOVA table for kerf width (RSM).

Source	Sum of Square	Degrees of freedom	Mean Square	F Value	P Value
Model	0.21	15	0.014	5.15	0.0011
A	0.044	1	0.044	16.17	0.0010
B	0.035	1	0.035	13.02	0.0024
C	0.0008	1	0.0008	0.30	0.5905
D	0.014	1	0.014	5.19	0.0368
E	0.008	1	0.008	2.99	0.1030
AB	0.000008	1	0.000008	0.003	0.9584
AC	0.016	1	0.016	5.96	0.0267
AD	0.016	1	0.016	6.07	0.0254
AE	0.005	1	0.005	1.86	0.1920
BC	0.008	1	0.008	3.04	0.1006
BD	0.027	1	0.027	9.88	0.0063
BE	0.023	1	0.023	8.51	0.0101
CD	0.00002	1	0.00002	0.007	0.9358
CE	0.003	1	0.003	0.11	0.7405
DE	0.011	1	0.011	4.11	0.0597
Residual	0.043	16	0.003		
Lack of fit	*0.036*	*11*	*0.003*	*2.28*	*0.1872*
Pure Error	*0.007*		*5*	*0.001*	
Cor Total	0.25	31			

Table 8. Optimization using desirability criterion.

No.	*A*	*B*	*C*	*D*	*E*	Kerf Width	Desirability	
1	1800	550	1700	80.0	2.5	0.278	0.976	Selected
2	1800	554	1700	80.0	2.5	0.280	0.971	
3	1800	550	1700	80.8	2.5	0.289	0.956	

Table 9. Experimental validation (RSM)

Exp. No.	Factor levels A	B	C	D	E	Values	Response Kerf width
1	1850	663	1813	81.3	1.8	Actual	0.547 mm
						Predicted	0.609 mm
						Error	10.18 %
2	1950	663	1813	83.8	2.3	Actual	0.533 mm
						Predicted	0.559 mm
						Error	3.09 %
3	1950	588	1813	81.3	2.3	Actual	0.441 mm
						Predicted	0.511 mm
						Error	13.70 %
4	1850	663	1738	83.8	1.8	Actual	0.602 mm
						Predicted	0.643 mm
						Error	6.38 %
5	1850	588	1738	81.3	1.8	Actual	0.487 mm
						Predicted	0.549 mm
						Error	11.29 %
						$\overline{X}$ **Error**	**8.93 %**

Table 10. Experimental validation (Taguchi)

Exp. No.	Factor levels A	B	C	D	E	Values	Response Kerf width
1	1850	663	1813	81.3	1.8	Actual	0.547 mm
						Predicted	0.609 mm
						Error	10.18 %
2	1950	663	1813	83.8	2.3	Actual	0.533 mm
						Predicted	0.559 mm
						Error	3.09 %
3	1950	588	1813	81.3	2.3	Actual	0.441 mm
						Predicted	0.511 mm
						Error	13.70 %
4	1850	663	1738	83.8	1.8	Actual	0.602 mm
						Predicted	0.643 mm
						Error	6.38 %
5	1850	588	1738	81.3	1.8	Actual	0.487 mm
						Predicted	0.549 mm
						Error	11.29 %
						$\overline{X}$ **Error**	**8.93 %**

5. Conclusion

The experiment reveals the high level of interest in comparing Taguchi and RSM to predict response in laser non-linear process. Normally, there is a l ack of comparative studies concerning the performance of the optimization techniques; in other words which method would be better for a given optimization problem. Both analytical tools are outstanding at developing mathematical modelling in laser processing. However, RSM is more promising due to its giving very low average error towards modelling and experimental validation. The desirability criterion available in RSM will easily help users to determine the optimum condition. Significance of interactions and square terms of parameters are more clearly predicted in RSM. The RSM shows significance of all possible combinations of interactions and square terms as depicted in Table 5. Taguchi technique is normally used in linear interactions only. This is due to the fact that in Taguchi design, interactions between controls factors are aliased with their main effects. 3D surfaces generated by RSM can help in visualizing the effect of parameters on response in the entire range specified whereas Taguchi technique gives the average value of response at given level of parameters (Figure 1 a nd 2). Thus RSM is a promising analytical tool to predict the response which suits the range of parameters studies.

Acknowledgement

The authors would like to thank Universiti Teknikal Malaysia Melaka (UTeM) for awarding MyBrain UTeM scholarship for the post graduate which enabled the progression of this critical research. Special thanks goes to the Ministry of Higher Education for awarding a r esearch grant (grant no.: PRGS/2012/TK01/FKP/02/1/T00003) which succeeded the completion of this research. The authors are also very much obligated to sincerely thank the management of UES International Pte.Ltd. for sponsoring work materials which enabled the accomplishment of this analytical tools modelling and validation stage. Last but not least, the authors would also like to express their sincere thanks and gratitude to management of Centre for Research and Innovation Management (CRIM) and Faculty of Manufacturing Engineering, Dr. Azizah Shaaban and Dr. Mohd Rizal Salleh respectively and not forgetting technical support of laser machining centre, Mr. Mohd Ghazalan.

References

[1] Steen WM. (1991). *Laser Material Processing*, 3rd edn., New York: Springer.

[2] Canel, T., Kaya, A. U., & Çelik, B. (2012). Parameter optimization of nanosecond laser for microdrilling on PVC by Taguchi method. *Optics & Laser Technology*, 44(8), pp. 2347–2353.

[3] Kumar Pandey, A., & Kumar Dubey, A. (2012). Simultaneous optimization of multiple quality characteristics in laser cutting of Titanium Alloy sheet. *Optics & Laser Technology*, 44(6), pp. 1858–1865.

[4] Badkar, D. S., Pandey, K. S., & Buvanashekaran, G. (2010). Parameter optimization of laser transformation hardening by using Taguchi method and utility concept. *The International Journal of Advanced Manufacturing Technology*, 52(9-12), pp. 1067–1077.

[5] Eltawahni, H. A., Olabi, A. G., & Benyounis, K. Y. (2011). Investigating the CO_2 laser cutting parameters of MDF wood composite material,*Optics & Laser Technology*, 43(3), pp. 648–659.

[6] Negarestani, R., Li, L., Sezer, H. K., Whitehead, D., & Methven, J. (2009). Nano-second pulsed DPSS Nd:YAG laser cutting of CFRP composites with mixed reactive and inert gases. *The International Journal of Advanced Manufacturing Technology*, 49(5–8), pp. 553–566.

[7] El-Taweel, T. A., Abdel-Maaboud, A. M., Azzam, B. S., & Mohammad, A. E. (2008). Parametric studies on the CO_2 laser cutting of Kevlar-49 composite. *The International Journal of Advanced Manufacturing Technology*, 40(9–10), pp. 907–917.

[8] Aggarwal, A., Singh, H., Kumar, P., & Singh, M. (2008). Optimizing power consumption for CNC turned parts using response surface methdology and Taguchi technique – A comparative analysis. *Journal of Materials Processing Technology*, 200(1-3), pp. 373-384.

[9] Stournaras, A., Stavropoulos, P., Salonitis, K., & Chryssolouris, G. (2009). An investigation of quality in CO_2 laser cutting of Aluminum. *CIRP Journal of Manufacturing Science and Technology*, 2(1), pp. 61–69.

[10] Masmiati, N., & Philip, P. K. (2007). Investigations on laser percussion drilling of some Thermoplastic Polymers. *Journal of Materials Processing Technology*, 185(1-3), pp. 198–203.

[11] Avanish, K. D., & Vinod, Y. (2008). Multi-Objective optimization of Nd:YAG laser cutting of Nickel-Based Superalloy sheet using orthogonal array with principal component analysis. *Optics and Lasers in Engineering*, 46(2), pp. 124 – 132.

[12] Mathew, J., Goswami, G. L., Ramakrishnan, N., & Naik, N. K. (1999). Parametric studies on pulsed Nd:YAG laser cutting of carbon f ibre reinforced plastic composites. *Journal of Materials Processing Technology*, 89–90, pp. 198–203.

[13] Corcoran, L., Sexton, L., Seaman, B., Ryan, P., & Byrne, G. (2002). The laser drilling of multi-layer aerospace material systems. *Journal of Materials Processing Technology*, 123(1), pp. 100–106.

[14] Chen, Y. H., Tam, S. C., Chen,W. L., & Zheng, H. Y. (1996). Application of Taguchi method in the optimization of laser micro-engraving of Photomasks. *International Journal of Materials & Product Techonology*, 11(3-4), 333–344.

[15] Verma, A. S., Suri, N. M., & Kant. S. (2012). Effect of process parameter of AL-6063 based fly ash composites using Taguchi. *International Journal of Applied Engineering Research*, 7(11), 1856-1859.

[16] Phadke, M. S. (1989). Quality engineering using robust design, Prentice Hall: New Jersey.

[17] Gill A. S., Thakur. A., & Kumar. S. (2012). Effect of Deep Cryogenic Treatment on the surface roughness of OHNS Die Steel after WEDM. *International Journal of Applied Engineering Research*, 7(11), 1508-1512.

[18] Dubey, A. K., & Yadava, V. (2007). Robust parameter design and multi-objective optimization of laser beam cutting for Aluminium Alloy sheet. *The International Journal of Advanced Manufacturing Technology*, 38(3-4), 268–277.

[19] Arce, R. G. (2005). *Nonlinear signal processing: A statistical approach*, John Wiley & Sons.

[20] Chatfield, C. (1995). *Problem solving: A statistician's guide* (2nd edition, Chapman & hall/CRC, 1995).

[21] Shetty, R., Pai, R., Rao, S. S., & Kamath, V. (2008). Machinability study on discontinuously reinforced aluminium composites (DRACs) using response surface methodology and Taguchi's design of experiments under dry cutting condition. *Maejo International Journal of Science and Technology*, 2(1), pp. 227-239.

[22] Montgomery, D. C. (1997). *Design and Analysis of Experiments*, 5th edn., Wiley, New York.

[23] Madic, M. J., & Radovanovic, M. R. (2013). Identification of the robust conditions for minimization of the HAZ and burr in CO_2 laser cutting, *FME Transactions*, 41, pp. 130-137.

JJMIE

Volume 8 Number 1, February. 2014
ISSN 1995-6665
Pages 43 - 49

Jordan Journal of Mechanical and Industrial Engineering

The Reliability Analysis of Horizontal Vibration of Elevator Based on Multi-State Fuzzy Bayesian Network

Rui-jun Zhang*, Wei-wei Yang, Xiao-wei Wang

School of Mechanical and Electrical Engineering, Shandong Jianzhu University, Jinan, China

Abstract

Reliability analysis is one of the important constituent parts of elevator safety evaluation. In order to obtain the exact value of fault probability of components in elevator system, by combining fuzzy theory with Bayesian network approach, we proposed a reliability analysis method of multi-state system based on fuzzy Bayesian networks. By expanding the traditional two-state Bayesian network to multi-state system, multi-state Bayesian network model of horizontal vibration of elevator is established. The language variable of the root probability is transformed into triangular fuzzy numbers under different states. After equalization, defuzzification and normalization, the precision probabilities can be gotten and then introduced to the multi-state Bayesian network model. The posterior probability and the probability importance degree of various root nodes are calculated with multi-state Bayesian network algorithm. The result can provide quantitative evaluation for the reliability of multi-state horizontal vibration of the elevator. Compared with the fuzzy fault analysis method based on T-S, the method we proposed is valid.

***Keywords**: Reliability Analysis; Fuzzy Theory; Bayesian Network; Horizontal Vibration*

1. Introduction

The elevator's vibration is one of the important indicators of measuring the quality of the elevator [1]. With the increase of high-rise buildings and the speed of elevators, elevator vibration will exacerbate [2]. Studies have shown that the horizontal vibration of the elevator has a linear relationship with its running speed [3]. Lots of factors can cause horizontal vibration of the elevator, mainly including manufacturing and fixing errors of rail, the guide wheel shape of the rolling guide shoes, the static equilibrium of the car and the change of passenger load, hoist way overall and hoist way airflow, the car speed [4].

Currently, the elevator fault diagnosis methods mainly include fault diagnosis method based on fault tree, fault diagnosis method based on expert system, fault diagnosis method based on artificial neural networks, fault diagnosis method based on information fusion, and so on. Zong et al. [5] proposed a fault diagnosis method of elevator based on fault tree expert system and established the fault diagnosis model of the elevator system and expert knowledge, thus solving the problem of obtaining expert system knowledge and poor integrity of knowledge. The literature [6] used the method of combining fault tree and expert system to improve the diagnosis accuracy in the elevator fault diagnosis. Zong et al. [7] applied BP neural network to solve the problem of traditional expert systems and achieved good results in the failure of the elevator. Li et al. [8] applied the information fusion technology to equipment fault diagnosis according to the multi-information characteristics of electrical fault diagnosis, improving the accuracy and reliability of fault diagnosis. Although these methods have a very good application prospects in the elevator system fault diagnosis and reliability analysis, their applications are limited because of the complicated calculation process.

In recent years, many methods of system reliability have been proposed and applied with the development of reliability theory, such as reliability block diagram analytical method [9], fault tree analysis method [10], binary decision diagram analytical method [11], importance analysis method of fuzzy fault tree based on T-S model [12], and Bayesian network analysis methods [13-14]. Bayesian network, proposed by Pearl in 1988, can express and analyze the uncertainty of information well and bi-directional reasoning of reliability of the system can be achieved. BN can describe polymorphism of events and non-deterministic logical relation, so it has a very good application in reliability, fault diagnosis and other fields [15-16]. Meanwhile, Bayesian network based on probability theory and graph theory has both solid mathematical foundation and intuitive semantics, which is an effective model to express the knowledge of uncertainty and the theory of reasoning [17]. Bayesian network not only has strong modeling capabilities, but also has a strong inference mechanism. With the complex of Bayesian network model, inference algorithms [18] tends to be perfect and simple and can solve well the probability problem of each node in Bayesian network model.

The multi-state fuzzy Bayesian network is applied to the elevator system. Because it is difficult to obtain the exact probability of each factor causing horizontal

* Corresponding author. makhlouf11@yahoo.com

vibration of the elevator, it is obtained through the method of group decision-making with the help of the expertise. Then the expertise is transferred into triangular fuzzy function to obtain precise priori probabilities of BN nodes. At last, the important factors are gotten, causing the car horizontal vibration.

2. Multi-State Bayesian Network Overview

Bayesian network, BN for short, is a graphical network based on probabilistic inference. BN is composed of a DAG (directed acyclic graph) and certain CPT (conditional probability tables). The directed graph is called DAG (directed acyclic graph) if the directed graph cannot be from one point to the original point after a number of edges. DAG consists of representative variable node and directed edges connecting these nodes, in which nodes present variables and directed edges represent the relationship between variables. DAG describes the network structure of BN, which is the qualitative part. CPT is a table indicating the number dependence relationships of probability between the variable and its parent node, which describes network parameters of the BN, so it is quantitative section. According to the Bayesian formula, the definition of the conditional probability is given:

$$P(A/B)=\frac{P(B/A)P(A)}{P(B)} \tag{1}$$

Where P(A) is priori probability; P(A/B) is posterior probability; P(B/A) is likelihood ratio.

If A is a multi-state variable having the states of ($a_1, a_2, \cdots, a_n$), the definition of the total probability formula is:

$$P(B)=\sum_{i=1}^{n} P(B/A=a_i)P(A=a_i) \tag{2}$$

An obvious advantage of Bayesian network is bidirectional inference , i.e. causal reasoning and diagnostic reasoning. Causal reasoning is deduced from the priori probability to posterior probability that means that results are deduced by the reason. The process of diagnostic reasoning is contrary to that of causal reasoning. The probability of the working network can be calculated through bidirectional reasoning when any one or more of the variable nodes are given because the node variable of Bayesian network is independent. Then the probability of any one or more fault nodes can be calculated through the reverse inference when the network is fault, which can diagnose the weak link of the network. Bayesian network uses bucket elimination algorithm [19] to conduct the causal inference of network and uses Bayesian formula to conduct diagnostic reasoning, thus achieving bidirectional inference of Bayesian network.

According to the chain rule, when BN has many nodes $X_1, X_2, \cdots, X_n$, the joint distribution is:

$$P(X_1, X_2, \cdots, X_n)=\prod_{i=1}^{n} P(X_i/Pa_i) \tag{3}$$

Therefore, the complex BN can be simplified and disassembled with the help of conditional independence among variables nodes.

3. Multi-State Bayesian Network Model of Horizontal Vibration of the Elevator

Multi-state system is divided into discrete multi-state system and continuous multi-state system. This thesis mainly discusses discrete multi-state system. For example, a system has normal operating state, degraded working condition and completely failed state. Usually 0, 1, 2 are used to represent the three states.

3.1. Modeling Steps

Bayesian networks analyze various causes of fault (network nodes) from part to whole, from bottom to top, which are dendrites. First, we determine the network nodes, the root node of the network represents the basic event of the system and the leaf node represents the system. Then we identify discrete systems and multi-states of system components. Finally, the probability of each state of component is given. Since the probability of each state of component is difficult to obtain, it is obtained through a language variable given by the expertise. The directed arc of Bayesian network represents the dependency relationship between variables, and probability distribution table shows the dependence degree between variables. Then priori probability information and sample knowledge are combined.

3.2. Modeling Construction

Many factors can affect the horizontal vibration of the elevator, but the present article considers and analyzes the factors from the aspects of guidance system and car system. Guidance system consists of guide shoes, guide rails and rack components.

3.2.1. Each Node of the Model

Various factors affecting the horizontal vibration are mainly analyzed from the following two aspects: (1) Guidance system: the guide wheel shape of rolling guide shoe, surface profile of elevator guide rail, the installation quality of elevator guide rail, and (2) Car system: static equilibrium of the car and the load size of the passenger. Each influence factor can be seen as the root node of the Bayesian network. The surface profile and installation quality of elevator guide rail are quality problem of the guide, which can be seen as an intermediate node. The horizontal vibration of the elevator can be seen as the leaf node of the network.

3.2.2. Logical relationships between Nodes

Logical “and” relationships are between surface profile of elevator guide rail and quality of the installation of the elevator guide rail and between static equilibrium of the car and the load size of the passenger. Each factor will lead to the occurrence of the above event. Logical “or” relationships are between the guide wheel shape of rolling guide shoe and the problem of guide quality and between guidance system and the car system. Each factor has three states. For example, the surface profile of the guide has three different states: the ideal state with small roughness, the normal state with the roughness within a reasonable range and large roughness having a serious impact on horizontal vibration.

3.2.3. The Model of Horizontal Vibration of Elevator under the Influence of Guidance System and Car System

The Bayesian network model of elevator horizontal vibration is established based on the logical relationship between the factors.

The root nodes X_1, X_2, X_3, X_4 and X_5, respectively, represent the surface profile of the elevator guide rail, the installation quality of the elevator guide rail, the guide wheel shape of the rolling guide shoe, the static equilibrium of the car, and the load size of passenger. A_1, A_2 and A_3 are used respectively to signify guidance system, car system and the quality of guide rail. T represents the leaf node. Each node has three states that are shown by using state space $\{0,1,2\}$. 0 represents the normal state, 1 represents semi-fault state, and 2 represents completely failed state. According to the dependencies between nodes, directed arcs are used to connect root node with leaf node to indicate the relationship between parent and offspring. Then the status space of all nodes and the conditional probability of the intermediate node are determined. Bayesian network model of horizontal vibration elevator is shown in Figure 1. The conditional probability tables of the node are omitted due to the limited space.

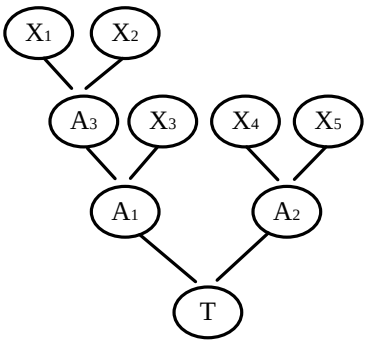

Figure 1. The Bayesian network model of horizontal vibration of elevator

4. The Analysis of Multi-State Bayesian Network Model of Horizontal Vibration of Elevator

4.1. Fuzzy Approach

The horizontal vibration factors are often in a variety of fault conditions in the elevator. The different fault conditions are interrelated and mutually transformed in the process of fault change. Fault state is often manifested as "this and that" state. In other words, it is fuzzy. The presence of ambiguity makes it difficult to obtain an exact probability value of each state. For example, the installation quality of the elevator guide rail may change when the surface profile of elevator guide rail changes. Thus, it is difficult to determine the installation quality of the elevator guide rail. Here, a fuzzy number is used to process this condition. The forms of fuzzy numbers are various, such as a triangular fuzzy number, a trapezoidal fuzzy number, a rectangular fuzzy number and an irregular shaped fuzzy number. The triangular fuzzy number is used to represent the probability of occurrence because the reference function of the triangular fuzzy is more convenient to handle and algebra is relatively easy. A form of membership function of the triangular fuzzy number is the following:

$$\mu(x)=\begin{cases}\max(0,\dfrac{x-a}{m-a}), x\le m\\ \max(0,\dfrac{b-x}{b-m}), x>m\end{cases} \quad (4)$$

Therefore, the triangular fuzzy number can be represented by three parameters: " a ", "m" and "b" denoted by (a,m,b). For two triangular fuzzy numbers $A=(a_1,m_1,b_1)$ and $B=(a_2,m_2,b_2)$, the algorithm [20] is the following:

The sum of two numbers:

$$A\oplus B=(a_1+a_2,m_1+m_2,b_1+b_2) \quad (5)$$

A precise number K exists, then:

$$\frac{A}{k}=(\frac{a_1}{k},\frac{m_1}{k},\frac{b_1}{k}) \quad (6)$$

The result is gotten through group decision-making approach with the help of expertise under the condition of not being able to obtain exactly the state probability of event. In order to connect judging result of event probability given by expert with fuzzy number, we introduce seven language variables [21] of "very high", "high", "on the high side", "secondary", "on the low side", "low", "very low". Table 1 is the corresponding relation between language variable and fuzzy number. Figure 2 is the membership function of triangular fuzzy numbers.

Table 1. Semantics value of event occurring probability and corresponding triangular fuzzy

Sequence number	Semantics value	triangular fuzzy number
1	very high	(0.9, 1.0, 1.0)
2	high	(0.7, 0.9, 1.0)
3	on the high side	(0.5, 0.7, 0.9)
4	secondary	(0.3, 0.5, 0.7)
5	on the low side	(0.1, 0.3, 0.5)
6	low	(0, 0.1, 0.3)
7	very low	(0, 0, 0.1)

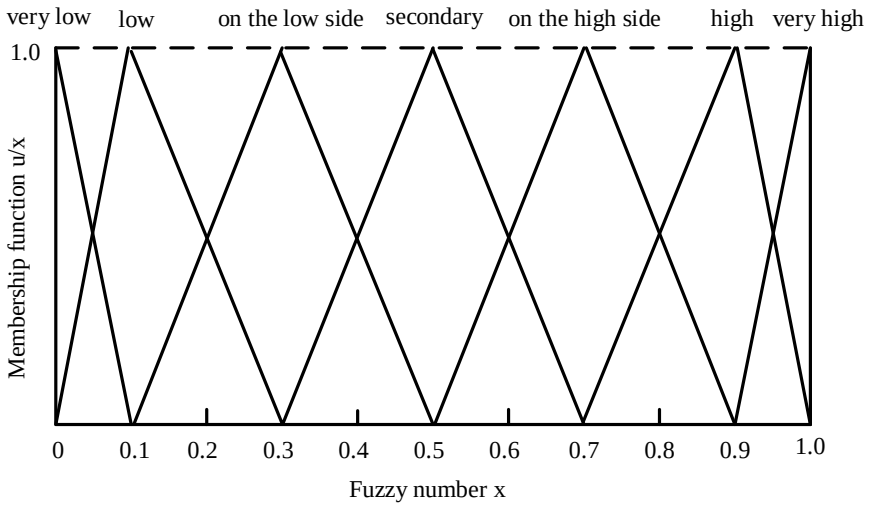

Figure 2. Membership function of triangular fuzzy number

The information of expertise is transformed into a fuzzy number expressed by a triangular fuzzy number through the above method.

4.2. The Probability Importance of Multi-State Bayesian Network:

Four experts estimate occurring probability of each root node in each state in horizontal vibration of elevator. They have been working in the elevator industry for many years and know the affecting factor of the horizontal vibration of elevator well. Language variable is gotten by the experts independently. In the evaluation process, the experts should consider comprehensively the using environment, production quality and frequency of failures in recent years of the various components. And the language variable of the same node given by different expert is different because every expert has a different opinion considering their familiarity, the extent grasping or human factors. Then the language variable is transformed into a fuzzy probability. The language variables of the expert and the corresponding fuzzy number are shown in Table 2.

Table 2.Experts' opinion of root nodes in different states

Root node		Expert 1	Expert 2	Expert 3	Expert 4
X_1	0	high (0.7,0.9,1.0)	very high (0.9,1.0,1.0)	high (0.7,0.9,1.0)	high (0.7,0.9,1.0)
	1	low (0,0.1,0.3)	very low (0,0,0.1)	low (0,0.1,0.3)	very low (0,0,0.1)
	2	very low (0,0,0.1)	low (0,0.1,0.3)	on the low side (0.1,0.3,0.5)	low (0,0.1,0.3)
X_2	0	high (0.7,0.9,1.0)	on the high side (0.5,0.7,0.9)	on the high side (0.5,0.7,0.9)	secondary (0.3,0.5,0.7)
	1	on the low side (0.1,0.3,0.5)	on the low side (0.1,0.3,0.5)	low (0,0.1,0.3)	low (0,0.1,0.3)
	2	low (0,0.1,0.3)	low (0,0.1,0.3)	on the low side (0.1,0.3,0.5)	very low (0,0,0.1)
X_3	0	very high (0.9,1.0,1.0)	very high (0.9,1.0,1.0)	very high (0.9,1.0,1.0)	high (0.7,0.9,1.0)
	1	very low (0,0,0.1)	very low (0,0,0.1)	low (0,0.1,0.3)	very low (0,0,0.1)
	2	very low (0,0,0.1)	low (0,0.1,0.3)	low (0,0.1,0.3)	low (0,0.1,0.3)
X_4	0	high (0.7,0.9,1.0)	on the high side (0.5,0.7,0.9)	high (0.7,0.9,1.0)	secondary (0.3,0.5,0.7)
	1	on the low side (0.1,0.3,0.5)	low (0,0.1,0.3)	low (0,0.1,0.3)	very low (0,0,0.1)
	2	low (0,0.1,0.3)	very low (0,0,0.1)	on the low side (0.1,0.3,0.5)	on the low side (0.1,0.3,0.5)
X_5	0	on the high side (0.5,0.7,0.9)	very high (0.9,1.0,1.0)	secondary (0.3,0.5,0.7)	on the high side (0.5,0.7,0.9)
	1	low (0,0.1,0.3)	on the low side (0.1,0.3,0.5)	very low (0,0,0.1)	very low (0,0,0.1)
	2	very low (0,0,0.1)	low (0,0.1,0.3)	on the low side (0.1,0.3,0.5)	low (0,0.1,0.3)

According to Table 2, the language variable of root node X_2, which is the probability of the state of 0 given by the first expert, is transformed into fuzzy probability $\tilde{P}_{20}^{1} = (0.7,0.9,1.0)$.

In order to transform the experts' opinion into a relatively reasonable fuzzy probability, four experts' evaluation results are synthesized by using arithmetic average method. Average formula of fuzzy probability of the root node X_i ($i=1$, 2, 3) in the state of j is:

$$\tilde{P}_{ij}^{'} = \frac{P_{ij}^{1} \oplus P_{ij}^{2} \oplus \cdots \oplus P_{ij}^{4}}{4} = (a_{ij}^{'}, m_{ij}^{'}, b_{ij}^{'}) \quad (7)$$

According to formula (7), the fuzzy probability mean of the root node in each state is shown in Table 3.

Table 3.: Fuzzy probability of the root node in different states

Fuzzy probability	State j		
	0	1	2
$\tilde{P}_{1j}^{'}$	(0.75,0.925,1)	(0,0.05,0.2)	(0.025,0.125,0.3)
$\tilde{P}_{2j}^{'}$	(0.5,0.7,0.875)	(0.05,0.2,0.4)	(0.025,0.125,0.3)
$\tilde{P}_{3j}^{'}$	(0.85,0.975,1)	(0,0.025,0.15)	(0,0.075,0.25)
$\tilde{P}_{4j}^{'}$	(0.55,0.75,0.9)	(0.025,0.125,0.3)	(0.05,0.175,0.35)
$\tilde{P}_{5j}^{'}$	(0.55,0.725,0.875)	(0.025,0.1,0.25)	(0.025,0.125,0.3)

In order to transform fuzzy probability into exact probability, we use "mean area method" [22] to resolve the ambiguity of fuzzy probability. The exact probability of the root node X_i in the state of j is

$$P_{ij}^{'} = \frac{a_{ij}^{'} + 2m_{ij}^{'} + b_{ij}^{'}}{4} \quad (8)$$

According to formula (8), the exact probability mean of each root node in different states is shown in the Table 4.

Table 4. The exact probability of each root node in different states

Fuzzy probability	State j		
	0	1	2
$P_{1j}^{'}$	0.9	0.0750	0.14375
$P_{2j}^{'}$	0.69375	0.2125	0.14375
$P_{3j}^{'}$	0.95	0.0500	0.1
$P_{4j}^{'}$	0.7375	0.14375	0.1875
$P_{5j}^{'}$	0.71875	0.11875	0.14375

In order to make the sum of the probability of the root node in various states be one, we conduct "normalization" on exact probability of the root node in various states. After the normalization, the exact probability of root node X_i in the state of j is:

$$P_{ij} = \frac{P_{ij}^{'}}{\sum_{j=0}^{2} P_{ij}^{'}} \quad (9)$$

According to the above formula, the exact probability mean of each root node in different states is shown in Table 5.

Table 5. After the normalization, the exact probability of each root node in different states

Fuzzy probability	State j		
	0	1	2
P_{1j}	0.804469	0.067039	0.128492
P_{2j}	0.660714	0.202381	0.136905
P_{3j}	0.863636	0.045455	0.090909
P_{4j}	0.690058	0.134503	0.175439
P_{5j}	0.732484	0.121019	0.146497

The probability of intermediate nodes and leaf nodes in different states can be calculated through priori probabilities of the root node in various states obtained by the above method and the known conditional probability. According to Bayesian formula, we use the bucket elimination method to calculate the posterior probability of the root node in various states.

The probabilities of leaf node in different states are gotten by algorithms of multi-state BN. $P_{T0}=0.739$, $P_{T1}=0.131$, $P_{T2}=0.130$. And then the probability of the root node in various states is obtained when the leaf node T is in different states, which is shown in Table 6.

Table 6.The posterior probability of different root nodes

T		0	1	2
X_1	0	0.862	0.577	0.708
	1	0.047	0.186	0.059
	2	0.091	0.237	0.233
X_2	0	0.708	0.474	0.581
	1	0.174	0.385	0.178
	2	0.118	0.141	0.241
X_3	0	1	0.667	0.285
	1	0	0.333	0.015
	2	0	0	0.700
X_4	0	0.753	0.458	0.568
	1	0.107	0.311	0.111
	2	0.140	0.231	0.321
X_5	0	0.799	0.486	0.603
	1	0.091	0.312	0.100
	2	0.110	0.202	0.297

Importance degree is a quantitative index of reflecting the influence of each component on the top event in the

reaction system. According to different conditions, the importance degree has many definitions. Structural importance degree, probability importance degree and key importance degree are applied widely in practical production. In addition, importance degree can make the quantitative analysis of the safety and reliability of the system, which is important in systematic reliability.

Among them, probability importance degree reflects the role of basic event to the top event. And it can compare the importance of various events in the system [23]. When the state of multi-state system is ε, probability importance degree formula of the component j is:

$$I_{\varepsilon}^{\Pr}(X_j)=\frac{\sum_{\tau=1}^{M_j} I_{\varepsilon}^{\Pr}(X_j^{\tau})}{M_j} \tag{10}$$

Where M_j represents the non-zero state total number of the component j, $I_{\varepsilon}^{\Pr}(X_j)$ represents the evaluation of probability importance degree under the system state of ε when the component j is in different state.

The value of probability importance degree can be calculated by the above formula (10).

$I_1^{\Pr}(X_1)=0.303$, $I_1^{\Pr}(X_2)=0.192$,
$I_1^{\Pr}(X_3)=0.480$, $I_1^{\Pr}(X_4)=0.238$,
$I_1^{\Pr}(X_5)=0.259$

5. The Comparison with the Fuzzy Fault Analysis Based on T-S

T-S probability importance degree is calculated on the basis of T-S importance degree calculation method proposed by the literature [12] when the state of the top event is 1. It is shown in the Table 7.

Table 7. T-S probability importance degree of fuzzy probability when the fault states of the essential event are 1 and 2

Probability importance	Fault state	
	1	2
$I_1^{\Pr}(X_1)$	0.362422	0.241162
$I_1^{\Pr}(X_2)$	0.248564	0.134755
$I_1^{\Pr}(X_3)$	0.957160	0
$I_1^{\Pr}(X_4)$	0.302467	0.171630
$I_1^{\Pr}(X_5)$	0.336677	0.179992

The formula $I_{T_q}^{\Pr}(X_j)=\frac{\sum_{i_j=1}^{k_j'} I_{T_q}^{\Pr}(X_j^{(i_j)})}{k_j'}$ is used, where k_j' means the number when the part j is in the fault degree of 1 and 2. k_j' is two because the fault degree is described by fuzzy 0,1,2.

The probability importance that is the basic event X_1 to top event T is gotten by generally considering T-S probability importance of the basic event X_1 in the fault condition 1 and 2.

$$I_1^{\Pr}(X_1)=[I_1^{\Pr}(X_1^1)+I_1^{\Pr}(X_1^2)]/2=0.302$$

Similarly, T-S probability importance of each basic event is available.

$I_1^{\Pr}(X_1)=0.302$, $I_1^{\Pr}(X_2)=0.192$,
$I_1^{\Pr}(X_3)=0.479$, $I_1^{\Pr}(X_4)=0.237$,
$I_1^{\Pr}(X_5)=0.258$

The comparison of results calculated by two different methods is shown in Table 8.

Table 8. Comparison between the probability importance degree calculated by this method and T-S probability importance degree calculated by the fuzzy fault analysis method

The results	Classification	
	probability importance degree calculated by this method	T-S probability importance degree calculated by the fuzzy fault analysis method
$I_1^{\Pr}(X_1)$	0.303	0.302
$I_1^{\Pr}(X_2)$	0.192	0.192
$I_1^{\Pr}(X_3)$	0.480	0.479
$I_1^{\Pr}(X_4)$	0.238	0.237
$I_1^{\Pr}(X_5)$	0.259	0.258

The following conclusion can be gotten.

(1) The calculation results obtained through T-S fuzzy fault tree analysis are similar to that with the method proposed by the author, which verifies the correctness of the result that is calculated by the above method. The important order of each basic event is $R_3 > R_1 > R_5 > R_4 > R_2$.

(2) When we use T-S fault tree analysis to calculate we can only calculate the probability in accordance with the structure of T-S fuzzy fault tree one by one from the bottom event to the higher event until the top event. This approach will generate a lot of calculations and can not be bidirectional inference, while the Bayesian network is not only simple operation and analysis but also can be bidirectional inference. Therefore, the Bayesian network is more suitable for engineering application.

6. Conclusion

The triangular fuzzy number instead of language variable is used to describe the component fault

probability, which solves the problem that the exact value of fault probability is difficult to obtain. Defuzzification of the fuzzy probability is conducted by using "mean area method", so the fuzzy information contained in operation is removed. The quantitative analysis and calculations of the system is realized, and the analytical results obtained are more clearly.

Currently Bayesian network in the elevator system reliability analysis is relatively limited. The application of Bayesian networks is expanded by combining fuzzy theory with Bayesian network. The importance degree of many factors affecting the elevator horizontal vibration is obtained by the importance analysis, and then the elevator is maintained and checked according to the importance degree. This can not only improve the reliability of the normal operation of the elevator, but also improve the maintenance efficiency.

Failure logical relational among components is determined. How to consider the ambiguity of failure probability and the uncertainty of failure logical relational among components will be the further research focus when failure logical relational is uncertainty.

References

[1] C.M. Zhu, "The comfortable elevation method of the elevator vibration". Construction Mechanization, No. 6, 1988, 29-32.

[2] S. Yokota, J.N. Liu, B. Huang, "Elevator vibration analysis". Hoisting and Conveying Machinery,No.8, 1987, 57-62.

[3] K. Okada and N. Nishimura, "Noise and vibration reduction techniques for 750 m/min elevators". Mitsubishi Electric Advance, Vol. 3, 1994, 2-4.

[4] C.M. Zhu, Elevator and escalators. 1st ed. Shanghai: Shanghai Jiaotong University Press; 1995.

[5] Q. Zong, G.Y. Li, M. Guo, "Design of diagnostic expert system for elevator system based on fault tree analysis". Control Engineering of China, Vol. 20, No. 2, 2013, 305-308.

[6] Q. Zhu, The long-distance monitor and the expert-based fault diagnosis for elevator systems. Tianjin: Tianjin University, 2003.

[7] Q. Zong, Z.H. Wang, X.Y. Luo, "Application of neural network technology in fault diagnosis of elevator system". Computer Applications, Vol. 23, No. 8, 2003, 78-80.

[8] D. Li, S. Su, Y.L. Ai, "Design of real-time fault diagnosis design system for elevator based on multi-information fusion technology". Computer Measurement & Control, Vol. 17, No. 11, 2009, 2162-2163.

[9] G. Levitin, "Block diagram method for analysis multi-state systems with uncovered failures". Reliability Engineering and System Safety, Vol. 92, No. 6, 2007, 727-734.

[10] W.S. Lee, D.L. Grosh, F.A. Tillman, C. H. Lie, "Fault tree analysis, methods and applications-a review". IEEE Transactions on Reliability, Vol. 34, No. 3, 1985, 194 - 203.

[11] A Rauzy, "New algorithms for fault tree analysis". Reliability Engineering and System Safety, Vol. 40, No. 3, 1993, 203-211.

[12] C.Y. Yao, Y.Y. Zhang, X.F. Wang, D.M. Chen, "Importance analysis method of fuzzy fault tree based on T-S model". China Mechanical Engineering, Vol. 22, No. 11, 2011, 1261-1268.

[13] ALYSON G W, APARNA V H, "Bayesian networks for multilevel system reliability". Reliability Engineering and System Safety, Vol. 92, No. 10, 2007, 1413-1420.

[14] X.W. Yin, W.X. Qian, L.Y. Xie, "Multi-state system reliability modeling and assessment based on Bayesian networks". Journal of Mechanical Engineering, Vol. 45, No. 2, 2009, 206-212.

[15] Langseth H, Portinale L, "Bayesian Networks in Reliability". Reliability Engineering and System Safety, Vol. 92, No. 1, 2007, 92-108.

[16] C.H. Yang, C.A. Zhu, X.J. Hu, "Methods on complex system fault diagnosis based on Bayesian network". China Mechanical Engineering, Vol. 20, No. 22, 2009, 2726-2732.

[17] C.L. Hu, "Research overview on Bayesian network". Journal of Hefei University, Vol. 23, No. 1, 2013, 33-40.

[18] H.T. Li, G. Jin, J.L. Zhou et al," Survey of Bayesian network inference algorithms". Systems Engineering and Electronics, Vol. 30, No. 5, 2008, 935-939.

[19] Q.G. Yang, "Application of Bayesian networks in the reliability analysis of electronic products". Electronic Product Reliability and Environmental Testing, Vol. 28, No. 5, 2010, 13-17.

[20] H.P. Zhu, G.J. Zhang, X.Y. Shao, "Study on the application of fuzzy TOPSIS to multiple criteria group decision making problem". Industrial Engineering and Management, Vol. 12, No. 1, 2007, 99-102.

[21] Wickens CD. Engineering psychology and human performance. 2nd ed. New York: Harper Collins Publishers Inc; 1992.

[22] R. Lan, J.L. Fan, "Complete metric on triangular fuzzy numbers and its application to decision-making". Journal of Systems Engineering, Vol. 25, No. 3, 2010, 313-319.

[23] S Contini, V Matuzas, "New methods to determine the importance measures of initiating and enabling events in fault tree analysis". Reliability Engineering and System Safety, Vol.96, 2011, 775-784.

المملكة الأردنية الهاشمية

الجامعة الهاشمية

المجلة الأردنية
للهندسة الميكانيكية والصناعية

JJMIE

مجلة علمية عالمية محكمة

تصدر بدعم من صندوق البحث العلمي

http://jjmie.hu.edu.jo/

ISSN 1995-6665

المجلة الأردنية للهندسة الميكانيكية والصناعية

مجلة علمية عالمية محكمة

المجلة الأردنية للهندسة الميكانيكية والصناعية: مجلة علمية عالمية محكمة تصدر عن عمادة البحث العلمي و الدراسات العليا في الجامعة الهاشمية بالتعاون مع صندوق دعم البحث العلمي في الأردن.

ترسل البحوث إلى العنوان التالي

رئيس تحرير المجلة الأردنية للهندسة الميكانيكية والصناعية

عمادة البحث العلمي والدراسات العليا

الجامعة الهاشمية

الزرقاء - الأردن

هاتف : 3903333 5 00962 فرعي 4147

Email: jjmie@hu.edu.jo

Website: www.jjmie.hu.edu.jo